USE OF BUS-LEVEL ELECTRICAL SIGNALS FOR IMPROVING POWER PLANT OPERATIONS

by

Prayag Kiritkumar Parikh

A dissertation submitted to the faculty of
The University of North Carolina at Charlotte
in partial fulfillment of the requirements
for the degree of Doctor of Philosophy in
Electrical Engineering

Charlotte

2020

Approved by:

_____
Dr. Robert W. Cox

_____
Dr. Tiefu Zhao

_____
Dr. Babak Parkhideh

_____
Dr. Monica Johar

ABSTRACT

PRAYAG K. PARIKH. Use of bus-level electrical signals for improving power plant operations. (Under the Direction of DR.ROBERT W. COX)

Power plant owners and operators are leveraging advancements in sensor technology and data science to deploy monitoring systems that can potentially improve reliability, increase flexibility, and reduce maintenance costs. In many cases, however, plants either do not have the budget for such technologies, or the return on investment is deemed to be too low. This thesis takes an alternative view and considers a potentially low-cost approach that can be implemented simply by monitoring the aggregate current flowing into a bank of downstream motors.

The approach described in this thesis relies on current and voltage sensors installed at either the main bus or a motor control center in a power plant. This non-intrusive technique can be used to provide some level of information about motors and their driven equipment. Previous work has demonstrated the ability to use such measurements to track the operation of various loads; this thesis looks to move beyond the tracking application to develop specific use cases in power plants.

This thesis considers two specific applications of bus-level current for sensing applications in power plants. First, this dissertation shows two use cases on the use of bus-level data for induction motor health monitoring. Second, the thesis shows how bus-level measurements can be used to estimate induction-motor electrical and mechanical parameters. These parameter estimates can be provided to planners and system operators to support various regulatory requirements, including startup after the loss of off-site power at nuclear units and startup of black start units after a blackout.

DEDICATION

for Dhani and Urvi

ACKNOWLEDGMENTS

I want to express my gratitude towards my advisor Dr. Robert Cox for sharing his wisdom and supporting me throughout my time at UNC, Charlotte. He has been my mentor since I started working with him on my Master of Science in Electrical Engineering. I am thankful to him for my academic success.

I sincerely thank Dr. Tiefu Zhao, Dr. Babak Parkhideh, and Dr. Monica Johar, for their guidance and support as part of my dissertation committee member.

I want to thank my fellow students Rebbeca Sawyer, Manav Patel, and Tyler Beach, for their support. I have learned a lot during my time at UNC, Charlotte, from many of the professors and fellow students. I want to thank them all for sharing valuable knowledge with me. I will try and do the same in my life.

I am grateful to Susan Maley, Steve Seachman, Mike Ruszkowski, Dr. John Shingledecker, Neva Espinoza, and Tom Alley of EPRI for their encouraging words, guidance, and generosity.

I am forever indebted to my wife Urvi for her unwavering support through this seemingly never-ending journey. Her belief in me reinforced my will to complete this journey. Finally, I would like to thank my daughter Dhani for her understanding and unconditional love.

EPRI partially funded the research presented in this thesis.

TABLE OF CONTENTS

LIST OF TABLES

LIST OF FIGURES

CHAPTER 1: INTRODUCTION AND BACKGROUND

This thesis describes an induction machine and connected mechanical load monitoring techniques using bus-level measurements with two case studies. One of the case studies is associated with a coal crusher motor and another with centrifugal pump-motor. This thesis also proposes a novel technique to estimate an induction machine parameter using bus-level electrical measurements. These techniques can be beneficial in a power plant environment. The following section of this chapter provides an overview of the requirement for monitoring an induction machine and a connected mechanical load in a power plant. The latter part of the section also provides an overview of one of the power plant applications for induction machine parameter estimation.

1.1 Monitoring and Diagnostics of Induction Motors in a Powerplant

As more renewable energy penetrates the energy market, the cycling of the base loaded coal, and nuclear power plant will likely increase. This cycling potentially increases thermal and electric stresses on the assets of these power plants. Besides, resources of nuclear and coal power plants, for example, Operations and Maintenance (O&M) budgets, as well as maintenance personnel, are reducing [1, 2]. However, it is expected to maintain the high reliability of these power plants [1]. Therefore, power plant owners and operators have either begin or planning to install continuous on-line monitoring sensors to reduce manual preventive maintenance (PM) tasks while maintaining the reliability of these power plant assets despite challenges.

In recent years, the Electric Power Research Institute (EPRI) has published continuous on-line monitoring (COLM) guidebook Volume 1-8 [3]. These volumes discuss various aspects of the monitoring, diagnostics, and prognostics in a power plant environment. Volume 7 of this guidebook

has equipment specific guidance related to the sensors, and monitoring and diagnostics associated with these sensors. This volume provides information regarding various sensors that can be installed on that particular asset for monitoring and diagnostics. In addition, it also includes information on various preventive tasks that can be eliminated or extended due to the installation of these new sensors while maintaining the overall reliability of that asset. Examples of such equipment specific guides are [4-10].

This section of the document discusses various diagnostics techniques that are either being used or can be used in the power industry for different induction machines. Specifically, it discusses monitoring technologies for medium voltage induction motor and its applications. Application of such motors includes coal and gas power plant critical assets, for example, feedwater pumps, forced draft fan, induced draft fan, coal crusher, coal pulverizer, circulating water pump, cooling pumps, and so on. Unforeseen maintenance or failure of such machines can cost powerplant owners in terms of lost or reduced output, and maintenance cost. In some cases, failure of such machines can endanger safety, for example, in the nuclear power plant where this type of induction motors are used for cooling purposes.

1.1.1 Overview of Failure Modes Associated with Induction Motors

One of the EPRI's database is called Preventive Maintenance-base Database (PMBD) [11], lists all the possible failure modes of power plant assets and various PM tasks that can potentially discover these failure modes. One of the purposes of this database was to help the power plant industry with its preventive maintenance schedule, depending on individual requirements to achieve reliability. The PMBD is an extensive database of failure modes and various discovery methods to detect these failures of equipment for a variety of power plant assets.

Figure 1.1 shows the breakdown of all the possible failure modes of less than 15kV horizontal induction motor. In this figure, failure modes were divided into four major components – stator, rotor, bearing, and shaft of the induction motor. The rest of the failure modes were divided into other electrical or mechanical failure modes. Altogether, there are 70 faults listed in the PMBD

database for the type of induction motor. As seen in the figure, nearly two-thirds of the failures are associated with the rotor, bearing, and stator.

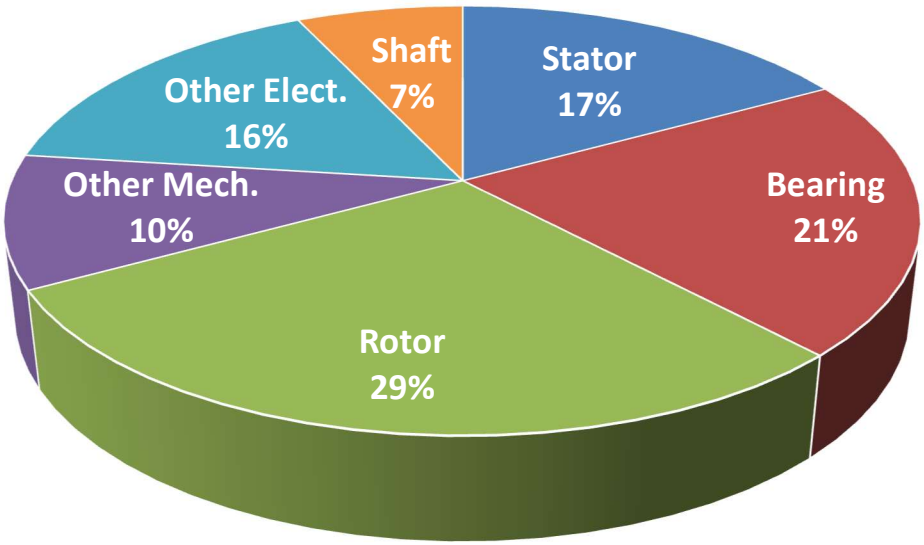

Figure 1.1: Breakdown of faults associated with major components in less than 15kV induction motor [12].

Table 1.1 shows the results of the IEEE survey and EPRI report that shows the percentage of failure by major components of induction motor. As seen in this table, slightly more than two-thirds of the fault also occurs due to the same three components. Figure 1.1 and Table 1.1 also confirms that bearing failure occurs the most often compared to other failures of the induction machine components.

The failure related to the bearing includes loose hardware, wear of the seals and rolling element, and so on. Rotor failure modes are associated with loose, broken or degraded laminations, retaining ring, shorting ring, and insulation. Stator related failure modes are associated with winding insulation degradation, loose bracing, wedge, blocking and tying, and stator laminations. As listed in [4], predominant monitoring technology for the monitoring of this type of motors includes Electrical Signature analysis (3-phase voltage and current sensors), Vibration monitoring, and winding temperature monitoring.

Table 1.1: Causes of failures by major components of the induction machine, from [13].

Cause	IEEE Survey	EPRI Report
Bearing Related	44	41
Stator Related	26	36
Rotor Related	8	9
Other	22	14

1.1.2 Review of Continuous On-line Monitoring (COLM) Technologies

There are many continuous on-line monitoring technologies in the market for induction machine monitoring and diagnostic. Some of the prominently used on-line monitoring technologies include Vibration Analysis, Motor Current Signature Analysis (MCSA), and temperature monitoring. In addition, some utilities also employ winding temperatures and partial discharge analysis (PDA) for electrical fault monitoring of the induction motor windings. The following sections discuss the MCSA or ESA and Vibration analysis technologies.

D1: Electrical Signature Analysis (ESA)

Electrical Signature Analysis (ESA) is similar to motor current signature analysis (MCSA) for induction motors. However, ESA can apply to other electrical machines, thus not specifically for the motors. Classic MCSA utilizes only stator input currents to detect various faults, as described in [14, 15]. Some of the commercially available MCSA systems also use voltage signals to derive additional key performance indicators (KPI). These KPIs can help further analyze the health of the induction machine, such as voltage unbalance, power factor, and torque measurements. Similar to those commercially available MCSA systems, ESA also uses the voltage signal to help with some of the signal manipulations; for example, Park's transformation vector analysis [16]. Figure 1.2 shows the typical ESA sensor installation. As seen in this figure, current transducers (CTs) and potential transducers (PTs) can be installed at the motor control center (MCC). In the case of low voltage motors, these CTs and PTs can be installed directly at the motor terminal. In the case of medium voltage motor, general practice is to install these sensors at the

secondary of the measuring current transformer and potential transformer, respectively [17], as shown in Figure 1.2.

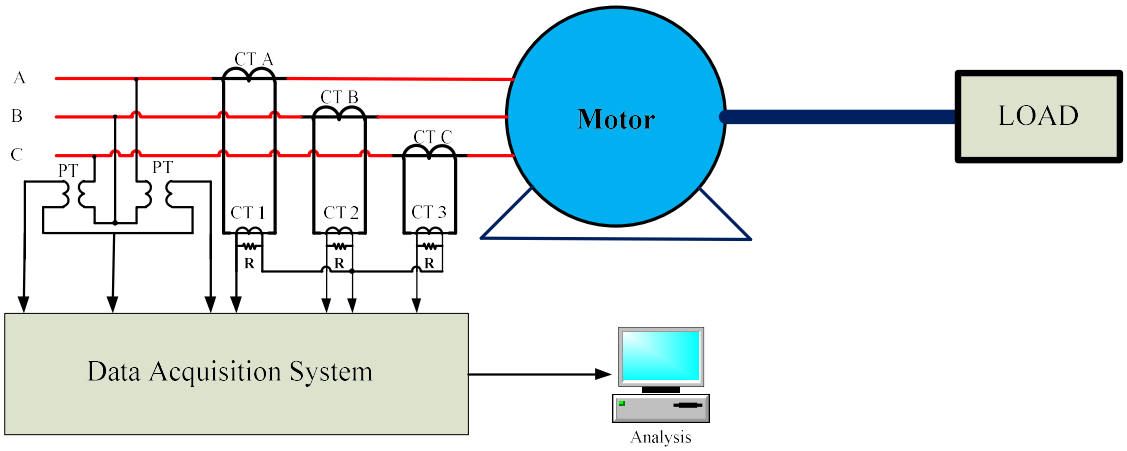

Figure 1.2: Typical Electrical Signature Analysis (ESA) sensor installation for an induction motor [14].

The current drawn by an induction machine is dependent on the physics of the system; this system includes electrical motor and mechanical load driven by this motor [14]. Any change in the physics of the system can change the current drawn by the stator of the machine. MCSA or ESA uses this change in stator current to detect anomalies in the induction machine.

Classic motor current signature analysis is similar to the vibration signature analysis where spectral analysis, RMS, and peak-to-peak value of the raw signal is calculated. In addition, within the spectral analysis, specific frequencies or frequency band magnitude or energy is estimated to detect faults.

A brief review of various signal processing techniques that can be used with voltage and current signals of the induction motor is provided in [18] and [19]. A literature review of [15, 16, 18-23] suggests that various signal processing techniques can detect bearing, stator, and rotor related anomalies in a motor using current and voltage signals. However, most of the commercially available online MCSA packages don't include these types of signal processing techniques that potentially provide better anomaly detection of stator and rotor faults [24]. Generally, in the power

industry, commercially available systems are used to collect rout-based data instead of continuous on-line data.

Based on academic literature as well as commercially available systems review, it appears that MCSA is better suited for anomalies related to bearing, the eccentricity of the airgap detection, load unbalances, and some ability to detect rotor bar defects [18-21].

D2: Vibration Analysis

Vibration analysis technology is relatively more mature than the MCSA or ESA technologies for monitoring of induction motor and mechanical loads connected to the motor. There are three different types of vibration measurements used in the industry, namely displacement, velocity, and acceleration. Generally, displacement measurement is used for the faults that manifest at lower than 10Hz frequency, velocity measurement is used for the defects that manifest at around 10Hz to 2kHz frequency and acceleration is used for fault frequencies in the range of 5kHz. An accelerometer is a commonly used vibration sensor for induction motors. Depending on the application of vibration analysis, vibration sensors are installed at multiple locations on the induction machine and connected mechanical loads. These locations include in-board bearing, and out-board bearing, of the pump, fan, and motor [4].

There are two types of accelerometers available in the market, single-axis and triaxial. A single-axis accelerometer can measure vibrations in one of the three-axis, namely: horizontal, vertical, and radial. Triaxial accelerometers can measure vibrations in all three directions simultaneously.

Measurement of the phase angle, magnitude, and the Fast Fourier transform (FFT) of the raw signal are commonly used signal processing techniques for vibration analysis. Vibration analysis widely used for monitoring mechanical faults, for example, bearing failures, eccentricity faults, and load unbalances type of faults. In some cases, this technology also provides some information on rotor bar faults of the induction motor.

In addition to technologies mentioned here, measurement of bearing temperature, lubrication oil analysis, flow, and pressure measurements are also used to monitor faults in the induction machine. Partial discharge analysis to monitor the health of induction machine insulation is also applied to high voltage motors in many cases.

1.1.3 Expected Thesis Contribution

As mentioned earlier, there are many monitoring technologies for induction machine monitoring. Most of these technologies are off-line and route-based for time-based maintenance. Continuous on-line monitoring for conditioned-based maintenance of the induction motor is enabled by on-line measurements, for example, vibration monitoring and MCSA or ESA measurements.

The focus of the thesis is the use of bus-level electrical measurements to detect anomalies in the induction machine and connected mechanical loads. The use of bus-level electrical measurement for induction machine monitoring provides an opportunity for power plant owners to reduce the number of sensors to be installed for improving condition-based monitoring of power plant assets. This type of monitoring is particularly attractive for nuclear power plants. In nuclear power plants for each sensor, the plant has to conduct and document the detailed evaluation of new sensor and installation details according to Nuclear Regulatory Commission (NRC) [25, 26] to ensure the safety and reliability of a nuclear power plant. This type of detailed evaluation for each sensor can be lengthy and costly. Reduced number of sensors for monitoring can reduce this cost, which is a high cost compared to the actual price of the sensor. Besides, a reduced number of sensors minimizes the cost of the procurement and installation of the sensors for fossil power plants.

Reduced number of sensors enables the cost-effective installation of monitoring sensors for fossil and nuclear power plants. In turn, the installation of these sensors enables cost-effective condition-based maintenance of power plant assets with limited maintenance personnel.

1.2 Overview of Black Start

Black start can be defined as "the capability of generating units to start without an outside electrical supply or the demonstrated ability of a generating unit to automatically remain operating at reduced levels when disconnected from the grid" [27], [28]. Regional Transmission Organization (RTO), for example, Pennsylvania, Jersey, and Maryland (PJM), and Electric Reliability Council of Texas (ERCOT) has select black start capability units that can help restore power on the grid in the event of cascade tripping of generators within that region. The selection of such units is based on the fulfillment of North American Reliability Corporation (NERC) requirements, as mentioned in [29] [30] as well as RTO requirements, as mentioned in [31]. The modeling, simulation, and other requirements are similar to the requirements outlined in the CIGRE document [32]. In this thesis, the black start from the generator operator's point of view is considered. There are two main types of blackouts at the power plant:

i. The individual island or powerplant experiences shut down due to loss of grid connection. In this case, the grid connection is lost because of unforeseen faults of the system.
ii. The cascade tripping of several generators on the grid occurs due to an unbalance of power demand and supply caused by system faults.

In either case, the power plant needs to restart its normal operation to energize transmission lines that supply power to the end-users. In both scenarios, power needs to be provided to the power plant auxiliary loads first before the main gas or hydro turbine generator starts. Examples of such auxiliary loads in gas power plants include; cooling system, fuel system, lighting loads, communication equipment, safety systems, protection relays, and generator excitation. The auxiliary loads in the hydropower plant include; generator excitation system, lighting loads, communication equipment, protection systems, safety systems, and oil system will need energizing before the main generator startup.

In the case where a power plant loses grid connection, the power plant can be restarted by reconnecting to the grid and using grid power to start the auxiliary loads. The exception to that is a nuclear power plant. When a nuclear power plant loses a grid connection, it is called loss of off-site power (LOOP). It will cause the tripping of a nuclear power plant. In that case, the nuclear power plant requires a black start type of capability to maintain safety systems, unit's substation systems, and motor control center (MCC) that has critical equipment.

When there is a cascade tripping of many generators on the grid, the grid power is not an option. In this case, it is a responsibility of RTO selected black start units, for example, gas turbines or hydro turbines to step by step energizing the grid. These black start unit's auxiliary loads need power before the startup of the main gas or hydro turbine. Diesel generator or other types of the power supply provides power to these auxiliary loads.

1.2.1 Black Start Sequence Overview

Section 2.2 of reference [28] provides an overall step by step information on black start sequence from the power plant operator perspective. The generalized black start sequence summary is as follow [28]:

1. Plant Operating normally – all main generator working and providing power, diesel generator off-line.
2. Plant completely blacked out – all main generators off-line, all station service loads, and system loads off-line.
3. Start the diesel generator.
4. Diesel Generator starts supplying power to the plant emergency services, for example, lighting loads, instrumentation, and communication devices.
5. In the next step, diesel generator provides power to auxiliary equipment of the gas or hydro turbine and the main generator, for example, pumps and motors, compressed air system, pressurized oil system, generator excitation system, and other necessary loads to start the main generator.

6. Bring the black start unit's main generator to the rated voltage.
7. The transmission line can be connected based on RTO's request.
8. The diesel generator can be powered down at this point.
9. Auxiliary loads of other units at the black start site can be started in a manner that system frequency and voltage is maintained to prevent tripping of other generators.
10. As other generator starts, it can pick up loads at the transmission operator's request.
11. Energize a crank path that includes the closing of appropriate circuit breakers to energize the transmission line, which provides power to other generating sites auxiliary loads.
12. Auxiliary loads at different locations can be started while keeping the balance of power demand and supply.
13. Bring other generators on the grid on-line.
14. Continue following the grid restoration process.

In this process, for diesel generators or black start unit's main generator and other generators, loads are added at a pace that maintains the stability of the system. This prevents the tripping of energized generators. Tripping of re-energized generators may warrant restarting the black start process.

Many publicly available documents discuss the time duration to restart the black start unit and close the dead bus to provide off-site power to nuclear units, according to the requirement of the RTO [28, 33]. However, these public documents don't offer information on the pace at which different auxiliary equipment should be restarted to maintain system stability. It is understandable, as each unit is different, and the auxiliary load requirements might be different. The utility with a black start unit documents the procedure to start up the auxiliary loads, its order, and the pace at which each load starts. This procedure documentation is one of the black start unit capability requirements. It was challenging to find this type of procedure document from publicly available information. Upon discussions with power plant personnel, it was informed that the sequence of starting of each load and wait time between two loads is documented for a black start unit's

auxiliary loads. The wait time is based on the perceived time required for the electrical load to go from transient to steady-state. This wait time between the two auxiliary loads is generally based on past experiences and the original equipment manufacturer's suggestions.

1.2.2 Expected Thesis Contribution

Many of the auxiliary loads to start the black start unit's main generator require the starting-up of various induction motors that can enable cooling system pumps, feedwater pumps, and other similar loads. During the start-up, the induction motor draws approximately 5-7 times of steady-state current, which can be attributed to the electromechanical system energization. This high current can potentially contribute to destabilizing the startup of the black start unit as well as the system as a whole when starting auxiliary loads of the other generators. If the induction motor is starting a pump connected with the higher volume piping system, the motor can take longer to attain the steady-state. The case study in Chapter 4 will discuss this phenomenon in brief. As mentioned in [28], one of the assumptions in the industry is induction motor generally takes 2 – 4 seconds. According to power plant personnel in the documented process, the startup of the induction machine can take up to 5 – 60 seconds, depending on the application of the induction motor. If the induction motor starting up a pump is a first motor to start in the system, then the discharge valve is closed for the first few seconds. Closing of the discharge valve helps reduce sustaining transient current amplitude. This sustaining current helps push the flow of liquid in the piping system. The assumption regarding transient time duration and amplitude can be extreme assumptions. Method to determine startup time duration, as well as transient amplitude for each motor, can help optimize the starting of auxiliary loads of the black start units. Knowledge of startup time duration and magnitude of the current during startup can help stable and efficient startup of black start unit.

This thesis attempts to develop a method to dynamically determine the parameters of the induction machine using bus-level current and voltage measurements. The knowledge of induction machine parameters can help assess startup time, the active and reactive power requirement of individual machines at the startup. Methods to optimize the starting auxiliary load sequence can

help power plant owners in restarting black start units efficiently on time without destabilizing the system.

1.3 Organization of the Document

Chapter 2 of this thesis provides an overview of the non-intrusive load monitoring system (NILMs) used to acquire electrical measurements at the bus-level. Section 3 discusses one of the use cases related to the monitoring of induction motor using bus-level current measurements. This chapter discusses the detection of loss of coal crusher hammer mass. Chapter 4 is another use case for monitoring of induction machine and the connected mechanical load. In this chapter, simulation and laboratory tests are discussed to detect the accumulation of deposits in a pump fluid pump. Chapter 5 presents a brief overview of past research related to the parameter estimation techniques for induction machines. This chapter provides broad information on widely used techniques to estimate the induction machine parameter in power plants. Chapter 6 proposes a novel method to estimate induction motor parameters using in-phase and quadrature-phase stator current components calculated by NILM. Chapter 7 provides a summary and suggests future work in this area of research.

CHAPTER 2: NON-INTRUSIVE LOAD MONITORING (NILM) OVERVIEW

In this dissertation, non-intrusive load monitoring (NILM) is used to acquire bus-level voltage and current measurements. As seen in Figure 2.1, NILM can be installed at a central location; for example, the motor control center (MCC). The NILM uses current and voltage transducers to measure voltage and aggregate currents flowing through the bank of electrical loads downstream. These sensors can be installed directly at the motor terminal for the low voltage motors. In the case or medium voltage motors, these sensors are generally installed at the secondary of the instrumentation potential and current transformers. A brief overview of NILM theory related to this dissertation, as well as past research using NILM is discussed in the following sections of this chapter.

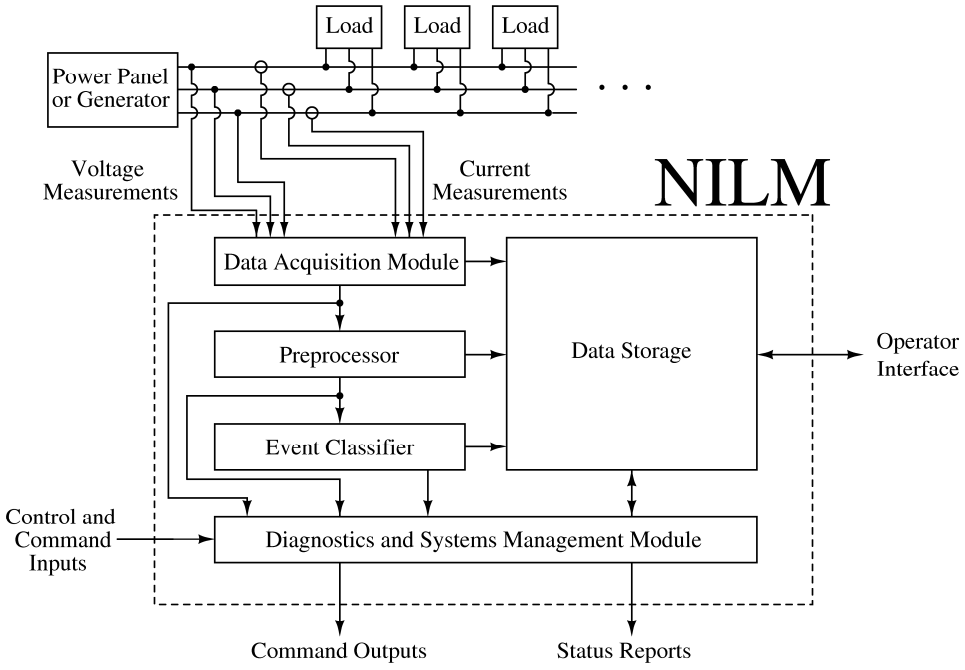

Figure 2.1: NILM Block Diagram.

2.1 NILM Overview

2.1.1 Calculations of Spectral Envelope

NILM's software-based pre-processor performs a spectral decomposition of the aggregate current $i(t)$ drawn by the downstream electrical loads connected to the same bus bar [34] and [35]. As mentioned in [36], the concept is that a real waveform $x(t)$ can be described with arbitrary accuracy as time-varying spectral coefficients $a_k(t)$ and $b_k(t)$ at time $t \in (t - T, T]$ using Fourier series:

$$x(t - T + s) = \sum_k a_k(t) \cos\left(k \frac{2\pi}{T}(t-T+s)\right) + \sum_k b_k(t) \sin\left(k \frac{2\pi}{T}(t-T+s)\right) \quad 2\text{-}1$$

The variable k in equation 2-1 ranges over the set of positive integers, T is a period and $s \in (0, T]$ [34], [35], [36] and [37]. The formula for calculating Fourier Series coefficients $a_k(t)$ and $b_k(t)$ is as follow [34], [35], [36], [37] and [38]:

$$a_k(t) = \frac{2}{T} \int_0^T x(t - T + s) \sin\left(k \frac{2\pi}{T}(t - T + s)\right) ds \quad 2\text{-}2$$

$$b_k(t) = \frac{2}{T} \int_0^T x(t - T + s) \cos\left(k \frac{2\pi}{T}(t - T + s)\right) ds \quad 2\text{-}3$$

NILM uses both voltage and current signals to estimate spectral coefficients $a_k(t)$ and $b_k(t)$ of the aggregate current $i(t)$. The coefficients $a_k(t)$ and $b_k(t)$ are calculated by synchronizing $\cos\left(\frac{2\pi}{T}t\right)$ of the above equations with the bus voltage and then averaging the products of the observed current and synchronized sine waves over one or more periods of the measured voltage [34, 36] and [39]. These coefficients are harmonically related in-phase component $a_k(t)$ and quadrature-phase component $b_k(t)$. These estimated spectral envelopes can be interpreted as real, reactive, and harmonic power [34] and [40]. To explore this idea, consider an example; assume the measured line voltage is constant amplitude, and a constant frequency sine wave of the form:

$$v(t) = V \sin(\omega t) \quad 2\text{-}4$$

When there is a load current, the measured line current will be a combination of the form:

$$i(t) = I\,sin(\omega t + \phi) \tag{2-5}$$

The real and reactive power provided by the voltage source will be:

$$P = \frac{V}{T}\int_0^T i(t)\,sin(\omega\tau)\;d\tau = \frac{VI}{2}cos\,\phi \tag{2-6}$$

$$Q = \frac{V}{T}\int_0^T i(t)\,cos(\omega\tau)\;d\tau = \frac{VI}{2}sin\,\phi \tag{2-7}$$

For the current and voltage waveforms considered in this example, the NILM would compute the following two spectral envelope coefficients:

$$a_1(t) = \frac{2}{T}\int_{t-T}^{t} i(t)\,sin(\omega\tau)\;d\tau = I\,cos\,\phi \tag{2-8}$$

and

$$b_1(t) = \frac{2}{T}\int_{t-T}^{t} i(t)\,cos(\omega\tau)\;d\tau = I\,sin\,\phi \tag{2-9}$$

These two values can be combined to determine the amplitude of the line current, as shown below:

$$\sqrt{a_1^2 + b_1^2} = I\sqrt{sin^2\phi + cos^2\phi} = I \tag{2-10}$$

If the voltage remains reasonably constant, both a_1 and b_1 can be scaled to provide the measurement of the real and reactive power. Bus voltages are relatively constant in the power plant environment. The spectral envelope coefficients change over time as the amplitude and phase of the current change. Figure 2.2 demonstrates the relationship between the measured current and the spectral envelope $a_1(t)$ and $b_1(t)$ during the start of an incandescent bulb, as described in [35]. The top trace of that figure shows current drawn by an incandescent bulb, middle and bottom trace shows calculated spectral envelope coefficients $a_1(t)$, which is an in-phase component and $b_1(t)$, which is the quadrature-phase component. Power P or in-phase spectral envelope coefficient $a_1(t)$

changes rapidly as filament heats-up, and once it reaches the steady-state, it only consumes in-phase power as expected.

NILM can calculate harmonic spectral envelope coefficients of aggregate current *i*(t). The information generated due to these spectral envelopes can be used for fault detection as well as dynamic parameter estimation of an induction motor. Both of these use cases are described in greater detail in further chapters of this thesis.

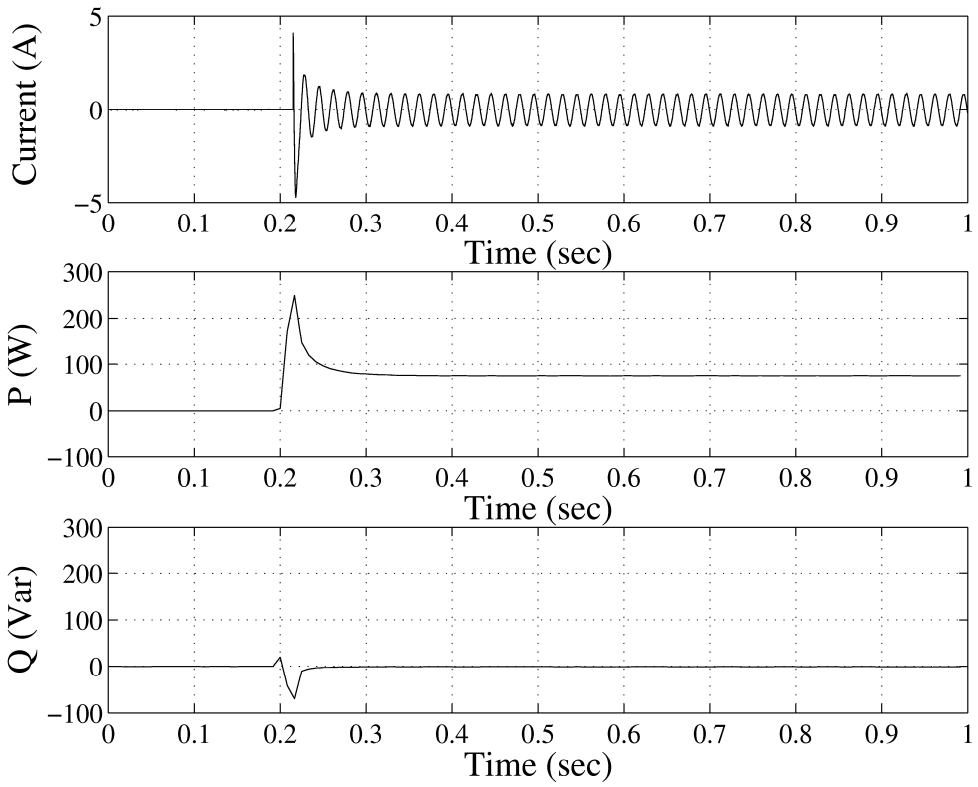

Figure 2.2: Calculation of in-phase current component $a_1(t)$ and quadrature-phase current component $b_1(t)$. The top picture shows the current drawn by the bulb. The middle image shows the calculated active power P with the in-phase current component. The bottom trace shows the calculated reactive power Q using the quadrature-phase component.

2.1.2 Identification of Load using Aggregate Current

NILM uses transient and steady-state methods to detect loads using the aggregate current measurements. NILM requires initial in-field training to identify loads using an aggregate signal. Both transient and steady-state methods of identifying load are briefly described below.

D1: Load Identification using Steady-state

NILM can measure a change in in-phase power and quadrature-phase current components up to 7th harmonic. In the training phase, the known load turning on and off, as well as the associated change in in-phase power and quadrature-phase power, can help NILM identify the load. The method to disaggregate loads in this manner is described in [41] and [42]. As described in [41] and [42], in some cases, two different loads can have a similar change in active and reactive power levels. The ability of NILM to calculate spectral coefficients of higher-order harmonics as well can help differentiate identical loads. Figure 2.3 shows the change in active and reactive power levels for the 150w computer as well as the 150w incandescent bulb. As seen from the top trace, it is hard to distinguish between the two loads. However, as seen in the bottom two traces, the higher-order harmonics measurements help in detecting a specific electrical load.

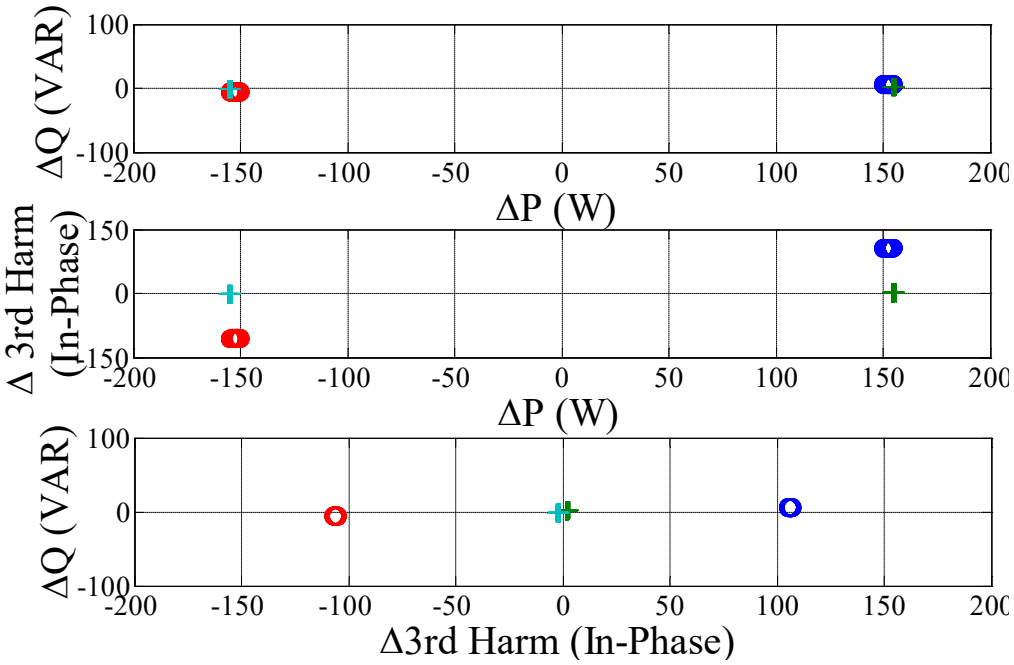

Figure 2.3: Identification of load using steady-state current measurements. The picture shows the turning on and off of 150w bulb with a "+" sign and 150w computer with an "o" sign. The top picture shows the change in the quadrature-phase power component Vs. in-phase component of power when the load is turned on and off. The middle image shows the change in 3rd harmonic in-phase power Vs. fundamental in-phase power. The bottom image shows the change in fundamental quadrature-phase power Vs. 3rd harmonic in-phase power.

D2: Load Identification using Transient

The physical task influences the transient behavior of the electrical load. Figure 2.4 shows the transient current drawn by a laptop and an induction motor. As seen on the right side of the image, the induction motor draws large in-rush current during startup. As the rotor attains near synchronous speed, current reduces to a steady-state level. The left image shows the turning on of a laptop. As seen in this figure laptop draws higher modulated current. The current is high at the startup, but it subsides to steady-state modulated current. The laptop current is modulated because of the power supply circuit of the laptop. As seen in this figure, the transient behavior of each load is unique. Also, the entire transient behavior or part of the transient behavior is repeatable [18] and [43]. This unique quality of electrical load can serve as a "fingerprint." Thus event detection using the transient identification technique is a very reliable tool. Further chapters of this thesis also describe some of the use cases of fault detection using the transient signature.

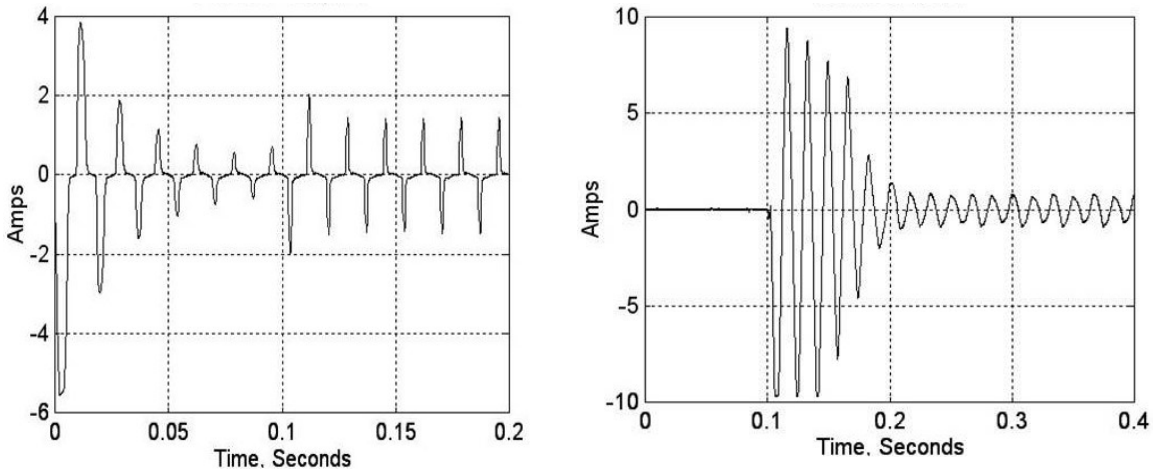

Figure 2.4: The current drawn by a laptop in the left, and current drawn by an induction motor on the right.

NILM stores transient behavior of the downstream loads connected to the same bus-bar in a library. These stored transients are known as exemplars. Each section of the exemplar is stored in vector t_i. In operation, NILM uses the scaled and shifted version of this vector to match incoming current data to identify the load. Mainly, this process involves least-square fit, as shown in equation

2-11. In this equation, the exemplar vector t_i is related to the input data X by gain coefficient α and an offset value of β. In equation 2-11, "1" is a vector of ones.

$$X = [t_i \quad 1] \begin{bmatrix} \alpha \\ \beta \end{bmatrix} \qquad 2\text{-}11$$

An example of a matching induction motor startup is shown in Figure 2.5. The top trace of the figure shows the raw current signal due to the induction machine startup. The continuous trace in the bottom shows the envelope calculated using NILM, whereas trace with "x" indicates the matching process using exemplar.

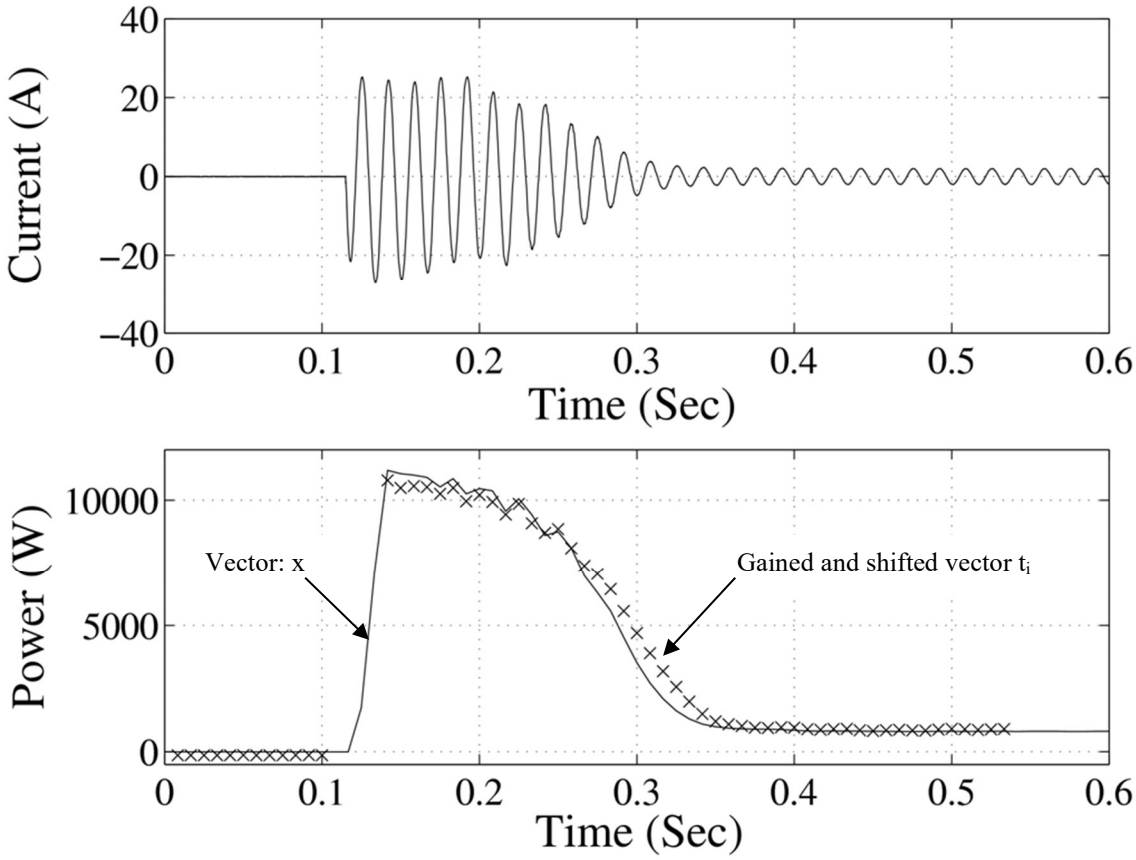

Figure 2.5: Successful identification of induction motor using the transient identification technique. Top trace: Transient current drawn by an induction motor. Bottom trace: Computed power and section of the template that has been successfully matched to the observed transient behavior by NILM.

NILM uses a combination of transient and steady-state methods to identify loads. Further information on load identification using NILM is described in [44]. In steady-state, NILM continues to monitor the power level of the load as described in [44] and [45].

NILM has been used in many research to detect faults in the induction machine systems, examples of such research include, coupling Failure [46], Detection of the leak in the cycling system [47], clogged filters in water treatment plant [48], clogged filters in household HVAC systems [49], short cycling of the compressor and detection of inadequate refrigerant charge [50].

CHAPTER 3: CASE STUDY 1 – COAL CRUSHER MOTOR

Coal crusher is a critical electrical load driven by the induction machine in a coal power plant. The function of the coal crusher is to crush the raw coal in granulated pieces and remove some debris from the raw coal. The granulated coal from the coal crusher then fed into the pulverizer of the power plant. Pulverizer grinds the granulated coal in pulverize form that can be used as fuel for a coal-fired power plant. If the hammers of the coal crusher are deteriorated, the quality of coal coming out of the coal crusher degrades. The degraded quality of crushed coal can affect the function of the pulverizer and, eventually, the performance and thermal efficiency of the power plant.

Widely used coal crusher in power plants, the "Pennsylvania Granulator," has coal hammers located at the periphery of the shaft [51]. Coal comes from the top, and as it comes in contact with hammers, the coal gets crushed. Due to the very function of the coal crusher, overtime hammers are deteriorated.

This case study describes the simulation model development for a coal crusher system using the 5^{th} order induction machine model and results derived from this simulation. In addition, it also describes the installation of the NILM system at a coal power plant and results associated with the installation. NILM was installed at the MCC, which supplied power to two of the coal crushers with identical induction machines. Degradation of coal crusher hammers was trended over time using bus-level voltage and current measurements.

3.1 Coal Crusher System Modeling and Simulation Results

In this case study, the "Pennsylvania Granulator" was driven by a 600 HP, 4160V, and 10-pole induction machine. The simulation model used to simulate this type of electromechanical

system is based on information provided in [52]. The brief description of the simulation modeling and results are discussed in this section.

3.1.1 Induction Machine Simulation Model

The induction machine is a multiply excited electromechanical energy convertor. In which, the electrical and the mechanical systems are connected via magnetic coupling. Figure 3.1 shows the cross-section area of a 3-phase, 2-pole induction machine with symmetrical winding and squirrel cage rotor. The stator winding of the induction machine is 120 electrical degrees apart in space [52]. The stator windings are represented with a_s, b_s and c_s. This figure also shows the magnetic axis of the a-phase winding. Distributed stator winding has N^s equivalent number of turns per phase with the stator winding resistance r^s. Similarly, the rotor has an equivalent number of turns N^r and winding resistance r^r. The stator winding of a 3-phase induction machine can be excited by a balanced 3-phase voltage source; voltage on the rotor is induced due to the induction effect [52] and [53].

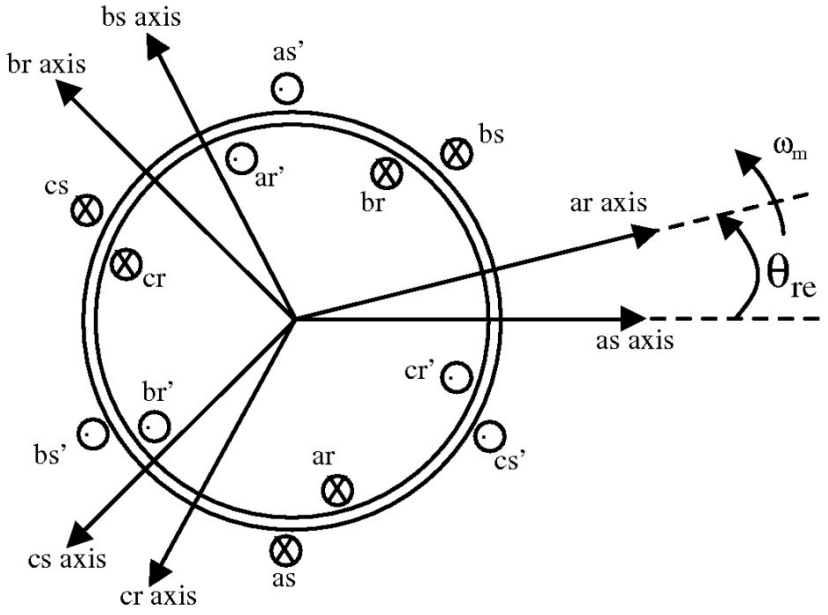

Figure 3.1: Cross-section of a three-phase symmetrical machine with two poles.

The fifth-order model using Park's transformation is used in this case study. Equations 3-1 to 3-4 are associated with the electrical system of the motor [52]. In these equations, superscript

"s" refers to the stator quantity, and superscript "r" refers to the rotor quantity. In these equations, rotor and stator quantities are transformed on to synchronously rotating "dq0" frame. Subscript "d" and "q" refer to the d-axis and q-axis, respectively. Voltage is referred to as "v," resistance as "r," current as "I," flux linkages with "λ" and "ω" is angular velocity.

$$V_q^s = \omega\lambda_d^s + \frac{d}{dt}\lambda_q^s + r^s i_q^s \quad 3\text{-}1$$

$$v_d^s = -\omega\lambda_q^s + \frac{d}{dt}\lambda_d^s + r^s i_d^s \quad 3\text{-}2$$

$$v_q'^r = (\omega-\omega_{re})\,\lambda_d'^r + \frac{d}{dt}\lambda_q^r + r'^r i_q^r \quad 3\text{-}3$$

$$v_d'^r = -(\omega-\omega_{re})\lambda_q'^r + \frac{d}{dt}\lambda_d^r + r'^r i_d'^r \quad 3\text{-}4$$

The mechanical system modeling of the induction machine can be explained with Newton's second law of motion for linear motion machine, which states that "The acceleration of an object as produced by a net force is directly proportional to the net force and inversely proportional to the mass of the object." In the case of the rotating induction machine, the force is replaced with the torque. The mechanical model of the induction motor can be explained using equation 3-5. Equation 3-6 is associated with electromechanical coupling between the electrical model and mechanical model of the induction machine [52]:

$$T_a = \frac{d\omega}{dt} = \frac{1}{J}(T_e - T_l) \quad 3\text{-}5$$

Where,

$$T_e = \left(\frac{3}{2}\right)\left(\frac{P}{2}\right)\left(\lambda_d^s\, i_q^s - \lambda_q^s\, i_d^s\right) \quad 3\text{-}6$$

Where,

ω: The rotational frequency of the rotor.

T_e: Torque produced by the motor

T_l: External torque provided by a mechanical load on the motor

T_a: Acceleration torque

J: Mass moment of inertia

Here, for a cylindrical object, the mass moment of inertia J can be defined as:

$$J = \frac{1}{2} Mr^2 \qquad 3\text{-}7$$

Where M is mass of the rotor, and r is the radius of the rotor.

3.1.2 Simulation and Results

As mentioned earlier, coal crusher hammer deteriorates due to the very function of the hammers, which is to crush the raw coal in a granulated form. As the hammers deteriorate, it loses mass, which reduces the mass moment of inertia, as seen in equation 3-7. As the moment of inertia decreases, the rate of change of speed $\frac{d\omega}{dt}$ increases as seen in equation 3-5. Consequently, the motor accelerates faster to attain steady-state speed. This phenomenon affects the duration of the inrush current. Monitoring the in-rush current duration can help track the loss of coal crusher hammer mass. The tracking of the inrush current duration can help power plant personnel to schedule condition-based maintenance according to the perceived deteriorated condition of hammers.

During the coal crusher startup, the only load torque is the mass of the machine and the windage surrounding it. Thus, the load torque can be modeled using the following equation:

$$T_l = A\omega^2 \qquad 3\text{-}8$$

MatLab® simulation model included equations 3-1 to 3-4 for the electrical system model and equation 3-5, 3-6, as well as equation 3-8 for the mechanical system model. The specifications used for the induction motor are shown in Table 3.1. As seen in this table, the simulations were performed for two different values of inertia to investigate the potential change in transient time duration for the same machine parameters.

Figure 3.2 shows simulated transient currents using two different values of inertia (*J*) for the same machine. As seen in this figure, in-rush current time duration with the higher value of the

mass moment of inertia J is higher. This change in the in-rush current time duration was as expected. The mass moment of inertia changes the rate of change of speed $\frac{d\omega}{dt}$ as seen in equation 3-5.

In Figure 3.2, the phase currents extracted from the simulation were quantized and passed through the NILM's preprocessor algorithm. The resulting spectral coefficients a_1 and b_1 were used to compute the time-varying component of the stator current. This value can be calculated using the following relation:

$$I = \frac{1}{\sqrt{2}} \sqrt{a_1^2 + b_1^2} \qquad 3\text{-}9$$

Table 3.1: List of parameters for 3-phase squirrel cage induction motor used for simulation [52].

Quantity	**Rating**
Horsepower	500 hp.
Voltage rating	2300 v.
RPM	1773 rpm
Number of poles	4
Torque	1980 N-m
Stator resistance	0.262 ohms
Stator leakage reactance	1.206 ohms
Magnetizing reactance	54.02 ohms
Rotor leakage reactance referred to stator	1.206 ohms
Rotor resistance referred to stator	0.187 ohms
Moment of inertia	11.06 / 8.06 kg-m^2

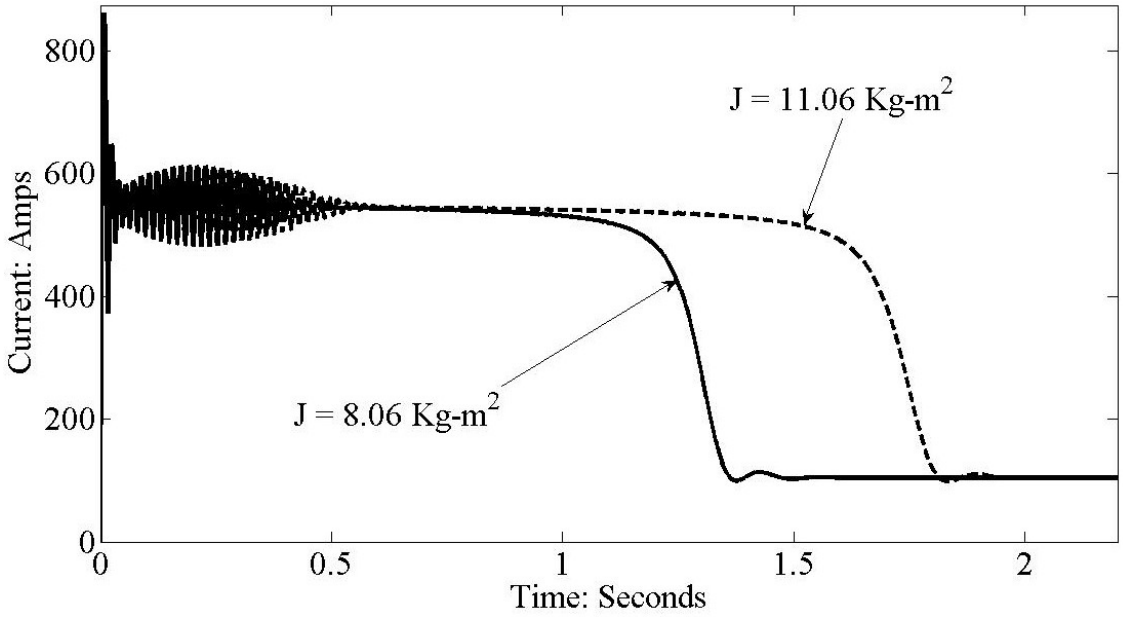

Figure 3.2: Amplitude of the simulated in-rush current for two different mass moment of inertia values.

3.2 Field Installation

As shown in Figure 3.3, the NILM was installed on the 4160V main busbar of the coal crusher unit that provided power to multiple electrical loads at a coal power plant. The focus of this project was to monitor coal crusher hammers for any anomalies. The 4160 main bus also provided power to two coal crusher induction motors. In addition to the bus-level measurement, NILM was also equipped to monitor the individual coal crushers. Figure 3.4 shows the one-line diagram of sensor installation for NILM.

Figure 3.3: Picture of the NILM installation. The NILM computer and box are at the top of the crusher panel.

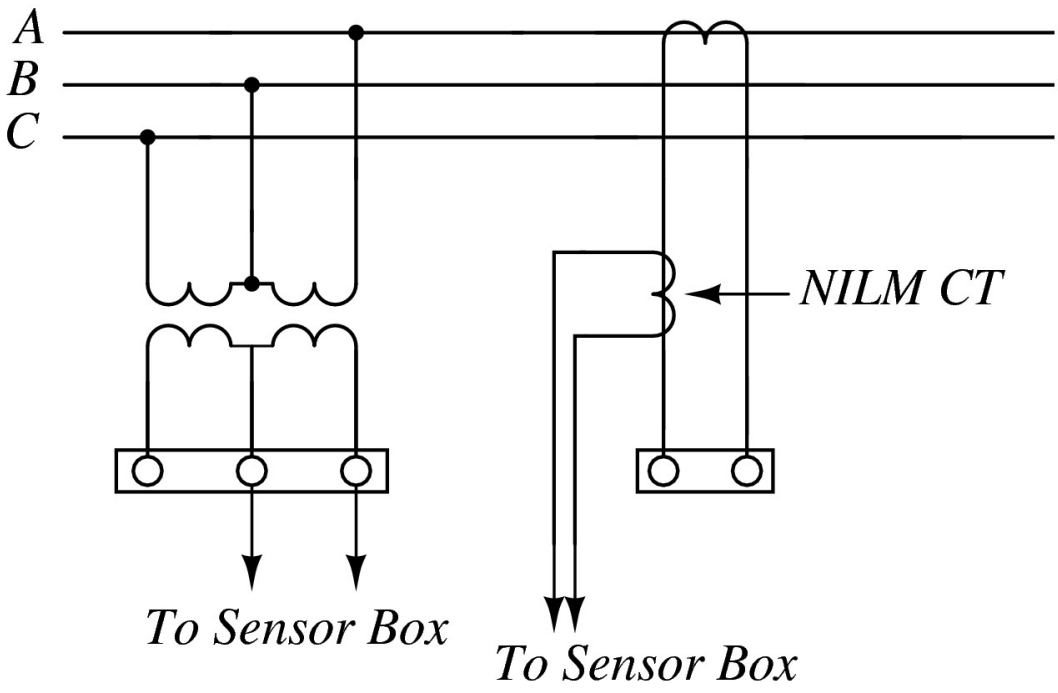

Figure 3.4: Sensor connection for the bus-level monitoring equipment. Similar connections were made for the coal crusher sensors.

3.2.1 Brief Description of the Coal Crusher Unit

At the power plant, the coal crusher unit was connected to the 4160V service, and it provided power to several electrical loads essential for coal crushing process. Direct on-line starters used to start the motor were connected to the 4160V. Table 3.2 lists loads connected to the 4160V bus. As seen in this list, a 2000 kVA transformer feeding MCC-1 and MCC-2 is also connected to the 4160V bus. As seen in Table 3.3 and Table 3.4, these MCCs are supplying 480V electrical loads essential for coal crushing process.

Table 3.2**:** List of loads connected to 4160V bus

Load Name	**Rating**
Crusher-5	600 HP
Crusher-6	600HP
Transformer feeding MCC 1 and MCC 2	2000 kVA
Belt Conveyor BC-13	125 HP
Belt Conveyor BC-17	125 HP

Table 3.3: List of loads connected to MCC-1

Description	Rating
Belt Feeder 2 VFD	200 HP
Air Compressor	150 A
Belt Feeder 3 VFD	200 HP
480/120-240 Lighting Transformer	100 kVA
Belt Conveyor BC-14	200 HP
Sampling System	150 A
Unloading Hopper Exhaust Fan	2 HP
Dump Hopper Area Welding Receptacle	100 A
Sump Pump at Tail of BC-17	20 HP
BC-15 Maintenance Area Sump Pump	20 HP
Drive Area of BF 2/3 Hoist Motor	5 HP
BC-13 Tramp Iron Magnet Rectifier	15 kW
Shaker Motor and Hoist Motor (North Control Unit)	60 A
Shaker Motor and Hoist Motor (South Control Unit)	60 A
Diverter Gate Motor	5 HP
4160V Gear Battery Charger	30 A
Belt Feeder BF-2/3 Welding Receptacle	100 A
Pasco Building Power (Maintenance Building)	200 A
480V/120-240 V Single Phase Lighting Transformer	37.5 kVA
Unloading Building Stairwell Exhaust Fan	10 HP
Dump Hopper Vault Sump Pump BC-13	20 HP
BC-16 Maintenance Area Sump Pump	20 HP
Unloading Building Hoist	5 HP
BC-13 Tramp Iron Magnet Belt Drive	10 HP
Electrical Room Heating and Vent	25 kVA

Table 3.4: List of loads connected to MCC-2

Description	Rating
Plow Feeder Drive	155 HP
Belt Conveyor BC-15	125 HP
BC-17 Tramp Iron Magnet Belt Drive	5 HP
BC-17 Tramp Iron Magnet Rectifier	10 kW
Proportioning Gate Motor	5 HP
Belt Conveyor BC-18	100 HP
Emergency Hopper Vent Fan	3 HP
BC-15 Tunnel Vent Fan	3 HP
Plow Shed Heater	10 kW
Transfer Station 'E' Supply Fan	10 HP
BC-16 Tunnel Vent Fan	3 HP
Plow Shed Heater 2	10 kW
Crusher Building Vent Fan 1	0.25 HP
Rotary Plow Maintenance Shed Hoist Motor	5 HP
Remote LP-V2 Dust Suppression Room Reclaim Area	37.5 kVA
Remote LP-V1 Dust Suppression Room Crusher Building #2 Area	37.5 kVA
Crusher Area Hoist Motor	10 HP
Crusher Door Opener Motor	2 HP
BC-15 Maintenance Area Welding Receptacle	100A
BC-16 Maintenance Area Welding Receptacle	100A
Crusher Building 2 Welding Receptacle	100A
Head of BC-15, BC-16 Welding Receptacle	100A
Belt Feeder #4 VFD	15 HP
Coal Yard Drainage Pumps	94 HP
Unloader Area Lighting Transformer	75 kVA
Sampling System	100 A

3.2.2 Brief Description of the Coal Crusher

The primary interest in this thesis is the two coal crushers installed in a Fossil Plant. Figure 3.5 shows the picture of one of the 600 HP coal crushers motor, the electrical load of interest for this thesis. Figure 3.6 shows the image of a coal crusher connected to the motor as well as other supporting systems. Raw coal is fed to the crusher from the top chute, as shown in Figure 3.6. Belt conveyors supplied coal to the chute. BC-15, BC-17, and BC-18 were the belt conveyers crucial for the coal crusher's operation. Belt conveyers BC-15 and BC-17 fed the raw coal to the coal crushers. Belt conveyer BC-18 takes crushed coal to the pulverizers. Coal crushers are responsible for crushing the raw coal into granulated form. Once the coal crusher breaks the raw coal into small

particles, belt conveyers take this crushed coal to the coal pulverizers. Coal pulverizer crushes this coal into a fine powder that can be used as fuel at the burners of the boiler.

Figure 3.5: Picture of 600 HP coal crusher's induction motor.

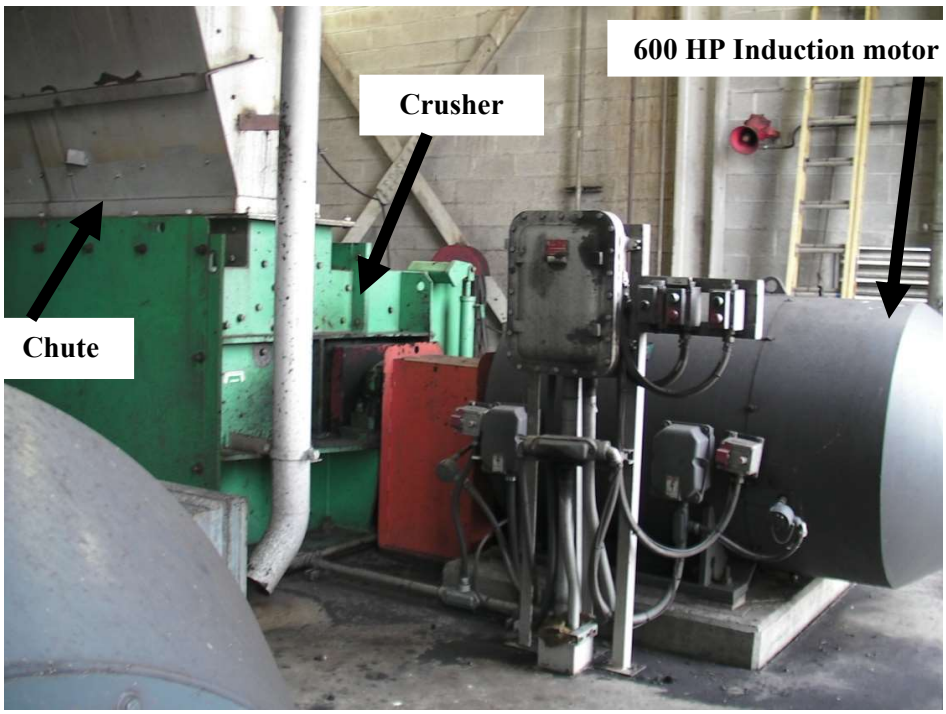

Figure 3.6: Picture of coal crusher connected to 600 HP motor.

3.3 Field Test and Results

NILM collected the data for about three months on this coal crusher unit. Coal crushers started one after another, almost at the same hour of every morning, and ran till the mid-afternoon. Maintenance was performed on both coal crushers when NILM was installed at the MCC. The maintenance was performed on one coal crusher at a time. Each maintenance period was for a few days for each coal crusher. During the time of maintenance, coal crushers were out of service. Plant personnel usually performed this time-based maintenance every six months. If the quality of the fine coal from the pulverizer degrades due to variation in crushed coal quality, the plant requested maintenance before scheduled maintenance. During the maintenance, among other maintenance activities, plant personnel replaced degraded hammers with new hammers and balanced the load around the shaft. An example of a degraded hammer and a relatively new hammer is shown in Figure 3.7. As seen in this picture, the degraded hammer has lost significant mass compared to the new hammer. NILM was able to collect data for before and after maintenance was performed on both coal crushers. The results of the field test are documented in this thesis using that data. The Example of data collected using the NILM of typical coal crusher startup with auxiliary loads is shown in Figure 3.8.

Figure 3.7: Coal crusher hammers: Picture on the left shows the degraded hammer removed from the coal crusher and picture on the right shows the replacement of the degraded hammer.

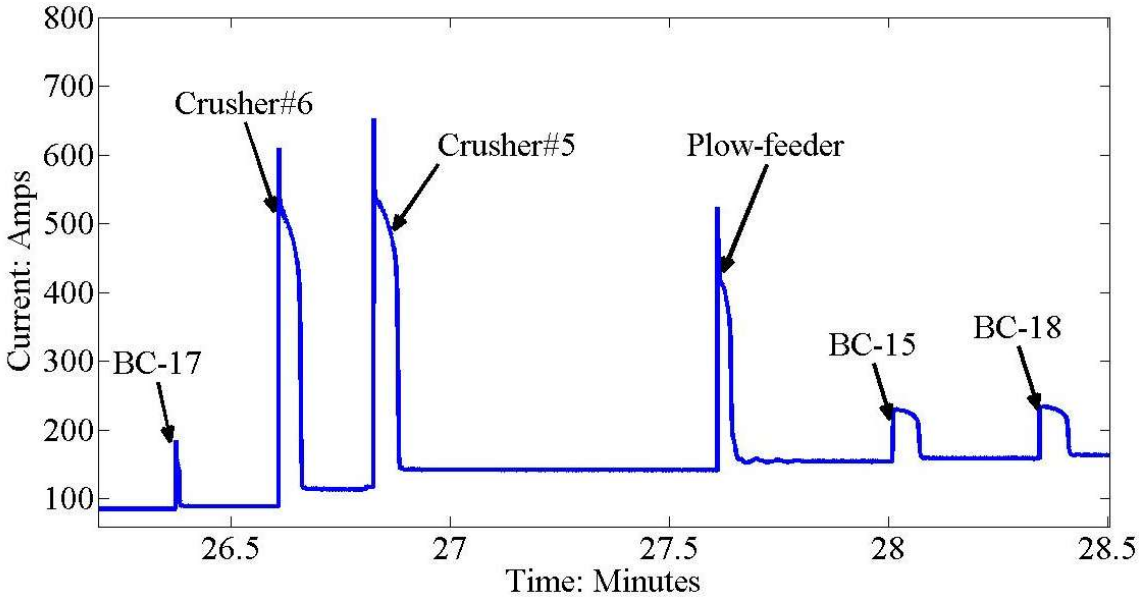

Figure 3.8: Bus-level current measurement for a typical crushers start-up sequence.

3.3.1 Transient-based Time Domain Analysis and Results

As mentioned earlier, the very function of the coal crusher causes hammers to degrade. As the hammers degrade, it loses mass. Consequently, the value of the moment of inertia reduces. Based on the simulations performed using two different values of the moment of inertia, it was observed that the motor takes less time to attain a steady-state for a lower value of the moment of inertia than a higher value of the moment of inertia as shown in Figure 3.2.

Both crusher motors were connected to the 4160V bus, where the NILM was installed. During the period of data gathering, both crushers underwent maintenance for a few days. Power plant personnel replaced the degraded hammers with new hammers and balanced the load across the shaft during the maintenance period. NILM acquired the data for before and after maintenance. Figure 3.9 shows the traces of current data obtained at 4160V bus for before and after maintenance. This figure is explicitly generated to show the comparison between transient time durations for crusher-6 induction motor before and after maintenance. As seen in this figure, the transient time duration after the maintenance was longer than the transient time duration before the maintenance. This result matches with simulation results shown in Figure 3.2.

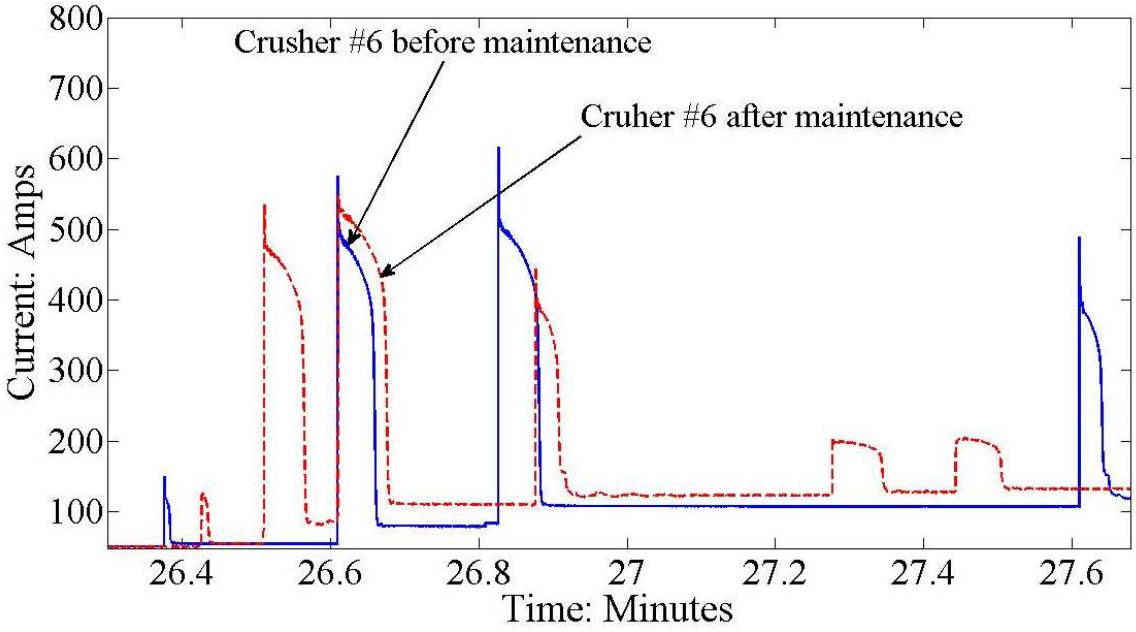

Figure 3.9: Current data recorded with NILM at the 4160V bus during the start sequence of crushers. The continuous trace showed the aggregate current recorded before maintenance, and a dashed trace shows the aggregate current after maintenance.

During the time NILM was installed at the plant, coal crusher hammers' degradation was tracked using a trend plot of transient time duration for each crusher motor. Such a process is shown in Figure 3.10. This process can help power plant personnel in scheduling maintenance of coal crusher based on condition. Condition-based maintenance can help the plant save in maintenance costs compared to time-based maintenance. It can also provide a better opportunity to produce better quality crushed coal for pulverizer continuously.

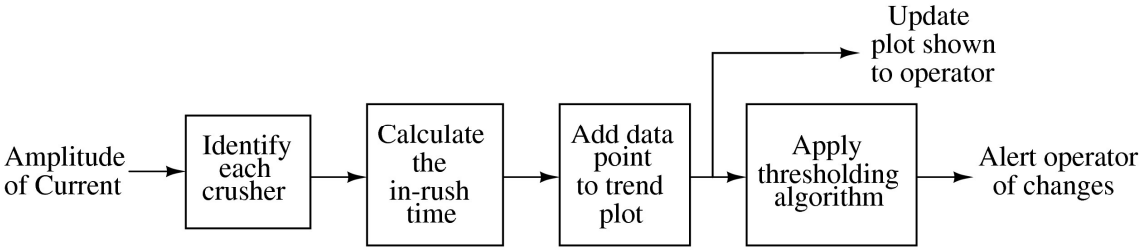

Figure 3.10: Potential transient-based detection algorithm for coal-hammer monitoring.

Figure 3.11 shows the transient time duration recorded for crusher-6, and Figure 3.12 shows the trend of transient time duration for crusher-5. As seen in both trend plots, after maintenance transient time duration for both induction motors is almost 1 second longer than the

transient time duration before maintenance. Moreover, close observation of the trend plot Figure 3.11 and Figure 3.12 also shows that the transient times are slowly reducing overtime.

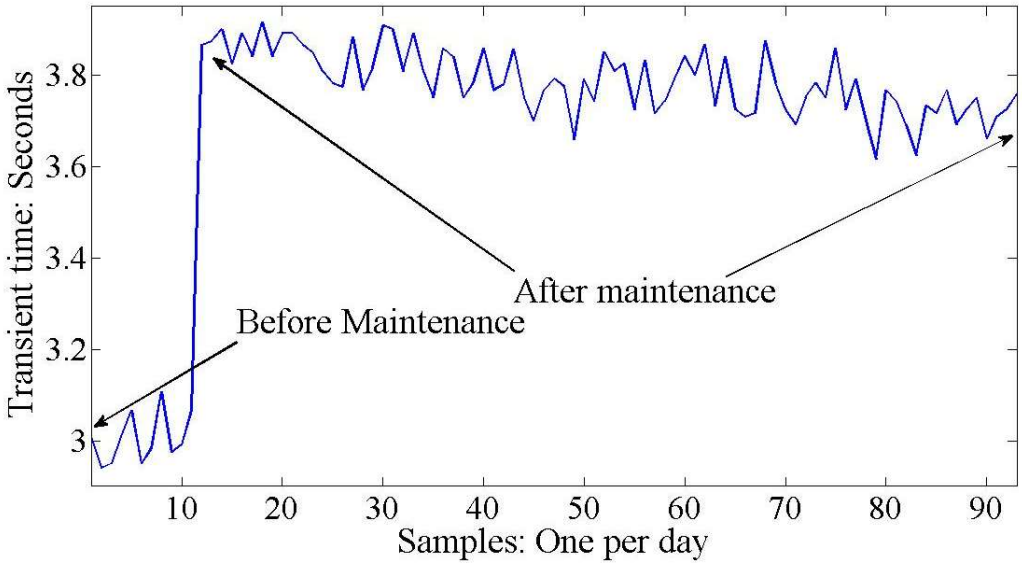

Figure 3.11: Trended transient time for crusher-6 throughout the field test.

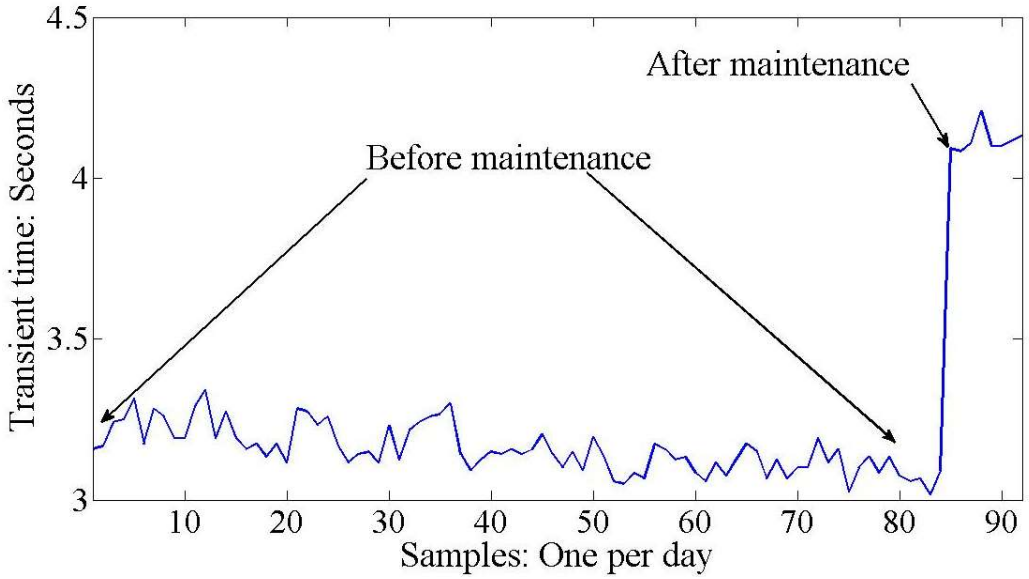

Figure 3.12: Trended transient time for crusher-5 throughout the field test.

3.3.2 Steady State Based Frequency Domain Analysis and Results

The sets of hammers are located at the periphery of the shaft, and it crushes the coal as the hammers come in contact with raw coal fed from the chute. This function of the coal crusher

hammer degrades the hammers. As shown in Figure 3.7, hammers lose weight as it deteriorates. Some portion of the hammer set might degrade differently than the other. This uneven degradation creates an unbalanced load on the shaft. In case of an unbalanced load, the motor will experience average torque T_0 and torque ripple at the shaft speed. This torque will be of the form as below [53] and [54]:

$$\tau = T_0 + T_1 \sin(\Omega_m t) \quad 3\text{-}10$$

Where Ω_m is the mechanical rotational speed of the motor. This torque pulsation causes the machine's air gap to vary its length as it rotates. Consequently, this torque pulsation causes the amplitude of the current to change at shaft speed. When measuring the magnitude of the current with a NILM, the current signal will be of the form:

$$i = I_0 + I_1 \sin(\Omega_m t + \varphi) \quad 3\text{-}11$$

These shaft-speed variations in the torque can be observed in the frequency spectrum analysis of stator current signals. In this case, the coal crusher's induction motor was a 10-pole machine, so the mechanical rotational speed is 12 revolution per second (RPS) or 12Hz. The motor is not always rotating at that speed. Therefore, the variations due to torque ripple will appear at around 12Hz in the stator current spectrum.

A diagnostic tool shown in Figure 3.13, can help track the amplitude of the shaft-speed variation using spectral analysis technique. As shown in this figure, the Fast Fourier Transform (FFT) of the stator current is calculated first. The output of the FFT contains real and imaginary components that provide phase and amplitude value of the stator current components. Once the FFT is computed, the shaft speed is searched, and amplitude corresponding to the shaft speed is recorded. The value of shaft speed can also be affected by the varying load. The shaft speed amplitude value is normalized using the average value of the current over FFT period to account for varying load conditions. Adding data points for each calculation can provide insight into the varying unbalance around the shaft.

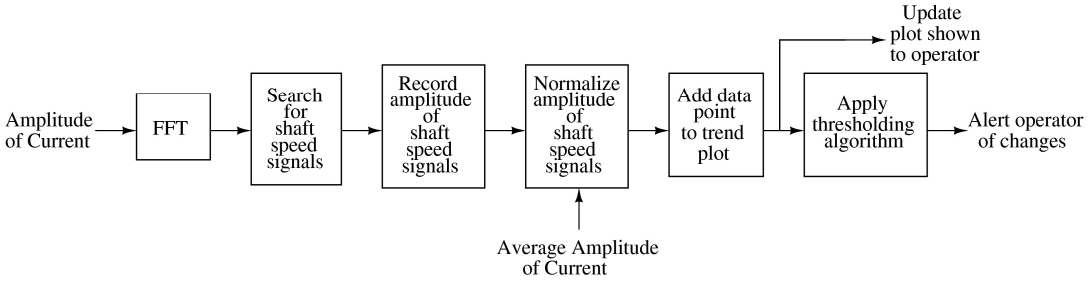

Figure 3.13: Process to track the trend of shaft speed amplitude variations in the measured current spectrum.

D1: Coal Crusher Hammer Degradation Detection Using Steady-State Current

Both coal crusher motors were identical 600 HP and 10-pole machine. Detecting shaft speed variations using bus-level measurements for two identical motors can be difficult. Despite being identical, most of the time, they do not run at the same speed. Appropriate parameters of FFT calculations; for example, FFT length and windowing function [38] can help differentiate both signals even when they are a fraction of 1Hz apart in the FFT plot, as shown in Figure 3.14. However, when the speed of the motors is too close, it may be difficult to distinguish between the two signals.

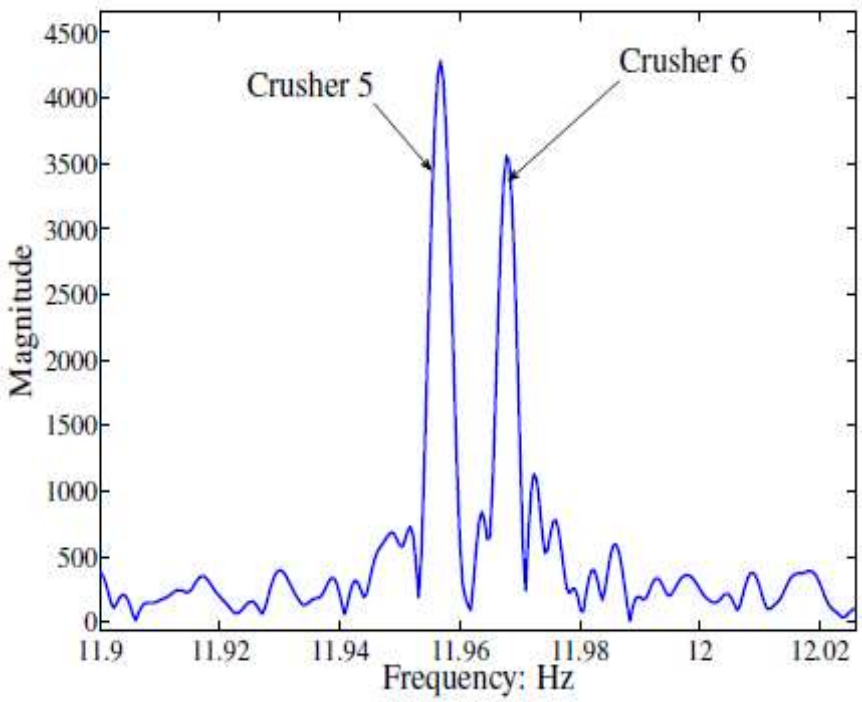

Figure 3.14: FFT of the time-varying amplitude of the aggregate current zoomed into the vicinity of 12Hz.

Using the procedure outlined in Figure 3.13, following each crusher start-up average magnitude of the current for each crusher was calculated, and the speed of the crusher is determined. The FFT was calculated three times a day for a minute-long current data. The magnitude of shaft speed frequency was extracted and normalized using average current data for each crusher. Figure 3.15 shows the trend plot of normalized shaft speed frequency magnitude for coal crusher-6 before and after maintenance. As seen in this figure, most of the time, this shaft speed frequency magnitude is higher before maintenance as the effect of unbalance predominantly high. However, there are certain times after maintenance when the magnitude is close to the magnitude before maintenance. Averaging these values over three consecutive measurements shows a clear distinction between before and after maintenance as shown in Figure 3.16.

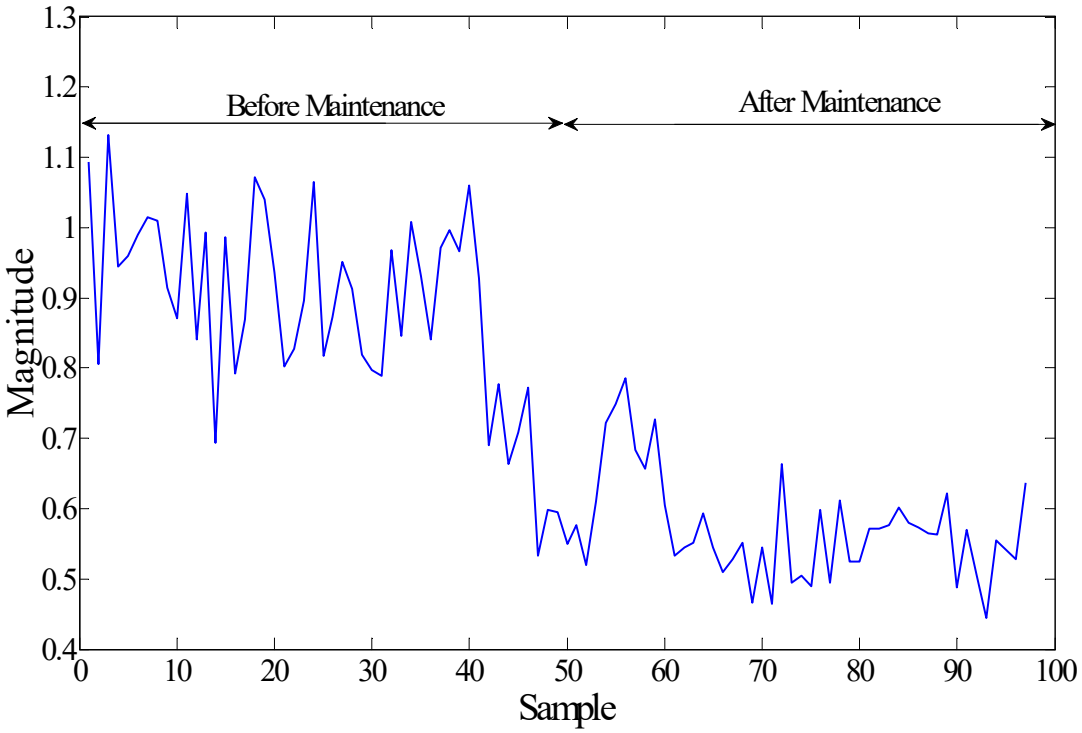

Figure 3.15: Normalized magnitude of the shaft-speed signal for Crusher-6.

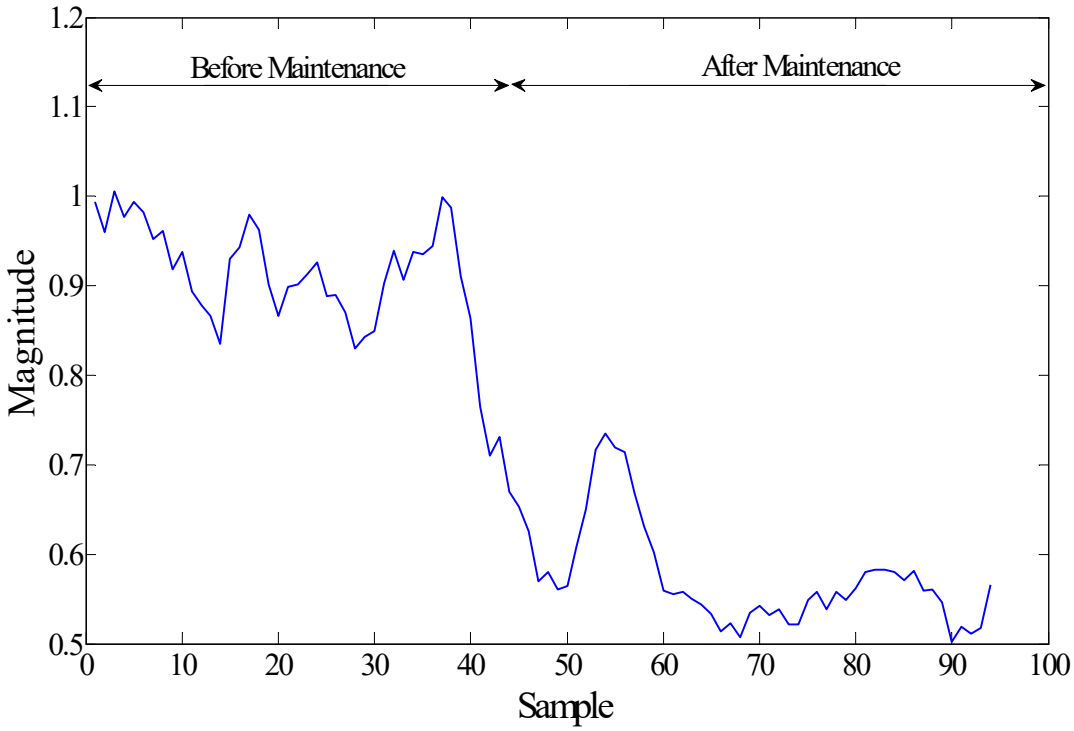

Figure 3.16: Normalized amplitude of the shaft-speed signal for Crusher-6. Data points in this plot were created by averaging over three adjacent data points from Figure 3.15.

D2: Vibration Monitoring Using Steady-State Current

The vibration of the machine also exhibits the torque ripples in the current spectrum at the shaft speed, similar to an unbalanced load condition. Coal crusher has significant vibration issues as well. Specifically, contaminations in raw coal can increase vibration and damage hammers. Thus, coal crushers were fitted with the vibration switches, which can trip in the event of highly abnormal vibrations. Figure 3.17 and Figure 3.18 shows such an event captured with bus-level current measurements as well as individual crusher current measurement. Once the vibration switch was tripped, plant personnel investigated the incident and found one of the hammers dislodged in the crusher, which contributed to increased vibrations. Figure 3.19 shows the trend plot for the normalized value of the shaft speed frequency. This plot followed the same procedure outlined in Figure 3.13. As shown in Figure 3.19, the normalized value for samples 15 through 19 slightly higher. These samples are from the current measurement a couple of hours before the vibration switch tripped. The sample 20 is where the switch tripped. As shown in this figure, after

maintenance, the vibration value returned to reasonably similar value to samples before the vibration switch tripped.

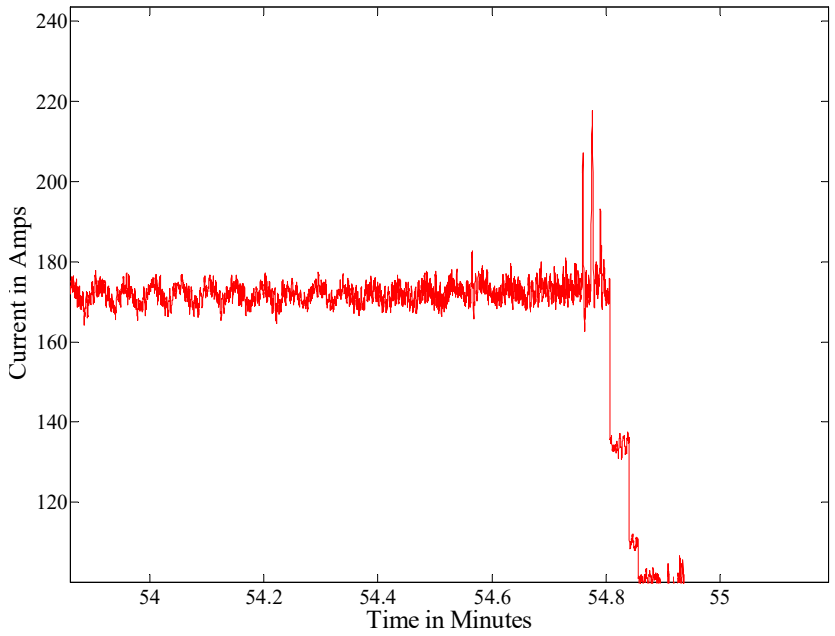

Figure 3.17: Amplitude of bus-level current before and after vibration switch tripped because of a dislodged hammer from crusher shaft.

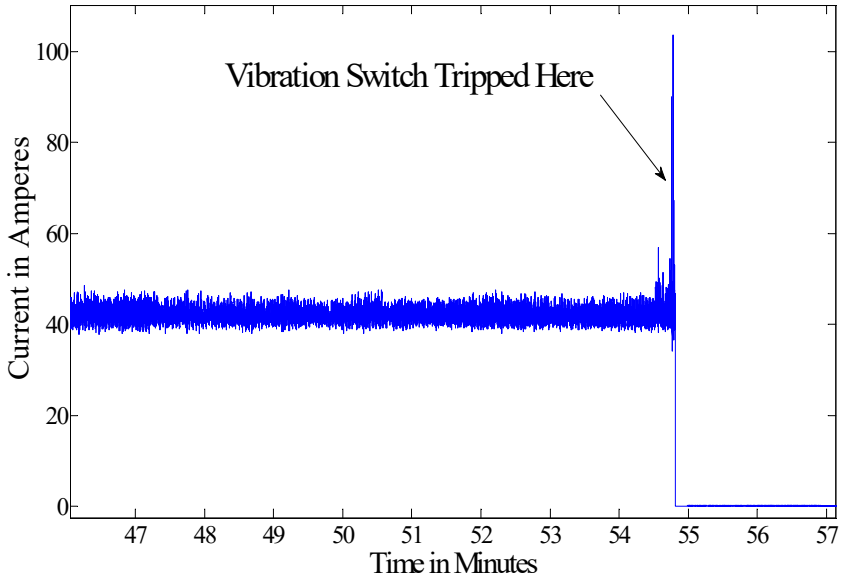

Figure 3.18: Amplitude of crusher-6 current before and after vibration switch tripped because of a dislodged hammer from crusher shaft.

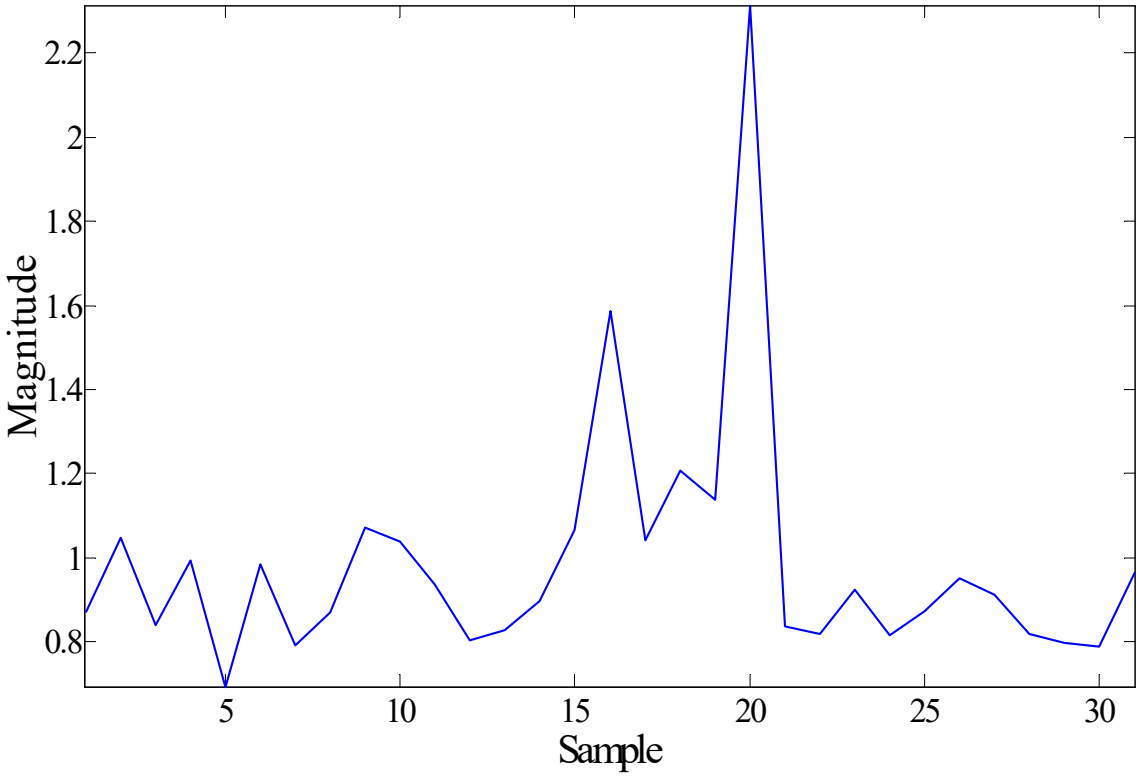

Figure 3.19: Normalized Magnitude of the Shaft-Speed oscillation in the hours before and after the vibration switch tripped on Crusher-6. Each data point was taken from a single FFT performed on a one-minute window of crusher-6 current data.

3.4 Summary

This chapter explored transient and steady-state techniques that can help diagnose the health of inertial loads using bus-level electrical measurements. Simulation and field test results demonstrated the effect of changing mass on the duration of inrush current. As the mass decreases, the value of the inertia decreases, and it reduces the in-rush period of the motor. The trending of such data can help determine the health of inertial loads, such as coal crusher. Frequency domain analysis of bus-level current provided information regarding increased vibration as well as unbalanced load due to uneven loss of mass around the motor shaft. The combination of transient and steady-state techniques can help power plant personnel determine the health of the coal crusher and support condition-based maintenance, which can help save in maintenance cost, unplanned outage cost, and optimize asset health for better plant performance.

CHAPTER 4: CASE STUDY 2 – CENTRIFUGAL PUMP AND MOTOR

Fossil, nuclear, and hydropower plants have various applications of pump-motor. The common types of critical applications in the bulk power generation plant include the boiler feedwater pump and the circulating water pump. In a nuclear power plant, the pump applications related to the cooling systems are associated with the safe operations of the plant. Some of the hydropower plants are pump storage plants where pump-motor combination stores water at height, and then as needed, the stored water is used to generate electricity. These fluid systems' health monitoring is essential for efficient, safe, and reliable operation of the power plant.

Most of the pump-motor applications in power plants are moving water for cooling and other requirements. In this case, water comes from the body of water near the plant, for example, a lake or river. There are filters at the water intake to avoid any un-intended debris to get into the system. These filters get clogged if not cleaned or replaced periodically. Clogged filters reduce the efficiency of the pump system. Over time due to the quality of the liquid moved by piping systems, and chemical interaction between the fluid and piping material, these piping systems collect deposits. These deposits or build-up of scale can affect the pressure, flow, and ultimately efficiency of these pump-motor systems. If enough deposits are gathered in one place of the piping system, it can also cause leaking or busting of the piping system under operating conditions.

The piping systems are not translucent. Consequently, the formation of deposits can't be detected during the periodic inspection. Filters are checked and replaced periodically as one of the time-based maintenance tasks. This chapter proposes a technique to detect filter clogging and accumulation of deposits in the piping system using voltage and current measurements by NILM during the startup of the pump's motor. The proposed technique uses transient electrical signals at

the main busbar to detect clogging and accumulation of scaling types of anomalies in the piping system. Consequently, this technique is more suitable for the pump that starts and stops periodically.

4.1 Background and Overview

Figure 4.1 shows the comparison between the hydraulic system and the electrical circuit. In the electrical circuit, voltage drives the flow of electrons (current) through the wires in the circuit. Voltage drops in the resistive elements of the electrical circuit. The resistive voltage drop of the electrical circuit depends on the applied voltage of the circuit, and material, length, and diameter of the wire. Much like an electrical circuit, in a hydraulic system, pressure or head (H) drives the flow (Q) of liquid through the piping system. The pressure drops in resistive elements of the piping system. This head change in the hydraulic system due to piping resistance may depend on the applied head of the system, the roughness of internal walls of the piping system, viscosity of the liquid being transferred, and the length and diameter of the piping system. When deposits in the piping system increases or filter become clogged, it replicates change in the diameter of the piping system. Consequently, it changes the value of pipe resistance.

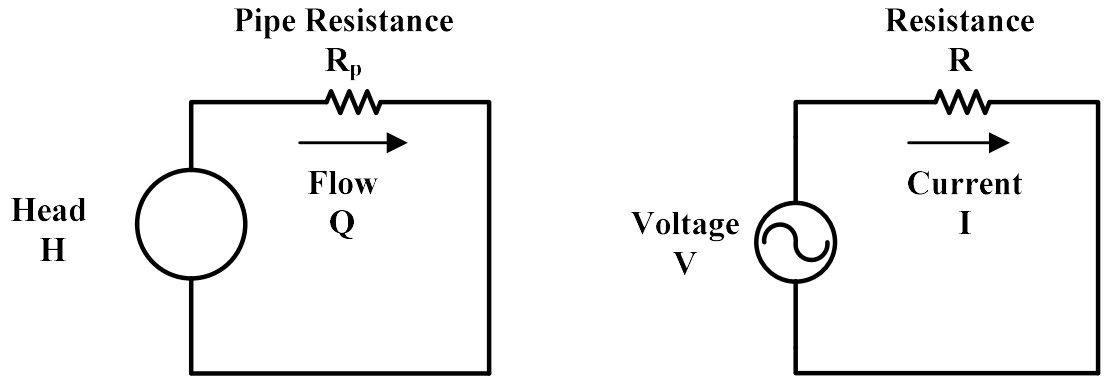

Figure 4.1: Comparison between the electrical circuit and pump fluid system.

4.1.1 Total Dynamic Head

The total head of the system has four components, suction head H_s, pressure head H_p, velocity head H_v, and friction head H_f. Figure 4.2 shows some of the elements of heads in the pump

fluid system. During the operation, this head may change; therefore, the term total dynamic head (TDH).

$$TDH = H_s + H_p + H_v + H_f \quad 4\text{-}1$$

Suction head H_s is the head at the intake pipe connected to the pump. Pressure head H_p is the pressure across the system. Pressure head may or may not exist for the pump fluid system. For the re-circulated closed-loop pump fluid system, there may be nominal pressure change across the system. Velocity head H_v and friction head H_f are the loss terms in equation 4-1. Velocity head represents the loss of energy in the system due to the velocity of the liquid in the piping system. Equation 4-2 shows the relation between velocity head, flow rate, and length and cross-sectional area of the pipe. Friction loss head H_f is due to the friction losses in the piping system. The term k_f in equation 4-3 is a friction loss constant; it depends on the viscosity of the liquid flowing through the piping system as well as geometry and properties of the piping system [55], [56] and [57]. This chapter investigates how a change in the pipe resistances will affect the transient time duration of the pump's motor. The technique is tested with simulation and laboratory tests.

$$H_v = \frac{v^2}{2g} = \frac{l}{gA}\frac{dQ}{dt} \quad 4\text{-}2$$

$$H_f = k_f Q^2 \quad 4\text{-}3$$

Where,

v: Velocity

g: Acceleration of gravity

k_f: Frictional constant

Q: Volumetric flow rate

L: Length of the piping system

A: The cross-sectional area of the pipe

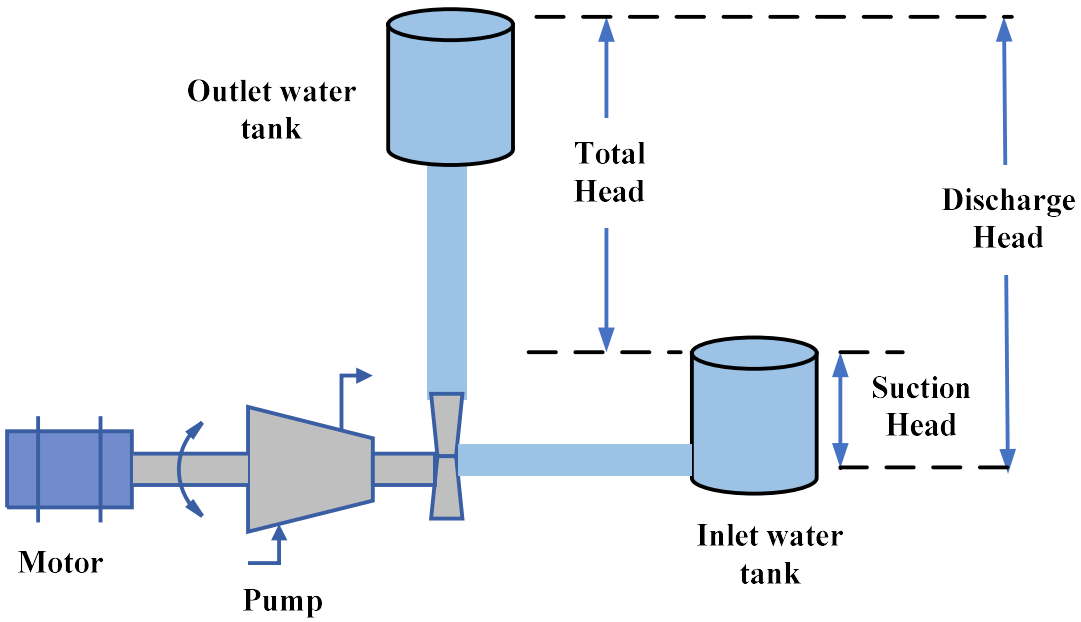

Figure 4.2: Various heads associated with pump fluid system, adopted from [58].

4.2 Simulation Test and Results

Simulation of pump motor system consisted of induction machine model and centrifugal pump model. The fifth order induction machine model is set up using equations from 3-1 to 3-6, as mentioned in the previous chapter. The output head of the centrifugal pump system shows the non-linear dependence on the flow rate Q and the speed of the motor, as shown in equation 4-4 [59] and [60].

$$h_{in}(t) = a_1 w_r^2 + a_2 \omega_r Q_{in} + a_3 Q_{in}^2 \quad 4\text{-}4$$

Where,

a_1, a_2, *and* a_3: Empirical constants

ω_r: Speed of the motor

The mechanical load torque due to centrifugal pump fluid system can also be defined as

$$\tau_l = b_1 \omega_r Q_{in} + b_2 Q_{in}^2 \quad 4\text{-}5$$

The head loss due to friction can be defined by combining H_f and H_v from equations 4-2 and 4-3,

$$h(t) = \frac{l}{gA}\frac{dQ}{dt} + k_f Q^2 \quad 4\text{-}6$$

Equations 4-4 and 4-5 provide the basis for the pump modeling, and equation 4-6 provides the basis for the head loss modeling. The simulation model was created using the induction machine and pump fluid system equations. As more deposits accumulate in the piping system, from the system perspective, the effective cross-sectional area A and frictional constant k_f changes. Thus, the increased flow resistance effect can be simulated by varying the friction loss constant k_f or changing the dimensions of the cross-sectional area A. List of the induction machine parameter used for the simulation are in Table 4.1.

Table 4.1: Parameters used for induction machine simulations [52]

Parameters	**Rating**
Output Power	3 HP
Voltage	220 V
Full-load current	5.8 A
Full-load speed	1710 RPM
Mass moment of inertia	0.089 kg-m^2
Stator resistance	0.435 Ω
Rotor resistance	0.816 Ω
Stator reactance	0.754 Ω
Rotor reactance	0.754 Ω
Magnetizing reactance	26.13 Ω

Figure 4.3 shows the simulated instantaneous power measured at the start of a 3 hp motor. As seen in this figure, there are two types of transients captured using electrical measurements. The first is electrical transient due to electromechanical system energization. The second one is mechanical transient, where current gradually increases as fluid is being filled in the piping system for the first time after motor startup. In the pump fluid system, this is a common occurrence; when the discharge valve is open, the motor current will gradually rise until the fluid is filled in the entire piping system. Once the liquid is filled in the piping system, the motor current will settle to the steady-state value. This phenomenon may be one of the reasons for closing the discharge valve for the first few seconds when the diesel generator is providing power to the pump's motor during the loss of off-site power startup procedure in a nuclear power plant.

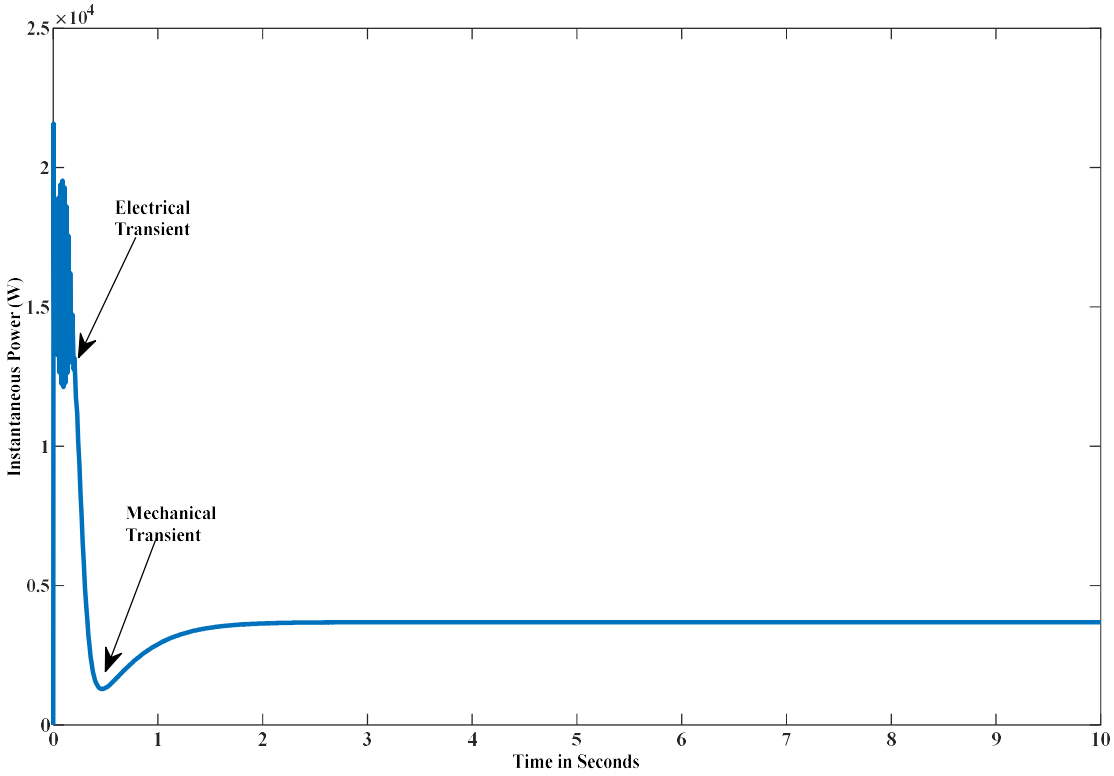

Figure 4.3: Simulated instantaneous power at the start of the 3 HP motor.

In this simulation, change in fluid system resistance was simulated by varying the value of pipe cross-sectional area A and friction constant k_f. Figure 4.4 shows the results of the simulation. As shown in this figure, a higher value of fluid system resistance reduces the duration of mechanical transient. The solid trace in that figure is for the lowest fluid system resistance, and it has the highest mechanical transient time duration. The dotted trace is for the highest fluid system resistance, and it shows almost no mechanical transient time duration. Noticeably, there is no-change in electrical transient time duration. The top of Figure 4.4 also shows that as the resistance increases, the steady-state power consumed by motor decreases. Similarly, the bottom of Figure 4.4 shows the change in flow rate (Q) for changing fluid resistance values. The volumetric flowrate reaches to final value faster for the highest fluid system resistance, as seen in the dotted trace. This bottom image also shows that as the resistance of the system increases, the steady-state value of volumetric flow decreases.

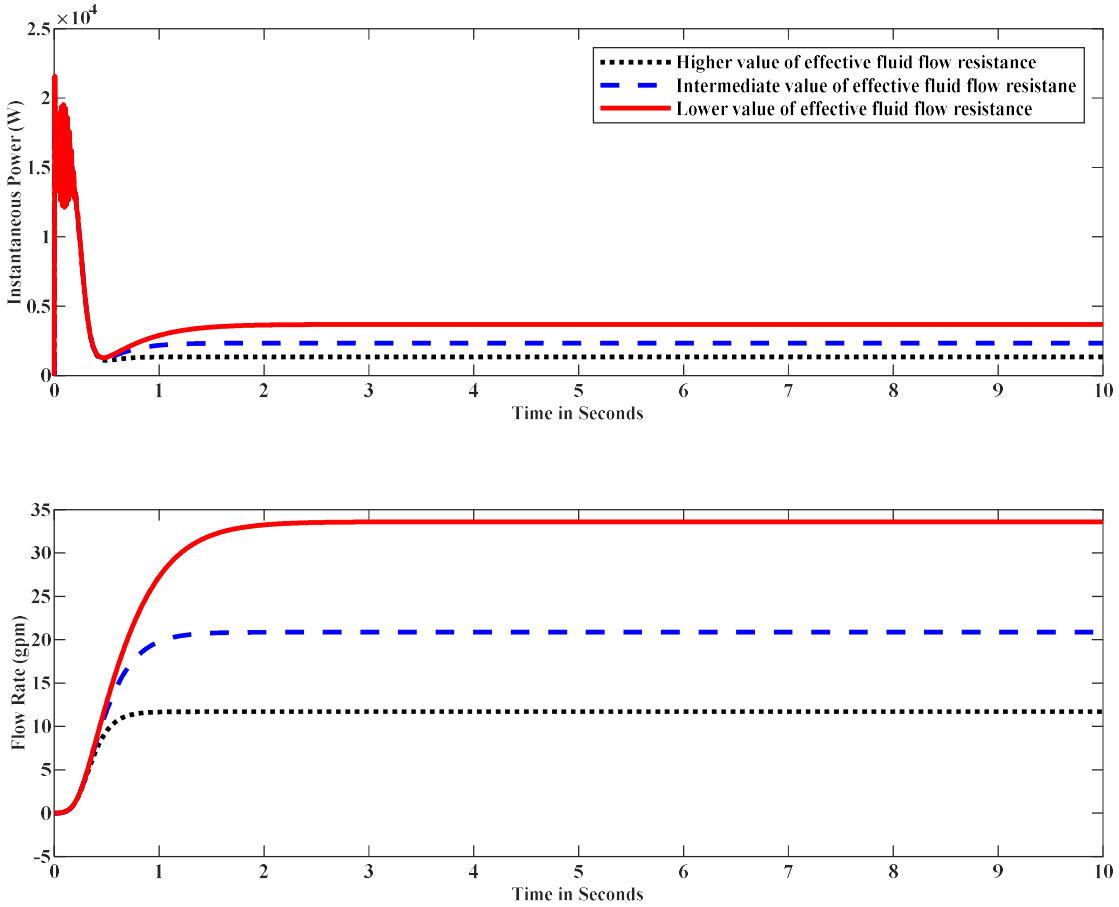

Figure 4.4: Simulation results showing the effect of changing fluid system resistance on electrical and mechanical transient acquired from electrical measurements. The top picture shows the instantaneous power for various values of the effective fluid flow resistance. The bottom image shows the change in volumetric flowrate with changing the effective fluid flow resistance.

4.3 Laboratory Tests and Results

Figure 4.5 shows the laboratory layout for the centrifugal pump's re-circulating water closed-loop system, and Figure 4.6 shows the picture of the laboratory setup. The reservoir that fed the inlet of the pump was also the storage for the pumped water, thus water re-circulating, closed-loop system. As shown in these figures, there are four 1-inch PVC ball valves installed around the piping system. Piping was almost 50 feet long; it was installed at different elevations, as shown in the picture of the laboratory setup Figure 4.6. The location of the valve V_1 was near the pump discharge, valve V_2 was almost in the middle of the piping system, and valve V_3 was near the reservoir. These valves were used to simulate the change in the effective resistance of the fluid

system. Valve V_0 near to the pump inlet was not used to change the resistance of the fluid system. Gould's MCC series pump and 1 HP motor were used for this experiment. Table 4.2 shows the specifications of the pump-motor system.

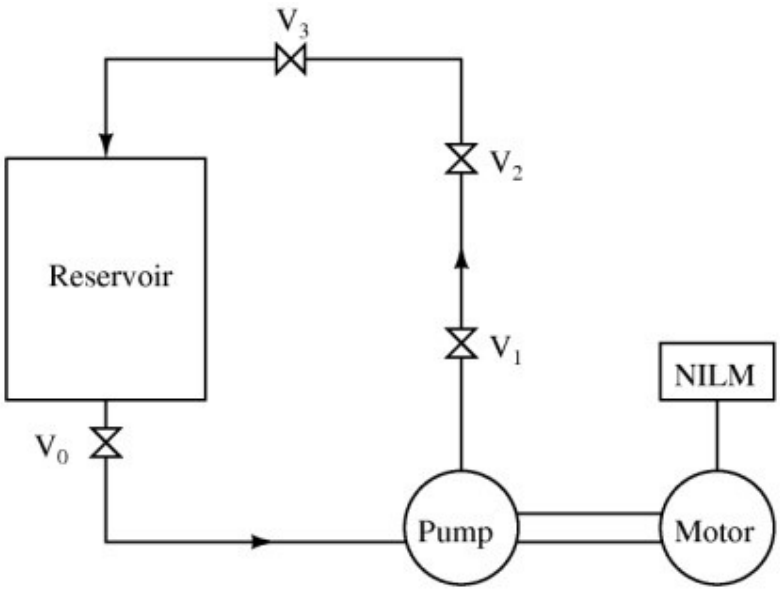

Figure 4.5: Closed-loop centrifugal pump system laboratory layout.

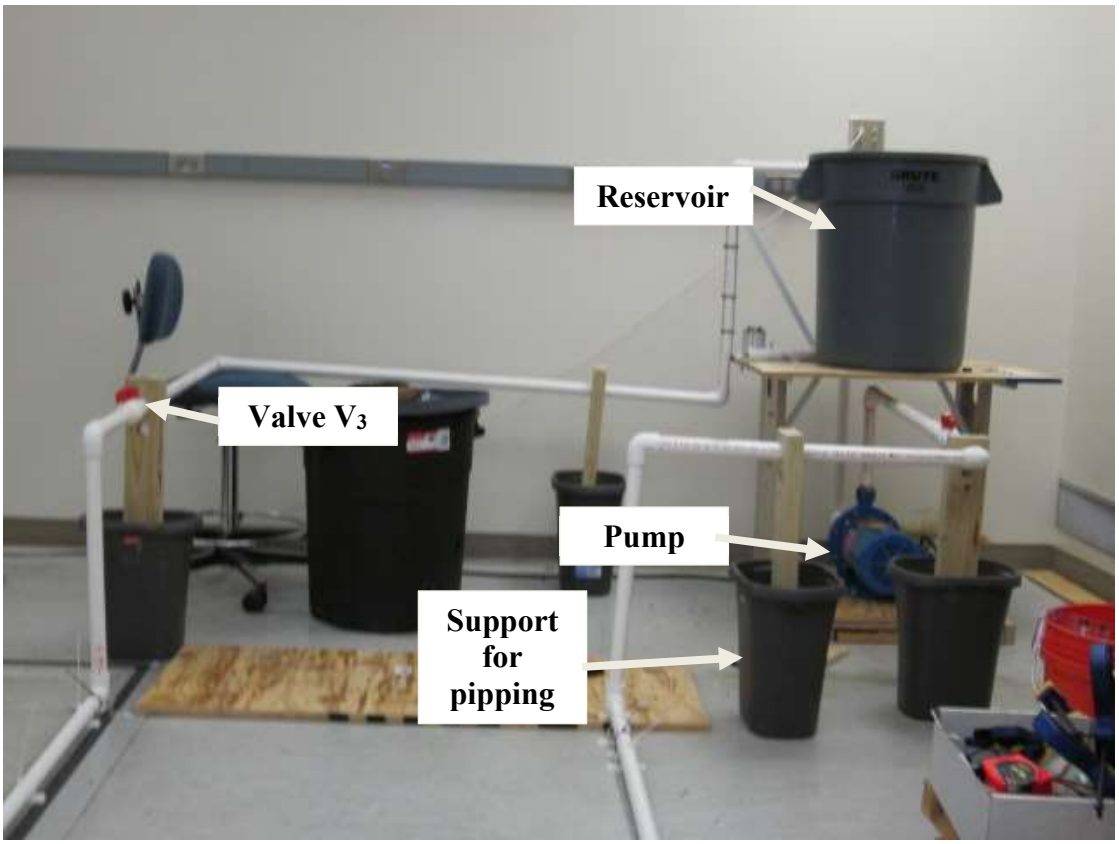

Figure 4.6: Picture of the actual laboratory setup for centrifugal pump closed-loop system.

Table 4.2: Pump motor specifications.

Parameter	Rating
Power rating	1 HP
Voltage Rating	460 V
Full-load current	1.7 A
Full-load speed	3450 RPM

Experiments were conducted by varying the valve positions to simulate the resistance of the fluid system. The electrical measurements of the motor's stator currents and supply voltages were acquired using NILM. Figure 4.7 shows the instantaneous power measurement of 1 HP three-phase induction motor connected to the pump. As seen in this figure, varying valve positions to change the effective fluid system resistance varies the mechanical transient time duration. As seen in the figure, various positions of the valve include; fully open, about 50% closed, and approximately 75% closed. This figure looks similar to the simulation results of the 3 hp motor shown in Figure 4.4. As shown in this figure, the increase in effective resistance of the fluid system

decreases the mechanical transient duration. There is a substantial difference between fully open to almost 50% and 75% closed. When all three valves are about 75% closed, the mechanical transient almost disappears.

Additional trace with the valves about 25% closed is also included in Figure 4.8 and Figure 4.9. Essentially, Figure 4.9 is a zoomed-in version of Figure 4.8 near mechanical transient. As seen in these figures, the mechanical transient time duration change is not significant between fully open valves to about 25% closed. However, it is still a noticeable change, as seen in Figure 4.9. These figures also confirm that the steady-state power level also reduces with higher fluid system resistance.

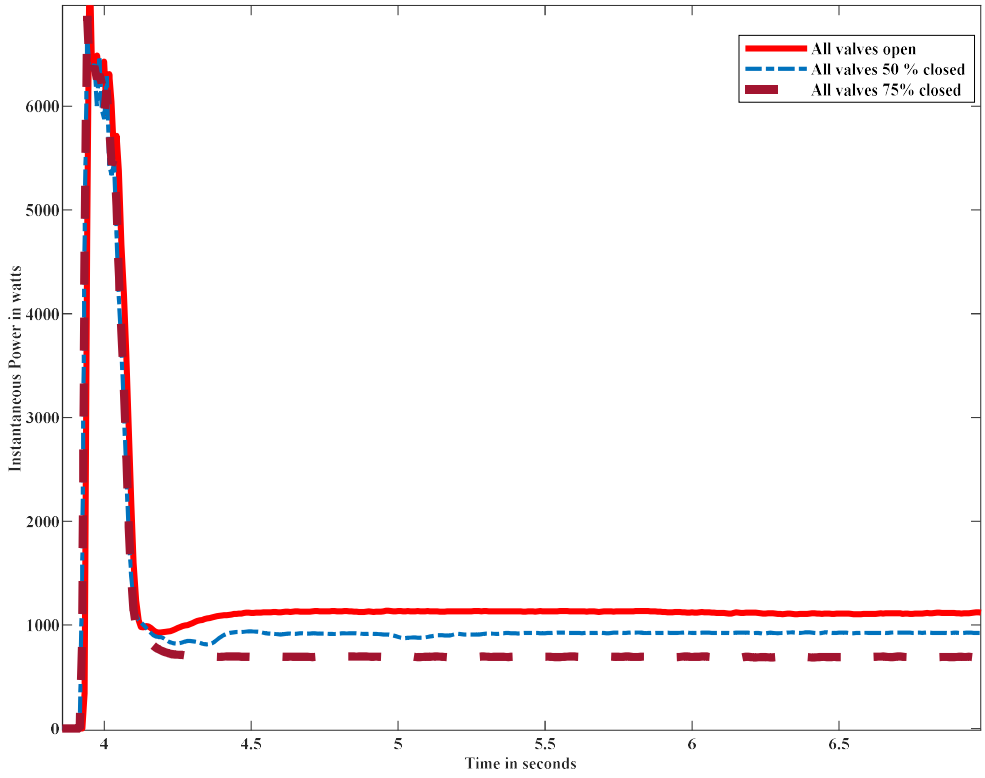

Figure 4.7: Traces of the pump motor's instantaneous power showing the change in the transient time duration when the motor is started with all four valves in open position, 3 of the valves are closed at around 50% and 75%, replicating increase in the effective resistance of the fluid system.

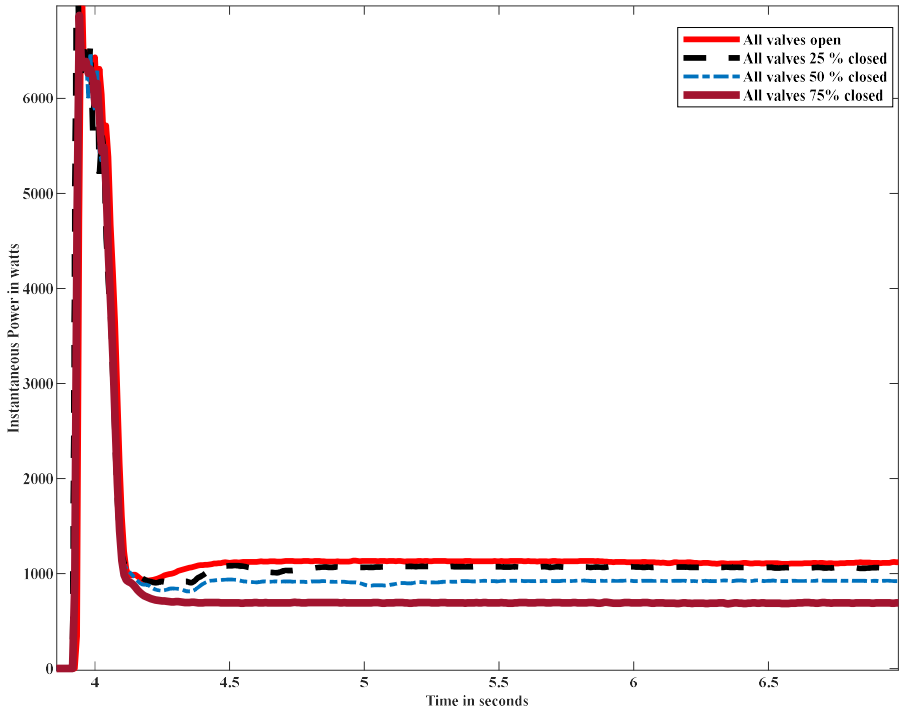

Figure 4.8: Traces of the pump motor's instantaneous power showing the change in the transient time duration when the motor is started with all four valves in open position, 3 of the valves are closed at around 25%, 50%, and 75%, replicating increase in the effective resistance of the fluid system.

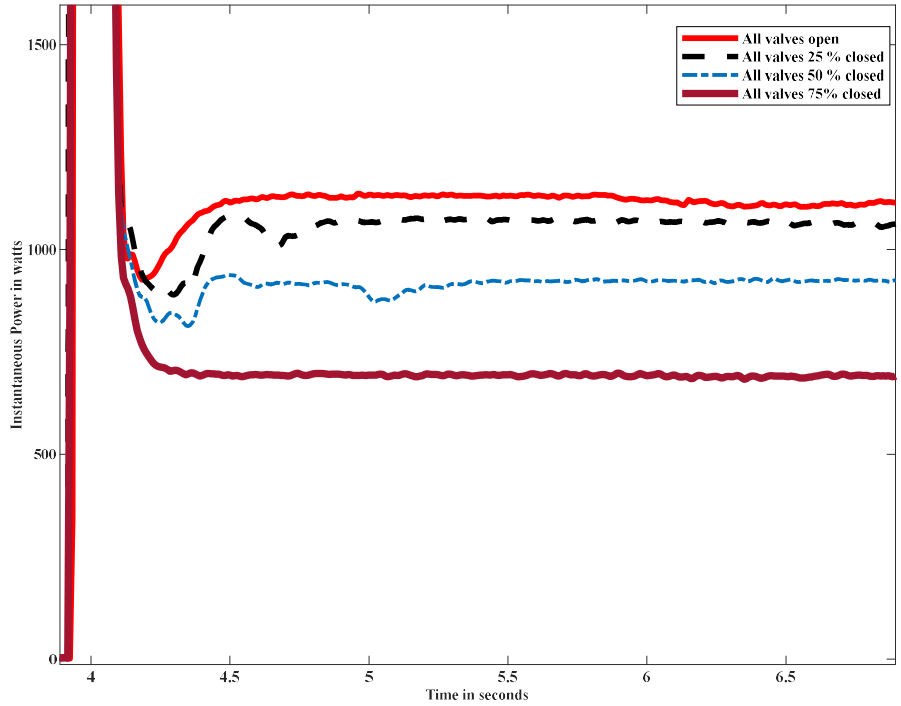

Figure 4.9: Traces of the pump motor's instantaneous power specifically showing the change in the mechanical transient time duration when the motor is started with all four valves in open position, 3 of the valves are closed at around 25%, 50%, and 75%, replicating increased effective resistance of the fluid system.

Figure 4.10 shows the potential transient-based algorithm that can be implemented to detect the accumulation of deposits in a fluid piping system using the transient-based measurement of current. As seen from Figure 4.7 to Figure 4.9, as the scale accumulates in the piping system, the mechanical transient duration decreases. Trending the value of this transient duration at every startup can help determine the relative accumulation of deposits in the fluid system piping. Power plant personnel can schedule the invasive inspections at the nearest convenient time when the transient time duration decrease at a specific threshold value set by plant personnel. This condition-based invasive inspection can save the plant in maintenance costs and avoid any catastrophic failure during the operations.

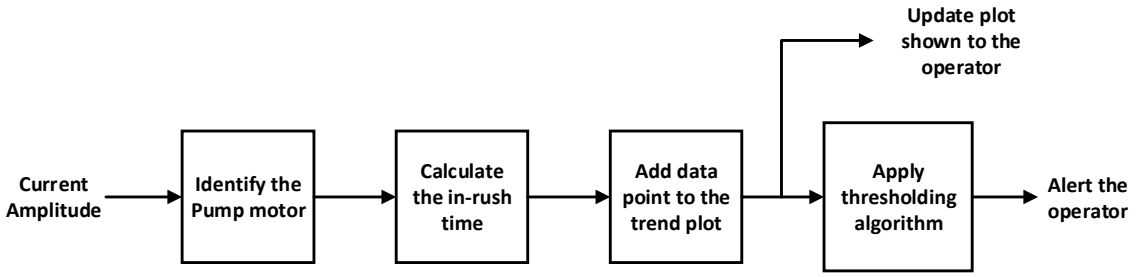

Figure 4.10: Potential transient-based algorithm to detect the accumulation of deposits in a fluid pump system.

4.4 Summary

The technique presented in this chapter is a non-invasive monitoring technique that can help determine the clogging of the piping system and obstructed flow in the pump fluid system using bus-level electrical measurements. NILM was used to acquire electrical measurement of stator currents and voltages. This method is particularly helpful for the pump motor that starts often. A comparison between consecutive transient time durations can give a relative measure of obstructed flow. This comparison can help power plant personnel in scheduling the maintenance or invasive inspection during the outage of the power plant. This condition-based invasive inspection can save potential maintenance, repair, and refurbishment cost compared to unintended bursting or leaking of the piping system during the operation.

CHAPTER 5: INDUCTION MACHINE PARAMETER ESTIMATION - SUMMARY OF PAST RESEARCH

There are mainly two types of applications for the induction machine parameter estimations, rotor field-oriented control, and power system stability studies. A high-performance variable speed drive requires knowledge of some of the induction machine parameters for control purposes. The knowledge of induction machine parameters also supports the efficient operation of a variable frequency drive. Power system stability studies that require knowledge of induction machine parameters include black start capability, loss of off-site power unit, and various regulatory modeling and simulations requirements. Many researchers have researched in developing techniques that cater to the needs of these applications. This chapter is an overview of the past research to determine parameters of the induction machine, focused on power system stability studies.

Figure 5.1 shows the commonly used single-line induction machine equivalent circuit per the IEEE standard 112 [61]. Table 5.1 describes parameters associated with this electrical circuit.

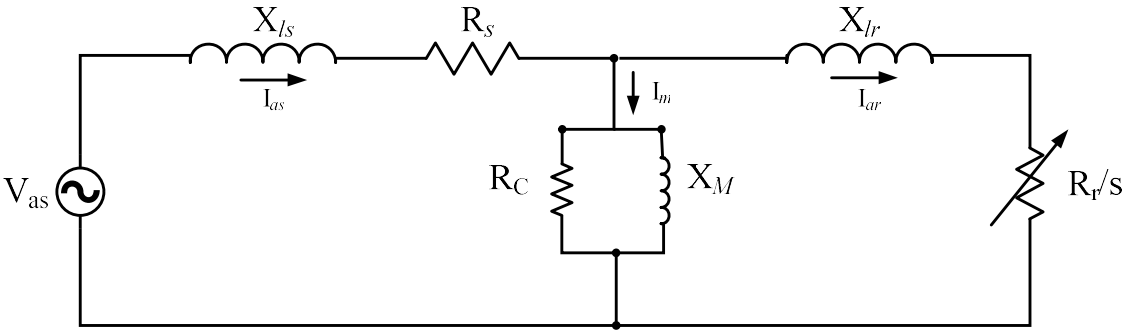

Figure 5.1: Simplified single-line diagram of the induction machine equivalent circuit, adopted from [61].

Table 5.1: The induction machine equivalent circuit parameters.

Parameter	Description
X_{ls}	Stator leakage reactance
X_{lr}	Rotor leakage reactance
R_s	Stator resistance
R_r	Rotor resistance
X_M	Magnetizing reactance
R_c	Core resistance
V_{as}	Supply voltage
I_{as}	Stator current
I_{ar}	Rotor Current
I_M	Magnetizing current

Once the induction machine parameters are determined, it can be used with the available software to study power system stability; for example, to determine power flow, changes in voltage, and changes in frequency during disturbances in the system. This information helps with planning for the starting sequence of large auxiliary loads during cold start as well as black start and setting up protection relays. There are several types of research conducted in the area of induction machine parameter estimation. Electromagnetic Transients Program (EMTP), and Electrical Transient Analysis Program (ETAP) are examples of widely used software to analyze power system stability. The software used for power system stability study are also used for determining the induction machine parameters in powerplant. These software estimates parameters based on available manufacturer data. The following section discusses past researches related to these widely used methods in power plants to determine the parameters of the induction machine. In addition, it also provides a brief overview of other investigations in the area of techniques to estimate induction machine parameters.

5.1 Techniques to Estimate Induction Machine Parameters

The induction machine parameters are not generally provided by the manufacturer unless specified in the request for procurement (RFP) by the buyer of the machine. Commonly, at the manufacturing facilities, these circuit parameters are obtained using methods documented in IEEE standard 112 [61]. In many cases, even if the parameters are provided during the buying process of

the machine, they are lost. Prominent methods used in power plants for induction machine parameter estimation are described in [62], [63], [64], [65] and [66]. To anonymize the commercially available techniques, they are referred to as technique-1 and technique-2 in the following sections.

5.1.1 Widely Used Parameter Estimation Technique – 1

A review of this technique for the induction machine parameter estimation is based on the references [62], [64], and [66]. As most of the large induction machines are with deep-bar rotor design, it can be represented with a double cage induction machine equivalent circuit model. In the literature for the parameter estimation technique-1, a double cage induction machine model is considered. The one-line diagram for such a machine is shown in Figure 5.2. As seen in this figure, the core resistance is neglected, and small leakage reactance of the outer cage is also ignored.

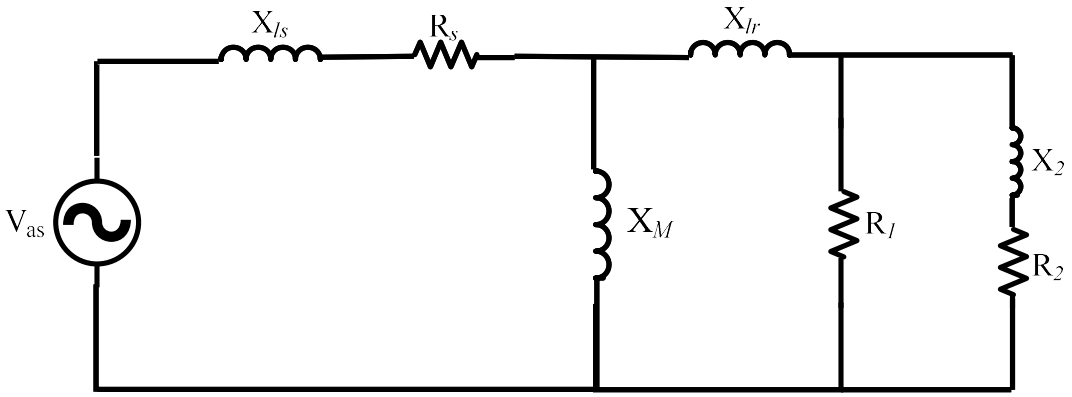

Figure 5.2: Simplified model of double cage induction machine equivalent circuit, adopted from [62].

Table 5.2 shows the manufacturer and nameplate induction machine information needed for the estimation of some of the parameters. As mentioned earlier, the core resistance and outer cage leakage reactance are neglected. Parameter estimations are made using per unit (pu) system. The following is a basic summary of the steps in this method to estimate the parameters [62]:

- The total windage, core, and friction losses are assumed to be 25% of the total losses. Full-load efficiency is adjusted to η' to reflect this assumption.

$$\eta' = 0.25 + 0.75\eta \qquad 5\text{-}1$$

- Parameters R_s, R_r, and X_M are estimated based on adjusted value of efficiency η', full-load power factor, and slip.
- Starting resistance R_{st} is estimated based on the values of starting torque T_{st} and current I_{st}.
- Rotor resistance R_r is estimated based on values of R_{st} and ratio of starting torque T_{st} to rated torque T.
- The assumption is made regarding the ratio of total inner and outer cage resistance to inner cage leakage reactance "m" between 0.5 to 0.6.

$$m = \frac{R_1 + R_2}{X_2} \quad \text{5-2}$$

- Values of R_1, R_2, and X_2, are estimated based on the value of "m" and rotor resistance R_r.
- Estimation of total starting reactance X_t

$$X_t = \sqrt{\left(\frac{V}{I_{st}}\right)^2 - (R_s + R_{st})^2} \quad \text{5-3}$$

- In case the saturation current value is unavailable; the saturated current I_{sat} is assumed twice the full-load current. As per the rotor bar design of the induction motor, the describing function is calculated. The describing function is developed in [66].
- Based on describing function values and saturated current value, the total reactance X_t, stator, and rotor leakage reactance are recalculated.
- Using Thevenin's equivalent circuit for the induction motor, X_M and R_r recalculated to account for the saturation.
- Based on all of the estimated circuit parameters, the value of maximum torque T_{max} is calculated. The maximum torque T_{max} value provided by the manufacturer is compared with the estimated value of T_{max}.
- If the estimated value of T_{max} is not almost equal to the T_{max} value provided by the manufacturer, iteratively adjust saturated current value I_{sat} and recalculate all of the circuit

parameters shown in Figure 5.2 until the estimated value of maximum torque matches with the value provided by the manufacturer.

- In addition to the above iterative process, the algorithm also requires mechanical model data for the accurate parameter estimation. This mechanical model data include the moment of inertia and friction coefficient of the load.

Table 5.2: List of required parameters before initiating parameter estimation calculations.

Parameter	Description
V	Rated Voltage
I	Full-load Current
NEMA motor Type	NEMA motor design type
I_{st}	Starting Current / Locked rotor Current
I_{sat}	Saturation Current (if available)
PF	Full-load power factor (cos φ)
s	Full-load slip
T	Rated or full-load torque
T_{max}	Maximum or Break down torque
T_{st}	Starting Torque or Locked rotor Torque
η	Full-load efficiency
m	The ratio of inner cage leakage reactance to the total of inner and outer cage resistance
J	Motor moment of inertia
β	Friction co-efficient of load

The method described in [64] is similar to the process described in [62]. In addition to the manufacturer data in Table 5.2, the method in [62] also uses the following manufacturer-provided information to reduce error in estimated induction machine parameters [64]:

- Current Vs. Slip characteristic
- Torque Vs. slip characteristics
- Power factor Vs. slip characteristic

5.1.2 Widely Used Parameter Estimation Technique – 2

The process used in this technique to estimate induction machine parameters is described in [63]. The value of α calculated using the following equation and values derived above

$$R_{rlr} = (1 + \alpha S_{lr}) R_{rfl} \qquad 5\text{-}10$$

- As the magnetizing branch is removed from the equivalent circuit, the stator leakage reactance Xls, the rotor leakage reactance Xlr, and the stator resistance Rs can be calculated at locked rotor condition using the following equation:

$$(X_{ls}+ X_{lr})= \left(\frac{V}{I_{slr}}\right) \sin \varphi_{lr} \qquad 5\text{-}11$$

$$(X_{ls} + X_{lr}) = \sqrt{\left(\frac{V}{I_{slr}}\right)^2 - (R_s+ R_{rlr})^2} \qquad 5\text{-}12$$

- As suggested in IEEE standard 112 [61], the ratio $\frac{X_{ls}}{X_{lr}}$ for different NEMA motor design as follow:

Type A and D: 1

Type B: 2/3

Type C: 3/7

- In the next step, this method finds XM while continue to exclude core resistance Rc [65] from the induction motor equivalent circuit.
- In this method, XM is derived using the iterative process. The full-load power factor is calculated from the estimated electrical circuit parameters. This calculated full-load power factor is compared with the full-load power factor provided by the manufacturer. The value of XM modified until the manufacturer provided full-load power factor and estimated full-load power factor match.
- Using these initial values of circuit parameters, values of rotor full-load current Irfl and slip at full-load Sfl are updated.
- Core losses are estimated using known values of power as well as estimated heat losses using calculated current and resistance values.

- Core resistance Rc was determined using Thevenin's equivalent circuit and the estimated value of core losses. The Thevenin's circuit was derived by combining the magnetizing branch with the stator circuit.
- Once the initial values of the parameters are determined, the final parameter values are calculated using the sensitivity analysis of each parameter. The sensitivity analysis is performed using known variable PF, Tmax, STm, Tlr, Islr, PFlr, and η with estimated parameter Xls, Xlr, Rs, Rrfl, XM, Rrlr, Xrfl, and Rc.

shows the list of the manufacturer data and nameplate data required to initiate the process of induction machine parameter estimation. In this method, researchers have used the IEEE standard 112 induction machine model equivalent circuit shown in Figure 5.3.

Table 5.3: List of required parameters before initiating parameter estimation calculations.

Parameter	Description
V	Rated Voltage
I	Full-load current
NEMA motor Type	NEMA motor design type
PF	Full-load power factor (cos φ)
η	Full-load efficiency
T	Rated or full-load torque
T_{max}	Maximum or Break down torque
S_{Tm}	Slip at maximum or breakdown torque
T_{lr}	Starting torque or locked rotor Torque
I_{slr}	Stator current at locked rotor
PF_{lr}	Locked rotor power factor (cos φ_{lr})
J	Motor moment of inertia
β	Friction co-efficient of load

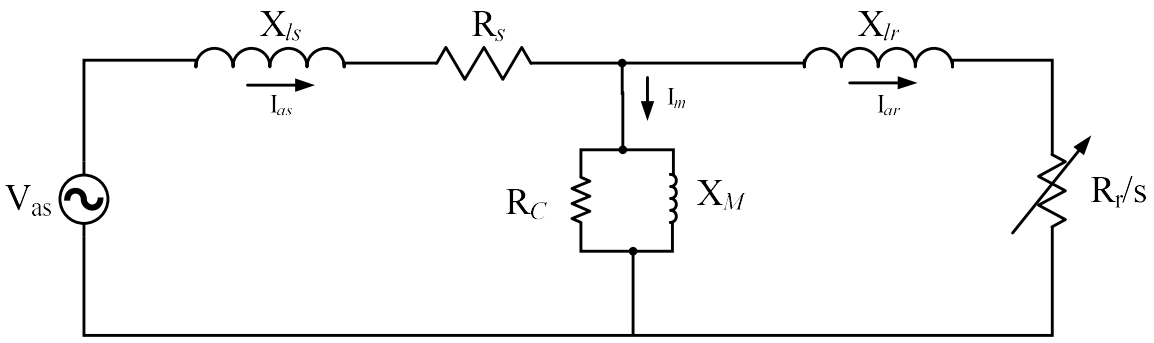

Figure 5.3: Simplified model of induction machine equivalent circuit, adopted from [61].

This method uses a per unit (pu) system for induction machine parameter estimation. The following is an elementary summary of the steps in this method to estimate the parameters [63]:

- Initially, the circuit is simplified by removing the magnetizing branch of the equivalent circuit and obtain the rest of the parameters. These parameters will be later used for the estimation of magnetizing branch parameters.
- Rated voltage V, rated or full-load stator current I_s, and rated or full-load torque T was set at 1pu.
- Values of rotor current at full-load I_r and at locked rotor I_{rlr} as well as full-load slip were assumed as follow,

$$I_r=0.95I_s \quad (5\text{-}4)$$

$$I_{rlr}=0.95I_{slr} \quad (5\text{-}5)$$

$$S=1.5\% \quad (5\text{-}6)$$

- Using assumed values of full-load rotor current, locked rotor current and slip from above, the values of full-load rotor resistance R_{rfl} and rotor resistance at locked rotor R_{rlr} were calculated as,

$$R_{rfl}=\frac{ST}{I^2} \quad (5\text{-}7)$$

$$R_{rlr}=\frac{ST_{lr}}{I_{rlr}^2} \quad (5\text{-}8)$$

- Rotor resistance R_{rot} approximated with the following equation, where α is between 0 to 3 depending on deep bar or double cage design.

$$R_{rot}=(1+\alpha S)R_{rfl} \quad (5\text{-}9)$$

- The value of α calculated using the following equation and values derived above

$$R_{rlr} = (1 + \alpha S_{lr})R_{rfl} \quad (5\text{-}10)$$

- As the magnetizing branch is removed from the equivalent circuit, the stator leakage reactance X_{ls}, the rotor leakage reactance X_{lr}, and the stator resistance R_s can be calculated at locked rotor condition using the following equation:

$$(X_{ls}+ X_{lr})= \left(\frac{V}{I_{slr}}\right) \sin \varphi_{lr} \quad 5\text{-}11$$

$$(X_{ls} + X_{lr}) = \sqrt{\left(\frac{V}{I_{slr}}\right)^2 - (R_s+ R_{rlr})^2} \quad 5\text{-}12$$

- As suggested in IEEE standard 112 [61], the ratio $\frac{X_{ls}}{X_{lr}}$ for different NEMA motor design as follow:

Type A and D: 1

Type B: 2/3

Type C: 3/7

- In the next step, this method finds X_M while continue to exclude core resistance R_c [65] from the induction motor equivalent circuit.
- In this method, X_M is derived using the iterative process. The full-load power factor is calculated from the estimated electrical circuit parameters. This calculated full-load power factor is compared with the full-load power factor provided by the manufacturer. The value of X_M modified until the manufacturer provided full-load power factor and estimated full-load power factor match.
- Using these initial values of circuit parameters, values of rotor full-load current I_{rfl} and slip at full-load S_{fl} are updated.
- Core losses are estimated using known values of power as well as estimated heat losses using calculated current and resistance values.

- Core resistance R_c was determined using Thevenin's equivalent circuit and the estimated value of core losses. The Thevenin's circuit was derived by combining the magnetizing branch with the stator circuit.
- Once the initial values of the parameters are determined, the final parameter values are calculated using the sensitivity analysis of each parameter. The sensitivity analysis is performed using known variable PF, T_{max}, S_{Tm}, T_{lr}, I_{slr}, $PF_{lr,}$ and η with estimated parameter X_{ls}, X_{lr}, R_s, R_{rfl}, X_M, R_{rlr}, X_{rfl}, and R_c.

5.1.3 Other Researches in Parameter Estimation Techniques

Induction machine parameter estimation has many applications; as such, there are numerous researches available in the journals and conference papers. This section will summarize various other investigations and techniques to determine induction machine parameters. There are mainly two categories for the application of induction machine parameters; to control high-performance variable frequency drives and in the power plant to determine voltage and power flows during disturbances of the power system.

Reference [67] provides an induction motor model that represents motor performance over a wide range of frequencies. This model can be applied for induction motor control purposes. Reference [68] provides a method to estimate induction machine parameters using stand-still measurements that can be helpful for variable frequency drive operations. Reference [69] provides an overview of many techniques for induction machine parameter estimation used in the control applications. Almost all of the methods mentioned in [69] for control applications require a variable frequency drive to estimate induction machine parameters. Moreover, most of the technologies are off-line. The techniques are implemented at the commissioning of the variable frequency drive. The electrical circuit parameter values are derived at the commissioning of the drive. Very few technologies

support re-calculations or verification of the induction machine parameters while the machine is in-service. Reference [70], provides an on-line non-linear least square approach to determine the parameters of an induction machine. This approach uses a dynamic induction machine model with rotor position measurements and measurements of all three-phase currents and voltages. It provides experimental results of 0.5 hp motor that shows a comparison between actual measurement of stator current and simulated stator current using estimated parameters.

There Reference [71], discusses another on-line approach using a two-step method for induction machine parameter estimation. This method uses measurements of stator currents as well as two sets of initial guesses. The first set of initial estimates are based on information provided by the manufacturer of the machine. This first set of guesses considered poor initial estimates for this method. The second set of initial guesses is calculated by applying the non-linear least-squares technique and the first set of poor guesses. In the final step, it calculates the last set of parameters by applying a non-linear least-square method with the second set of parameter guesses. Experimental results of this research provided a comparison between actual measurements of currents and calculated current based on estimated parameters of 1 hp motor connected to a fan. This research estimates electrical parameters of the induction machine equivalent circuit and estimates of mechanical parameters, such as friction co-efficient of load and moment of inertia of the rotor. Reference [72], discusses the importance of double cage model for induction machine parameter estimation. It also provides regression equations derived from numerous American and European motor catalog data. These regression equations are used to estimate parameters of similar rating motors from their mechanical power output and

voltage rating. Reference [73], provides another method to determine induction machine parameters using manufacturer and nameplate data. The use of transient stator current for estimation of the induction machine's electrical parameter is proposed in [74]. This paper provides simulation results as well as results from the 5 hp motor. The research discussed in [75] provides a mathematical approach to determine induction machine parameters with polynomial fraction regression. Experimental results from the 0.5 hp motor induction machine parameter were presented in [75].

5.2 Summary

This chapter of the thesis provided an overview of the various past researches. Methods developed in [62], [63], [65] and [66] are widely used methods in power plants. Methods discussed in [67-70] are suitable for control applications, and methods discussed in [71-75] are suitable for power plant applications. Some key points from this review are as follows:

- Techniques widely used in power plants for induction machine parameter estimation are off-line techniques. Moreover, it requires manufacturer data, motor nameplate data, and a relatively accurate model of mechanical parameters.
- Most of the induction parameter estimation methods estimate electrical parameters of the motor and not the mechanical load parameters.
- Methods used for control applications require variable speed drive for induction machine parameter estimation.
- Many of the techniques for induction machine parameter estimation reviewed in this chapter employs an iterative process to estimate parameters.
- Many of the researches described in these references, provided experimental results of the three-phase low voltage induction motors ranging from 0.5 hp to 5 hp. References related to the widely used parameter estimation techniques in power plant also provided experimental results of medium voltage induction motor applications.

CHAPTER 6: PROPOSED INDUCTION MOTOR PARAMETER ESTIMATION TECHNIQUE

Generally, a diesel generator is responsible for providing power to the auxiliary loads during the black start unit startup process and, in the case of the nuclear unit, during the shutdown process due to loss of off-site power (LOOP). Induction motors are one of the significant auxiliary loads that needs be startup using diesel generator provided power. Maintaining demand and supply balance is very important during the startup of induction motor loads. Knowledge of induction machine inrush current time duration and the load flow due to these motors' startup is critical in maintaining supply and demand balance during the black start unit or nuclear unit's loss of off-site power startup. The induction motor parameters are used with the widely used algorithms to predict transient current amplitudes as well as load flow analysis. This type of analysis is particularly useful for the black start unit [28, 32] and for nuclear units to proceed with a safe turndown in case of loss of off-site power.

6.1 Proposed Induction Motor Parameter Estimation Technique

As discussed in Chapter 5, widely used techniques in power plants for induction machine parameter estimation require a significant amount of manufacturer data, nameplate data, and mechanical modeling of the load. However, these manufacturer data and mechanical modeling data are not readily available. In some cases, these required data may never have been provided by the manufacturer of the induction machine and mechanical load (example; pump, fan, etc.), or the utility over the years may have misplaced it. If needed, utilities will have to request the manufacturer for the data. In case the manufacturer doesn't exist anymore, the utility will need to carry out testing of the individual machine to get this information. Besides, when the changes are made in the mechanical load or motor, a new set of data needs to be verified and entered into the

software for calculation of parameters before it can be used for modeling purposes. This data gathering process can be time-consuming and costly in many cases.

This chapter proposes a novel method to estimate an induction machine parameter using the electrical data gathered at the bus-level using NILM. It is the same voltage and current data that can be used for diagnostics purposes. It is a non-invasive on-line parameter estimation technique that can help utilities with black start units as well as nuclear units.

The following section discusses the NILM's ability to calculate the in-phase and quadrature-phase component of an induction machine's stator current. This unique ability of NILM is instrumental in estimating the parameters of an induction machine.

6.1.1 Spectral Envelope of Measured Induction Motor Stator Current

This capability of NILM is also mentioned in Chapter 2; however, it is essential to emphasize this useful capability of the NILM. The unique approach of this proposed parameter estimation technique relies heavily on NILM's ability to calculate the measured current signal's spectral envelopes. NILM's pre-processor decomposes the current signal acquired at the bu-level. The measured current can be viewed as a waveform $i(\tau)$, and it can be described with arbitrary accuracy at time $\tau \in (t-T, t]$ using a Fourier Series of time-varying signal's spectral coefficients $a_k(t)$ and $b_k(t)$ [34], [35], [36] and [37]. In this context, measured current can be presented as follow:

$$i(t-T+s) = \sum_k a_k(t) \cos\left(k\frac{2\pi}{T}(t-T+s)\right) + \sum_k b_k(t) \sin\left(k\frac{2\pi}{T}(t-T+s)\right) \qquad 6\text{-}1$$

In equation 6-1 variable k ranges over the set of positive integers, T is the fundamental period of the waveform, and $s \in (0, T]$. Traditional Fourier series analysis assumes that the frequency and phase of the waveform remain the same at any time. However, that is not true for this application, where current waveform amplitude and phase changes as load changes. Equation 6-1 takes these load changes into account. In this equation, at any time t, the waveform can be represented by a set of harmonically related in-phase and quadrature-phase sinusoids that extend

over the previous period. The coefficients $a_k(t)$ and $b_k(t)$ are calculated using equations 6-2 and 6-3 [36, 37]. These co-efficients provide time-local information of amplitude and phase of the measured current spectral. If the voltage remains relatively constant, then the coefficients in-phase component $a_k(t)$ and quadrature-phase component $b_k(t)$ has useful interpretation as active and reactive component of the current. This relationship of in-phase and quadrature-phase component is used for determining power factor of the induction machine in this thesis.

$$a_k(t) = \frac{2}{T}\int_0^T i(t-T+s)\cos\left(k\frac{2\pi}{T}(t-T+s)\right) \quad 6\text{-}2$$

and

$$b_k(t) = \frac{2}{T}\int_0^T i(t-T+s)\sin\left(k\frac{2\pi}{T}(t-T+s)\right) \quad 6\text{-}3$$

Figure 6.1 and Figure 6.2**Error! Reference source not found.** respectively shows the fundamental frequency in-phase and quadrature-phase stator current component of 100 hp induction motor. Figure 6.3 shows the stator current envelope of the 100 hp motor. These time-varying spectral coefficients of fundamental frequency in-phase component $a_1(t)$ and quadrature-phase component $b_1(t)$ can be interpreted as fundamental frequency active and reactive components of the current. One of the uses of this fundamental in-phase and quadrature-phase components in induction machine parameter estimation is to determine the power factor of the machine for varying conditions. The use of measured electrical signals allows the estimation of parameters at every

start, unlike other methods where parameters are estimated only once during the commissioning or off-line when it is required for modeling or load flow analysis.

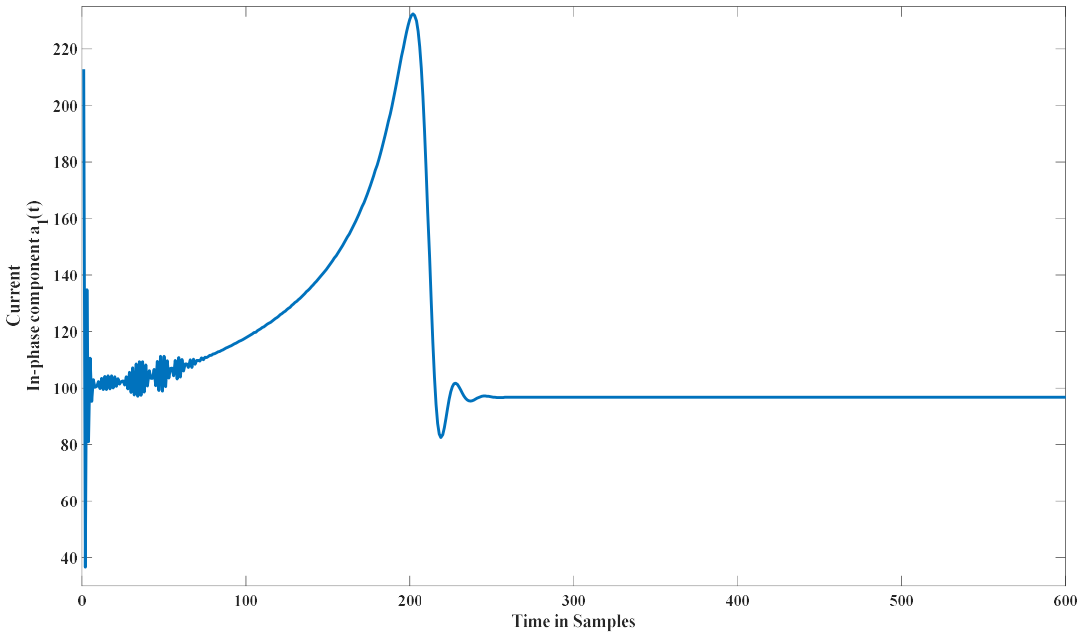

Figure 6.1: Fundamental in-phase component $a_1(t)$ of 100 hp induction motor stator current.

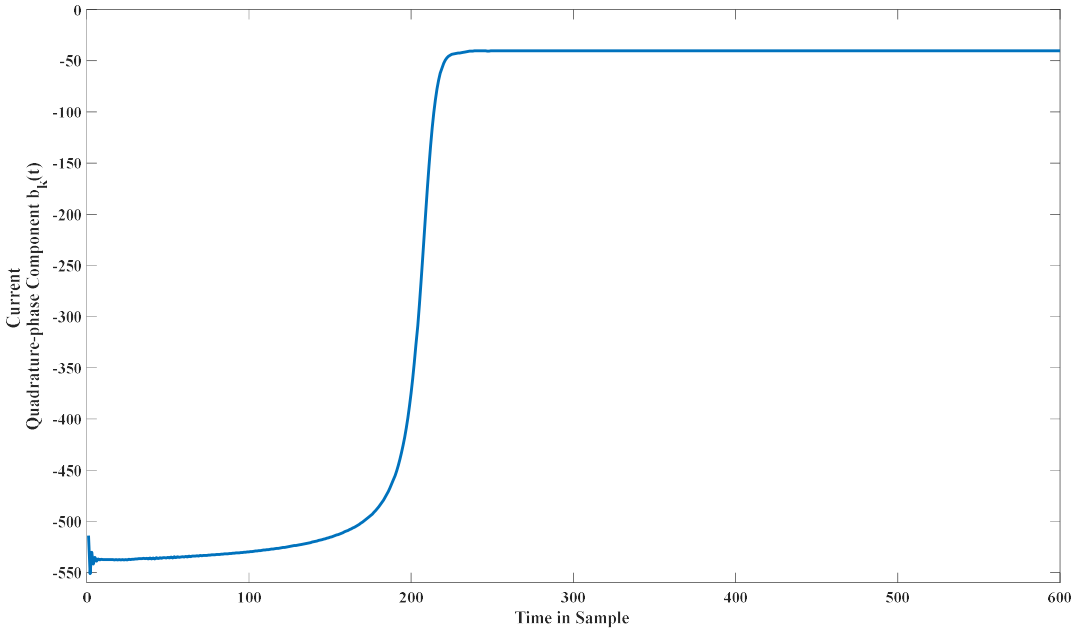

Figure 6.2: Fundamental quadrature-phase component $b_1(t)$ of 100 hp induction motor stator current

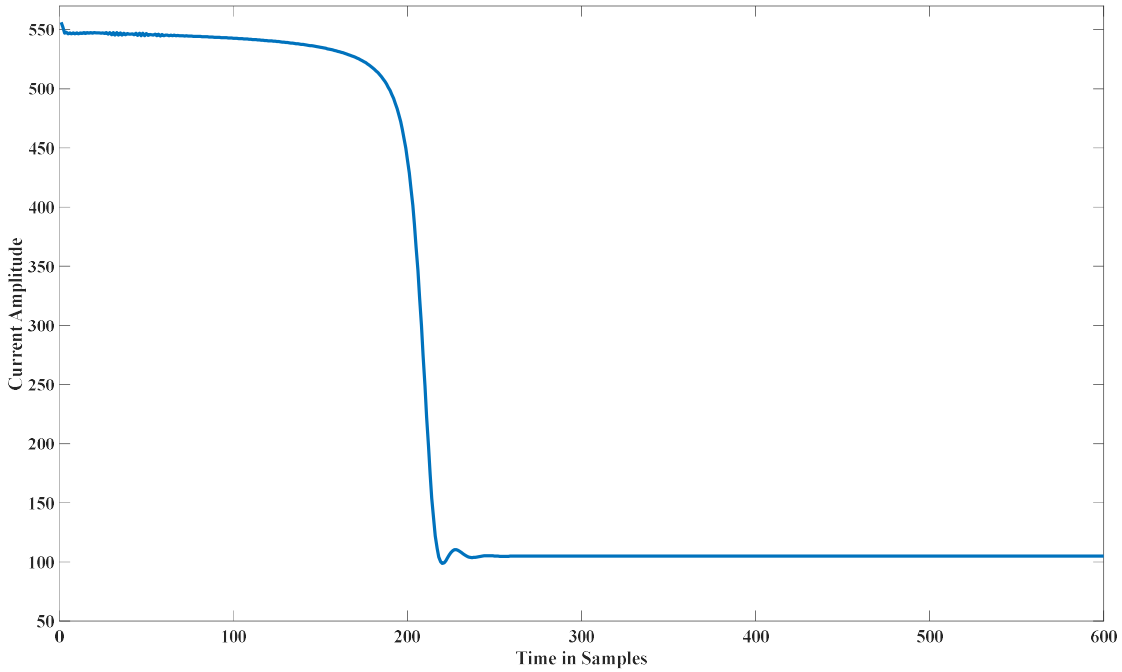

Figure 6.3: 100 hp induction motor stator current envelope.

6.1.2 Estimation of Electrical Parameters

The induction motor equivalent circuit as per IEEE standard 112 is shown in Figure 6.4. Core resistance R_c is very high in most of the induction motors. During the operation, minimal current passes through the core resistance. In the proposed technique, the core resistance R_c is neglected. The equivalent circuit used for the proposed technique is shown in Figure 6.5. The proposed method attempts to estimate the induction motor's mechanical and electrical parameters listed in

Table 6.1.

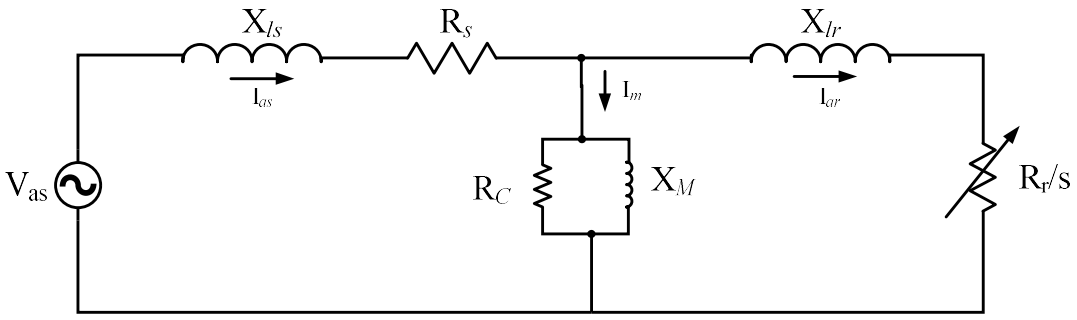

Figure 6.4: Induction Motor Equivalent circuit as per the IEEE standard 112 [61].

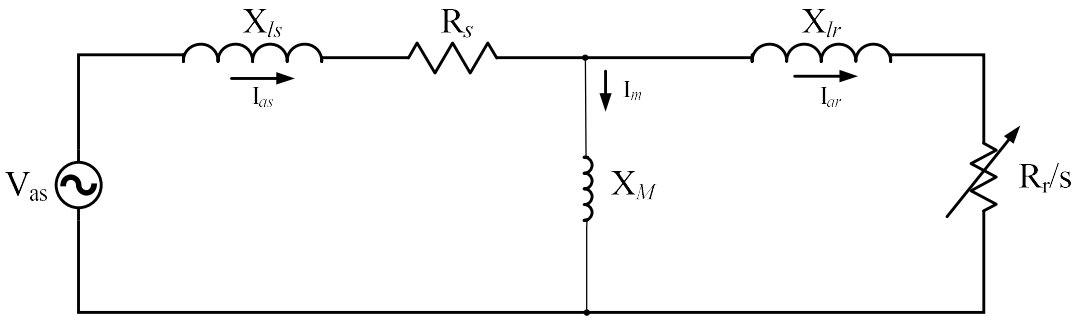

Figure 6.5: Simplified model of induction machine equivalent circuit used for the proposed technique.

Table 6.1: List of induction machine parameters the proposed technique attempts to estimate.

Parameter	Description
X_{ls}	Stator leakage reactance
X_{lr}	Rotor leakage reactance
R_s	Stator resistance
R_r	Rotor resistance
X_M	Magnetizing reactance
J	Moment of Inertia
β	Friction co-efficient of load

During the full-load condition, the induction machine equivalent circuit can be simplified, as shown in Figure 6.5. Current flows through the stator, rotor, and magnetizing branch of the equivalent circuit. The total impedance of the machine can be approximated by equations 6-4 to 6-6. Figure 6.6 shows the change in resistance and reactance of the induction machine as the slip of the machine changes. The shape of these curves remains the same for most of the induction machine only magnitude changes [75].

$$Z = (R_s + jX_{ls}) + jX_M \;||^{ll}\; \left({R_r}/{S} + jX_{lr}\right) \tag{6-4}$$

The real and imaginary part of the impedance can be expressed using the following equations

$$real\{Z\} = \frac{R_s R_r^2 + S^2 R_s (X_M + X_{lr})^2 + S X_M^2 R_r}{R_r^2 + S^2 (X_M + X_{lr})^2} \tag{6-5}$$

and

$$imag\{Z\} = \frac{S^2 X_{ls} (X_M + X_{lr})^2 + S^2 X_{ls} X_M (X_M + X_{ls}) + R_r^2 (X_M + X_{ls})}{R_r^2 + S^2 (X_M + X_{lr})^2} \tag{6-6}$$

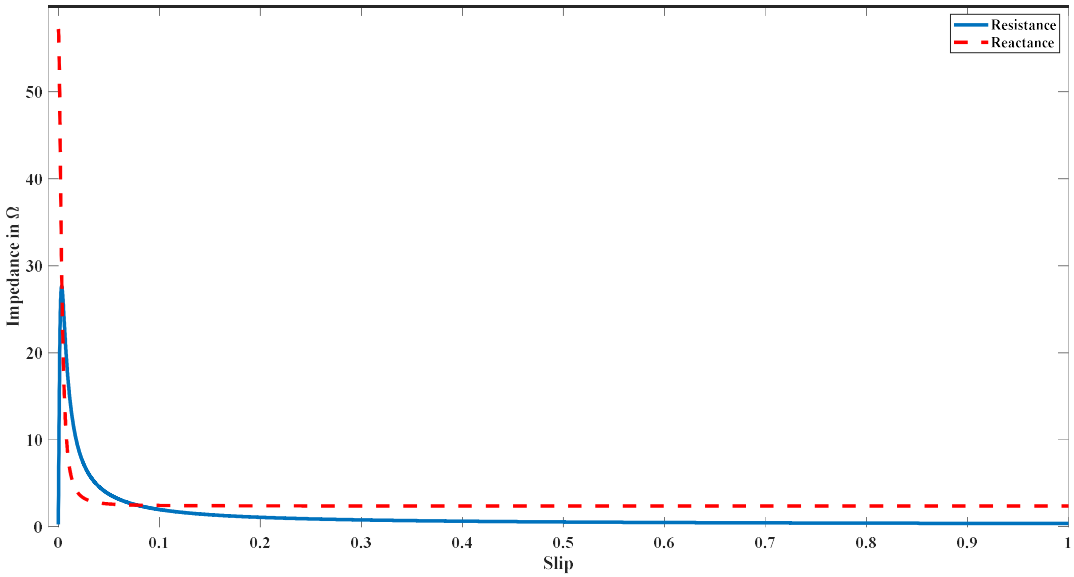

Figure 6.6: Change in resistance and reactance of the induction machine as the slip of the machine changes. Trace with the dashed line is a reactance curve, and trace with the solid line is a resistance curve.

D1: Estimation of Electrical Parameters During the Startup or Transient

At the time when the motor starts from the rest position, the rotating speed of the rotor is low. Thus, slip "s" as defined in equation 6-7 is very high. N_s and N_r are synchronous and rotor mechanical speeds of the motor, respectively. During the startup, as the rotor starts from the rest position, rotor speed N_r is very low; consequently, slip "s" is almost equal to 1. Figure 6.7 shows an example of slip changing overtime for a 100 hp motor. As seen in this figure, the slip varies from one at the startup to close to zero at synchronous speed. At the very beginning of the startup, the slip can be approximated near 100%. This condition at startup emulates the locked rotor condition. During the locked rotor conditions, current in the magnetizing branch is negligible. Consequently, the equivalent circuit of the induction machine can be approximated without a magnetizing branch, as shown in Figure 6.8 [76]. This equivalent circuit provides an opportunity to determine rotor and stator impedances at the beginning of the transient using equations from 6-8 to 6-13.

$$s = \frac{N_s - N_r}{N_s} \qquad 6\text{-}7$$

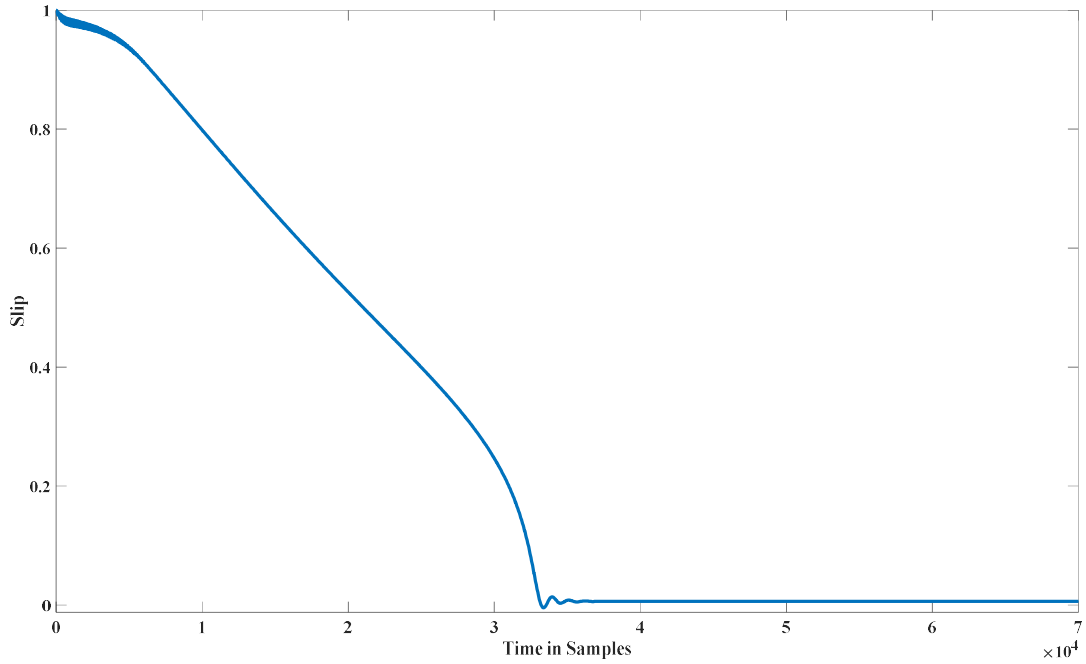

Figure 6.7: An example plot of change in slip overtime for a 100 hp motor.

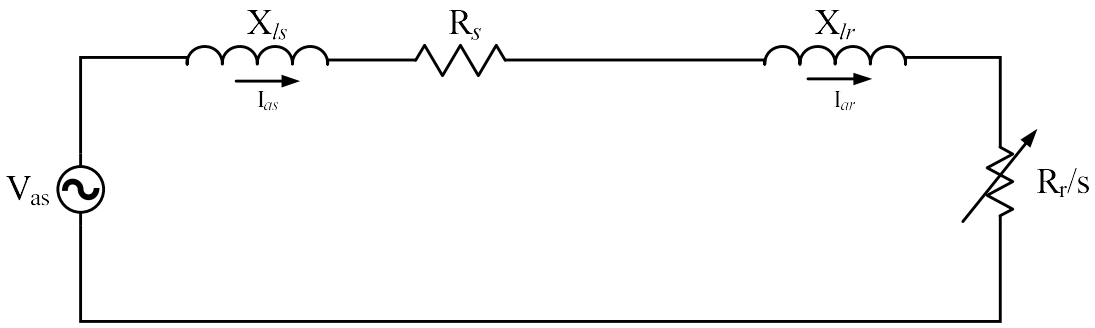

Figure 6.8: Approximate induction motor equivalent circuit at the startup of the motor.

Using bus-level electrical measurement, NILM calculates in-phase stator current component I_p and the quadrature-phase stator current component I_q. The equations for these calculations are as follows:

$$I_p = a_1(t) = \frac{2}{T}\int_0^T i(t-T+s)\cos\left(k\frac{2\pi}{T}(t-T+s)\right) = I\cos\emptyset \qquad 6\text{-}8$$

$$I_q = b_1(t) = \frac{2}{T}\int_0^T i(t-T+s)\sin\left(k\frac{2\pi}{T}(t-T+s)\right) = I\sin\emptyset \qquad 6\text{-}9$$

The power factor angle can be calculated using the values of Ip and Iq as follow:

$$\emptyset = tan^{-1}\left(\frac{I_q}{I_p}\right) \quad 6\text{-}10$$

$$I = \frac{1}{\sqrt{2}}\left(\sqrt{I_p^2 + I_q^2}\right) \quad 6\text{-}11$$

As seen in Figure 6.8, the impedance at the beginning of the transient can be derived as:

$$real\{Z\} = R_s + R_r = \left(\frac{V}{I}\right) cos\,\emptyset \quad 6\text{-}12$$

$$imag\{Z\} = X_{ls} + X_{lr} = \left(\frac{V}{I}\right) \sin\emptyset \quad 6\text{-}13$$

As mentioned in [62], the induction machine characteristic is influenced mainly by leakage reactance of stator and rotor as well as rotor resistance. These values may change with the speed because of eddy currents and saturation of the magnetic path [62]. If the design parameters are not readily available, according to NEMA MG [77] the ratio between the stator and rotor reactance for various NEMA type motors can be approximated as follow :

Type A and D: 1

Type B: 2/3

Type C: 3/7

This relationship can help identify leakage reactances X_{ls} and X_{lr} from equation 6-13. If the value of stator resistance R_s is known, then rotor resistance R_r value can be estimated from equation 6-12. One of the requirements of measuring R_r is to identify the rotor position at the measurement [61]. As suggested in [61], the value of R_r can be averaged over a set of voltage and current measurements. In this estimation technique, the value of (R_s+R_r) is averaged over a small period during the transient. The value of R_s remains relatively constant over the operating range, which helps in estimating the value of R_r during transient conditions.

Transient electrical current and voltage provide the opportunity to estimate R_s, R_r, $X_{lr,}$ and X_{ls}. The next section will discuss the derivation of X_M during steady-state using no-load, almost no-load, and full-load conditions.

D2: Estimation of Electrical Parameter During Steady State

As discussed in the previous section, measurement of electrical supply voltage and stator current of induction motor at the beginning of the transient provides the opportunity to estimate induction motor equivalent circuit electrical parameters R_s, R_r, X_{lr}, and X_{ls}. This section describes the estimation of X_M using full-load, almost no-load, and no-load conditions.

Use of No-load Condition

During the no-load condition, the motor is completely disconnected from the mechanical load. In this condition, there is a negligible current flowing through the rotor circuit of an induction machine [61] and [69]. The equivalent circuit in this condition can be approximated as shown in Figure 6.9. The impedance of this equivalent circuit can be estimated using equations 6-14 to 6-18.

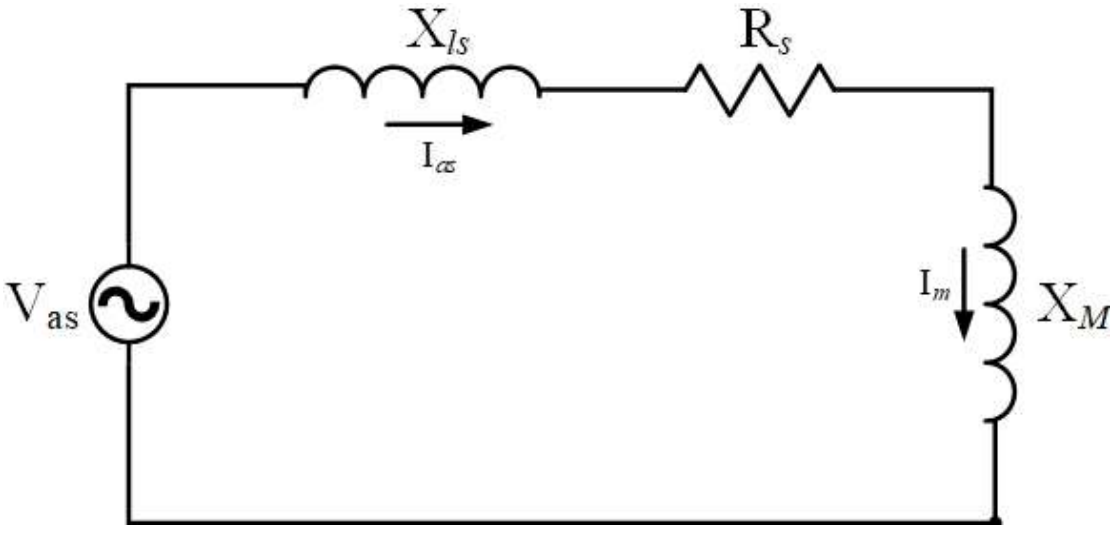

Figure 6.9: Approximated Induction motor circuit at no-load.

The equivalent impedance Z of the circuit shown in Figure 6.9, can be presented using the following equation,

$$Z = R_s + j(X_{ls} + X_M) \qquad 6\text{-}14$$

The power factor angle at steady-state can be calculated using the steady-state in-phase and quadrature-phase component of stator current,

$$\emptyset = tan^{-1}\left(\frac{I_q}{I_p}\right) \quad 6\text{-}15$$

Then the stator resistance can be calculated by the following equation,

$$real\{Z\} = R_s = \left(\frac{V}{I}\right)\cos\emptyset \quad 6\text{-}16$$

Total of stator leakage reactance and magnetizing reactance can be calculated using the following equation,

$$imag\{Z\} = (X_{ls} + X_M) = \left(\frac{V}{I}\right)\sin\emptyset \quad 6\text{-}17$$

Using the estimated value of X_{ls} from the transient measurements, X_M can be calculated with the following equation,

$$X_M = imag\{Z\} - X_{ls} \quad 6\text{-}18$$

In the field, estimating the induction machine parameters using the no-load condition is difficult. It requires a lengthy process of taking the machine out of the operation and re-installing it after the measurements are done. Unless the machine is taken out of the service for other purposes and that opportunity is used to determine the parameters, this could be a time consuming and costly process. The purpose of this research is to propose a technique that can estimate induction machine parameters while the machine is in operation. Consequently, the method of estimating parameters using the full-load and relatively no-load conditions are proposed in the next sections.

Use of Full-load Condition when Stator Resistance R_s is Known

The technique presented here in this section is only applicable if the stator resistance R_s is known. Table 6.2 shows the typical nameplate data available on every motor. In addition to this information, nameplate also has information on the type of NEMA design, insulation class, frame size, and winding connections. Synchronous speed N_s, full-load slip $S_{fl,}$ and full-load torque T_{fl} can be calculated using the nameplate data and equations 6-19 to 6-21.

Table 6.2: Typical nameplate data for an induction machine.

Parameters	Description
P	Rated Power in kW or HP
f_e	Rated electrical frequency in Hz
V	Rated voltage
I_{fl}	Full-load current in Amperes
PF	Full-load power factor
η_{fl}	Full-load efficiency
N_{fl}	Full-load speed in RPM
p	Number of poles
SF	Service Factor

$$N_s = 60\ (Seconds) f_e \left(\frac{2}{p}\right) RPM \tag{6-19}$$

$$S_{fl} = \frac{N_s - N_{fl}}{N_s} \tag{6-20}$$

Full-load motor torque can be calculated by the following equation [52],

$$T_e = T_{fl} = \left(\frac{p}{2}\right)\frac{P\ (in\ watts)}{2\pi f_e(1 - S_{fl})}\ \text{N.m} \tag{6-21}$$

Based on this nameplate data, derived data from nameplate and all of the other electrical parameters estimated as discussed in the previous sections, the value of X_M can be determined using equations 6-22 to 6-25.

The steady-state torque can be expressed in terms of current in phasor form as defined in [52]:

$$T_e = 3\left(\frac{p}{2}\right)\left(\frac{X_M}{\omega_b}\right) Re\left[j\ \vec{I}^*_{as}\vec{I}'_{ar}\right] \tag{6-22}$$

In equation 6-22, current vector $\vec{I}^*_{as}$ is a complex conjugate of the stator current. $\vec{I}'_{ar}$ is the rotor current that can be defined as follow [52],

$$\vec{I}'_{ar} = \frac{j\ (\omega_e/\omega_b)\ X_M}{r_r/s\ +\ j\ (\omega_e/\omega_b)(X_M\ +\ X_{lr})}\vec{I}^*_{as} \tag{6-23}$$

Replacing $\vec{I}'_{ar}$ in equation 6-22 with 6-23,

$$T_e = \frac{3\left(\frac{p}{2}\right)\left(\frac{\omega_e}{\omega_b}\right)\left(\frac{X_M^2}{\omega_b}\right)\left(\frac{r_r}{s}\right)|I_{as}|^2}{\left(\frac{r_r}{s}\right)^2 + \left(\frac{\omega_e}{\omega_b}\right)^2 (X_M + X_{lr})^2} \qquad 6\text{-}24$$

In the above equation 6-24, T_e is full-load torque at the full-load stator current I_{as}. The value of I_{as} at full-load is available from the induction motor nameplate data. Equations 6-22 to 6-24 are based on per unit system where ω_e and ω_b are equal. Only X_M is the unknown quantity in equation 6-24 as T_e can be calculated using equation 6-21, as X_{lr}, and R_r are known.

Rearranging equation 6-24, as shown in equation 6-25, provides an opportunity to estimate X_M. The positive root of the equation below provides the estimated value of X_M.

$$X_M^2\left(T_e - 3I_{as}^2\left(\frac{p}{2}\right)\left(\frac{1}{\omega_e}\right)\left(\frac{r_r}{s_{fl}}\right)\right) + X_M(2T_eX_{lr}) + T_e\left(\left(\frac{r_r}{s_{fl}}\right)^2 + X_{lr}^2\right) = 0 \qquad 6\text{-}25$$

Use of Nearly No-load Condition when Stator Resistance R_s is Unknown

To this point, it is presumed that the value of R_s is known; it helped in estimating the value rotor resistance R_r and magnetizing reactance X_M. In the case where stator resistance value is unknown, it may be challenging to determine all the electrical parameters of the induction machine equivalent circuit. It is also challenging to remove the motor from the operation and run at no-load to estimate the value of stator resistance. However, many large induction motors running critical mechanical loads in the power plant starts at almost no-load, for example, if the pump is the mechanical load connected to the induction motor, the discharge valve might be closed until little after the electrical transient is settled. There will not be any liquid running on the discharge side of the piping system when the discharge valve is closed. Similarly, in the case of the coal crusher's motor, coal is not fed to the crusher until after the motor attains steady-state.

In both of these examples, the motor is connected to the load via shaft. There will be some mechanical load of the shaft and mechanical load's mass on the motor. This condition is referred to as a nearly or almost no-load condition in this thesis. In the case of the nearly no-load state, reactive power drawn by the motor at the steady-state is higher than the active power. It can be

assumed that all the reactive current flows into stator leakage reactance X_{ls} and magnetizing reactance X_M. This assumption can help estimate the value of magnetizing reactance X_M, the value of rotor resistance R_r, and finally, the value of stator resistance R_s from equations 6-26 to 6-30.

During steady-state at relatively no-load condition, magnetizing reactance can be approximated using the following equations,

$$imag\{Z\} = X_M + X_{ls} = \left(\frac{V}{I}\right)\sin\emptyset \tag{6-26}$$

$$X_M = imag\{Z\} - X_{ls} \tag{6-27}$$

The iterative process to estimate rotor resistance R_r can be set up using equations 6-28 to 6-30. As seen in equation 6-28, full-load torque can be calculated using, number of poles p, rated power output P, line frequency f_e and the full-load slip S_{fl} of the motor.

$$T_{fl} = \left(\frac{p}{2}\right)\frac{P\ (in\ watts)}{2\pi f_e(1 - S_{fl})}\ \ \text{N.m} \tag{6-28}$$

Full-load torque can also be estimated using estimated rotor reactance X_{lr}, estimated magnetizing reactance X_M from the relatively no-load state, rated full-load stator current I_{fl}, and the value rotor resistance $R_r \in [0, R_r+R_s]$, as shown in equation 6-29. T_{fl}^e is estimated full-load torque.

$$T_{fl}^e = \frac{3\left(\frac{p}{2}\right)\left(\frac{X_M^2}{\omega_e}\right)\left(\frac{r_r}{s}\right)|I_{fl}|^2}{\left(\frac{r_r}{s}\right)^2 + (X_M + X_{lr})^2} \tag{6-29}$$

Iteratively changing the value of rotor resistance R_r from 0 to R_r+R_s in equation 6-29 to minimize the error of equation 6-30, can help estimate the value of rotor resistance R_r.

$$\text{err} = \min\sqrt{\left(T_{fl}^e - T_{fl}\right)^2} \tag{6-30}$$

Once the value of rotor resistance R_r is estimated, the value of stator resistance R_s can be determined using the value of real impedance at the transient condition derived from equation 6-12. The magnetizing reactance X_M, and rotor resistance R_r estimation can further be improved using the process described in the following section.

Recalibration of X_M and R_r using Measured current

Thus far, X_M is derived using an assumption that the quadrature-phase current at steady-state for a nearly no-load condition is due to stator leakage reactance and magnetizing reactance, as shown in equations 6-26 and 6-27. The value of rotor resistance is estimated using rated torque, rated current, and the estimated value of X_M based on assumption. These values can be calibrated for steady-state conditions using the iterative process. In this step, the error minimization function is used to minimize the error between the estimated current using the calculated values of motor impedance and measured current, as shown in equation 6-33.

The boundary conditions for these parameters established as $X_M^s \in [X_M \pm 0.5\ X_M]$, and $R_r^s \in [R_r \pm 0.5\ R_r]$. Here superscript "s" is used for steady-state values. Combination of parameters from the established boundary for X_M, and R_r in concert with previously estimated parameters R_s, X_{ls}, and X_{lr} are used to estimate the value of total impedance Z, as shown in equation 6-31.

$$Z = R_s + jX_{ls} + \left(\frac{jX_M^s \left(jX_{lr} + \frac{R_r^s}{s_s} \right)}{jX_M^s + jX_{lr} + \frac{R_r^s}{S^s}} \right) \qquad 6\text{-}31$$

In equation 6-31, S^s is a steady-state slip. The steady-state slip can be estimated using the Fast Fourier Transform (FFT) of the measured steady-state stator current. Figure 6.10 shows an example of detecting speed using FFT of measured stator current by NILM. In this example, it is a 10-pole machine running with at nearly no-load. As this is a 10-pole machine, the synchronous speed of the machine is 720 revolution per minute (RPM), which is 12 revolutions per second (RPS) or Hz. As shown in Figure 6.10, the detected speed at the low load is 11.9975 Hz, which is as expected, close to the synchronous speed.

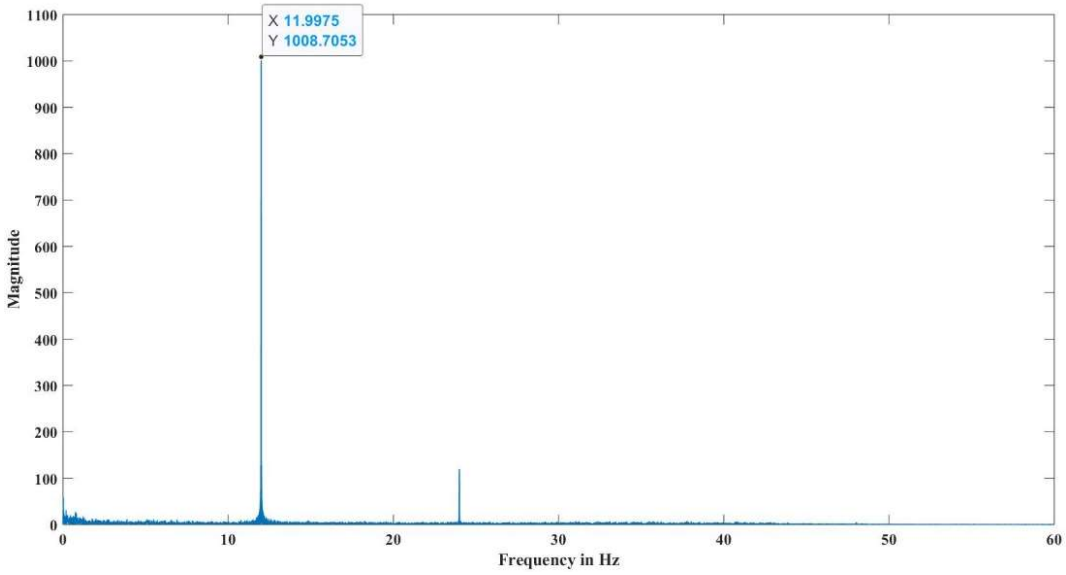

Figure 6.10: Example of 10-pole machine speed detection using FFT.

Using the value of total impedance Z from equation 6-31, one can find the value of estimated stator current I^s_{est} as follow:

$$I^s_{est} = \frac{V}{Z} \tag{6-32}$$

Equation 6-33 shows the error minimization function to minimize the error between estimated current I^s_{est} and measured stator current I^s at steady state. The combination of parameters where the error is minimum is the new set of parameters at the steady-state.

$$err = \min \sqrt{(\text{imag}\{I^s_{est}\} - \text{imag}\{I^s\})^2 + (\text{real}\{I^s_{est}\} - \text{real}\{I^s\})^2} \tag{6-33}$$

This procedure provides refined estimations for magnetizing reactance X_M and values of the rotor resistance R_r^s. These values are used to calculate the friction coefficient of the load, as will be shown later in this chapter.

6.1.3 Estimation of Mechanical Parameters

Once all the electrical parameters are estimated, the next step in the process is to determine mechanical parameters the mass moment of inertia J, and the friction coefficient of load β. Table 6.3 lists all the parameter descriptions associated with mechanical equations from 6-34 to 6-37.

Table 6.3: List of parameters associated with mechanical equations.

Parameter	Description
J	Mass moment of inertia in Nm
ω_r	Electrical angular velocity of the rotor in radian
P	Number of poles
T_e	Motor torque
T_l	Load torque (fan, pump, etc.)
T_a	Acceleration torque
β	Friction constant of load

When a motor starts from the rest position, it accelerates until it attains the steady-state speed. During this acceleration period, the motor draws higher startup current and generates acceleration torque to move mechanical load connected to the motor. The acceleration torque is equal to the difference between torque generated by motor T_e and load torque T_l as shown in 6-34. Equation 6-35 shows the relationship between acceleration torque and rate of change of velocity during the acceleration of the rotor.

$$T_a = T_e - T_l \tag{6-34}$$

$$J\left(\frac{2}{p}\right)\frac{\partial \omega_r}{\partial t} = T_a = T_e - T_l \tag{6-35}$$

Load torque T_l can be approximated for a fan with equation 6-36, and pump with equation 6-37. Examples of torque-speed curves for these types of loads are shown in Figure 6.11 and Figure 6.12.

$$T_l = \beta\omega_r^2 \tag{6-36}$$

$$T_l = \beta\omega_r^3 \tag{6-37}$$

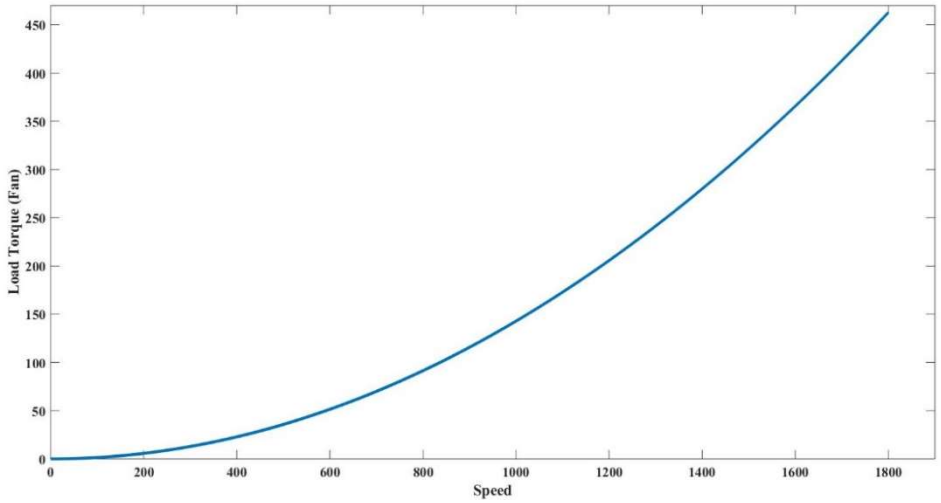

Figure 6.11: Example torque speed curve for the fan type of load.

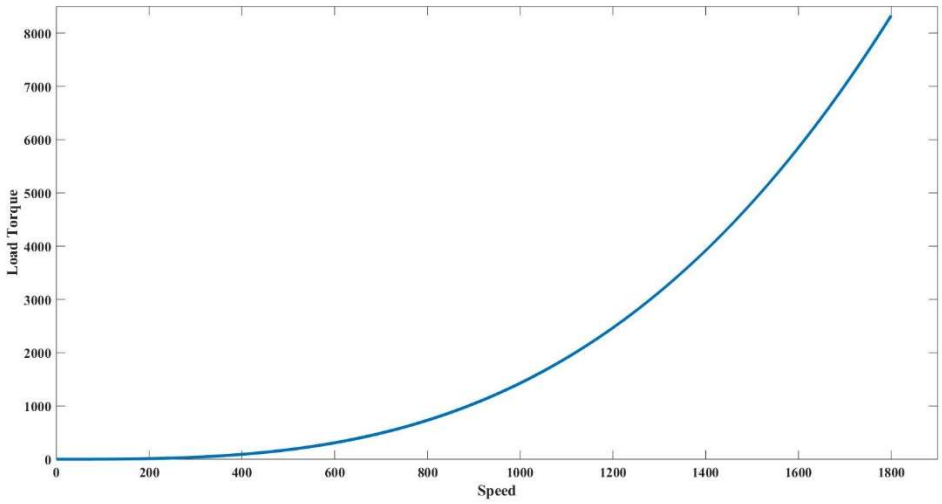

Figure 6.12: Example torque speed curve for a pump type of load.

D1: Estimation of Friction co-efficient of load β

The value of friction co-efficient of load β can be calculated at the steady-state. The β value can be estimated for varying load conditions up to full-load conditions using equations 6-38 to 6-44. The estimated impedance of the motor at a steady state can be calculated using equation 6-38.

$$Z_{est} = R_s + jX_{ls} + \left(\frac{jX_M^s \left(jX_{lr} + \frac{R_r^s}{S^s} \right)}{jX_M^s + jX_{lr} + \frac{R_r^s}{S^s}} \right) \quad 6\text{-}38$$

The value of stator current can be estimated using voltage measurement and estimated impedance value from 6-38, as shown in equation 6-39. The term $\mathrm{I}_{\mathrm{est}}^{\mathrm{s}}$ in that equation is the estimated stator current at steady-state.

$$\mathrm{I}_{\mathrm{est}}^{\mathrm{s}} = \frac{\mathrm{V}}{\mathrm{Z}_{\mathrm{est}}} \tag{6-39}$$

Based on the estimated stator current, the rotor current can be calculated, as shown in equation 6-40, where the term $\mathrm{I}_{r\_est}^{\mathrm{s}}$ is the estimated rotor current at steady-state.

$$\mathrm{I}_{r\_est}^{\mathrm{s}} = \mathrm{I}_{\mathrm{est}}^{\mathrm{s}} \left(\frac{\mathrm{j}X_M^s}{\mathrm{j}X_M^s + \mathrm{j}X_{lr} + \frac{\mathrm{R}_{\mathrm{r}}^{\mathrm{s}}}{\mathrm{s}_{\mathrm{s}}}} \right) \tag{6-40}$$

The torque generated by motor can be calculated using the estimated rotor current and calculated rotor resistance, as shown in equation 6-41, where the term $\mathrm{T}_{e\_est}^{\mathrm{s}}$ is and estimated motor torque at steady-state.

$$\mathrm{T}_{e\_est}^{\mathrm{s}} = 3\left(\frac{\mathrm{p}}{2}\right) \frac{\left|\mathrm{I}_{\mathrm{r_{est}}}^{\mathrm{s}}\right|^2 \left(\frac{\mathrm{R}_{\mathrm{r}}^{\mathrm{s}}}{\mathrm{s}_{\mathrm{s}}}\right)}{2\pi\, \mathrm{f_e}(1 - s_s)} \tag{6-41}$$

At the steady-state, the acceleration torque or inertial torque $\mathrm{T_a}$ is almost zero as the rate of change of velocity $\frac{\partial \omega_r}{\partial\, t}$ is near zero. Consequently, the torque generated by the motor is equal to load torque, as shown in 6-42 and 6-43. The load torque in equation 6-43 refers to the fan type of load.

$$T_a = T_{e\_est}^s - T_l = 0 \tag{6-42}$$

$$T_{e\_est}^s = T_l = \beta\omega_{\mathrm{r}}^2 \tag{6-43}$$

Solving equation 6-43 for β,

$$\beta = \frac{T_{e\_est}^s}{\omega_r^2} \tag{6-44}$$

If the full-load torque or rated power specifications are available, then β value at full-load can be calculated directly from those values. Replacing the value of $T^{s}_{e\_est}$ in equation 6-44 with full-load torque as specified in nameplate data and the value of angular velocity ω_r at full-load.

D2: Estimation of Induction Motor Moment of Inertia J

Load co-efficient β was estimated using the steady-state values of rotor resistance and reactance. Moment of inertia *J* is pronounced at the starting of the motor. Thus the moment of inertia *J* is estimated using the transient or locked rotor values of rotor resistance R_r and X_{lr}. The process to estimate the moment of inertia is as follow:

First, rearranging equation 6-36, as shown in equation 6-45,

$$J = \left(\frac{p}{2}\right)\frac{T_e - T_l}{\left(\frac{\partial \omega_r}{\partial t}\right)} \qquad 6\text{-}45$$

As seen in equation 6-45, *J* is proportional to the difference between the motor and load torque; and inversely proportional to the rate of change of speed. All these values are dependent on speed. Figure 6.13 shows an example rate of change of speed curve for a 500 hp induction motor. As seen in this figure, during the transient time, speed increases, and then it settles at near synchronous speed to attain steady-state.

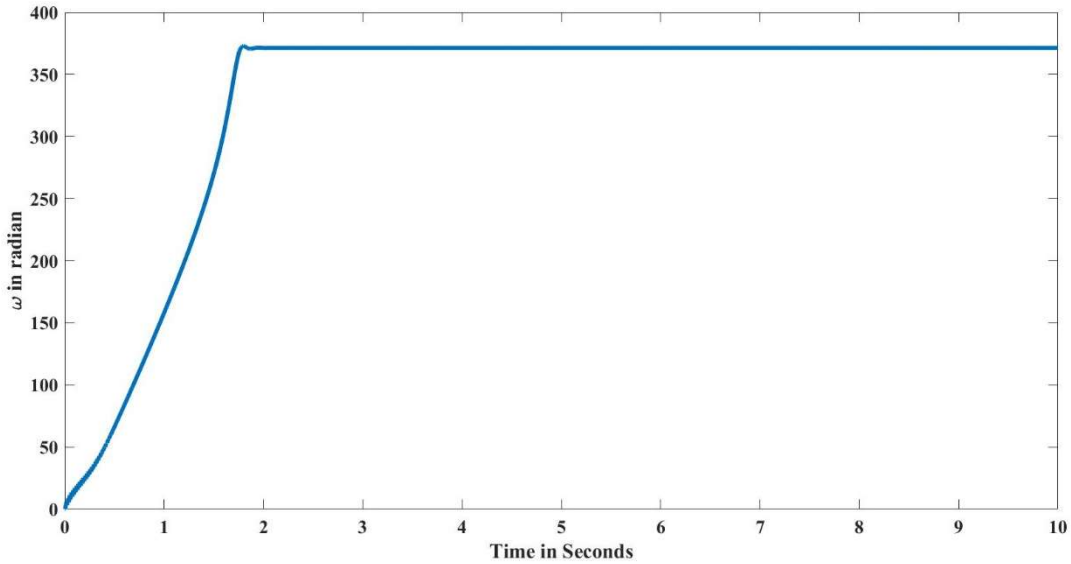

Figure 6.13: Example rate of change of speed curve for 500 hp induction motor running fan type of load.

Figure 6.14 shows the start and end time of the inrush current for 600 hp coal crusher induction motor. Detecting transient time duration from the current measurement can provide an average change of speed per second. For example, if the motor starts from rest t=0 and motor reaches to steady-state speed ω_{r1} at t=t_1 then ω_r^a is the average rate of change of speed. The value of ω_r^a is an estimate of the rotor angular velocity at one second, as shown in 6-46.

$$\frac{\partial \omega_r}{\partial t} = \frac{\omega_{r1} - 0}{t_1 - 0} = \frac{\omega_{r1}}{t_1} = \omega_r^a \ rad/sec \qquad 6\text{-}46$$

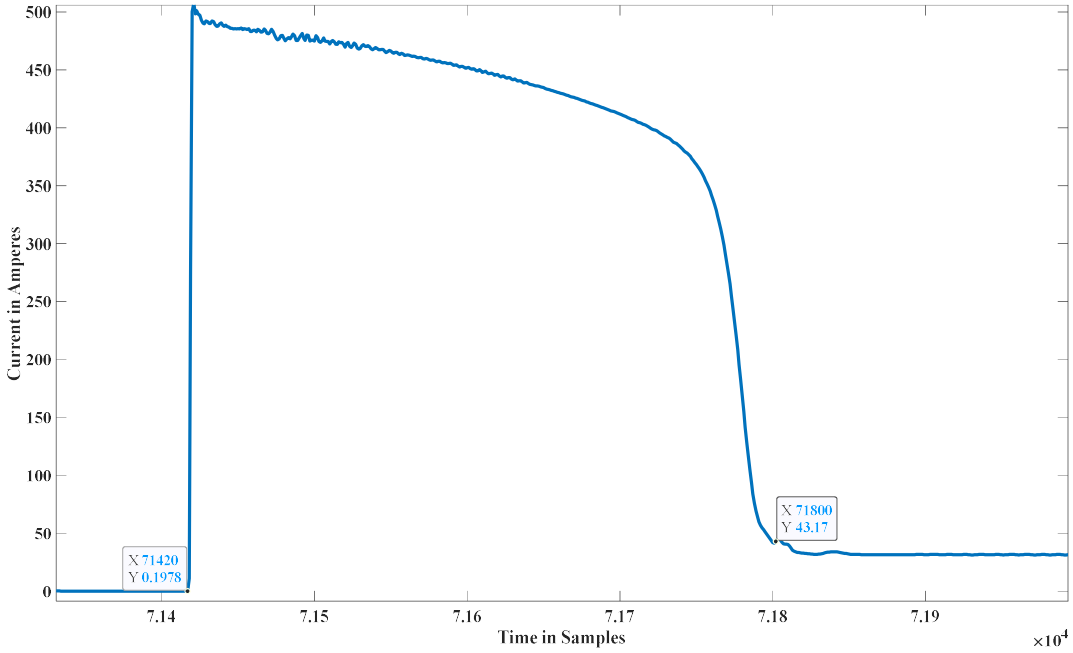

Figure 6.14: 600 hp coal crusher motor transient, showing start-time and end-time of the transient.

Load torque for a fan type load at one second after motor starts can be calculated as,

$$T_l^a = \beta \omega_r^{a\,2} \qquad 6\text{-}47$$

Slip at the average rate of change of speed s^a, can be calculated using equation 6-48 where ω_e is the synchronous electrical angular velocity of the induction motor.

$$s^a = \frac{\omega_e - \omega_r^a}{\omega_e} \qquad 6\text{-}48$$

Estimated motor torque T_e at one second after the motor start can be calculated using equation 6-49. Equation 6-49 is essentially the same as equation 6-29, except the values of current

and slip. Please note that values of rotor resistance and leakage reactance are the values estimated during the transient condition. The value of magnetizing reactance X_M^s is a calibrated value obtained using equation 6-33.

$$T_e^a = \frac{3\left(\frac{p}{2}\right)\left(\frac{{X_M^s}^2}{\omega_e}\right)\left(\frac{R_r}{s^a}\right)|I_{as}|^2}{\left(\frac{R_r}{s^a}\right)^2 + (X_M^s + X_{lr})^2} \quad 6\text{-}49$$

Value of *J* can be estimated using 6-45 and 6-50,

$$J = \left(\frac{p}{2}\right)\frac{T_e^a - T_l^a}{\omega_r^a} \quad 6\text{-}50$$

The assumption in estimating the value of *J* in this manner is; the rate of change of velocity remains the same throughout the transient. Estimating *J* in this manner may have some inherent discrepancies, as the rate of change of velocity of the rotor is generally not constant during the transient period. The value of *J* can be estimated this way and adjusted using the transient time duration of the stator current, as will be shown in the results section of this thesis.

6.2 Testing and Results of the Proposed Estimation Technique

The proposed technique has been tested using simulations and laboratory tests. The results of these tests are described in this section. Simulations performed for two motors; a100 hp and 500 hp motor. A laboratory test was also performed on a 0.5 hp motor.

6.2.1 Simulation Test and Results

There were two simulation tests performed in this thesis. In both tests value of the stator resistance R_s was known, and simulation was performed at full-load. The following section describes the simulations and results.

D1: 500 HP, 2300V, and 4-pole Induction Motor

Table 6.4 provides a list of specifications used for the induction motor simulation. These specifications are obtained from [52] and [78]. Fifth order dynamic simulation model for induction motor was used to simulate motor operation using these parameters. Equation 3-1 to 3-6 provides

the basis for the dynamic simulation model of an induction machine. Detailed information regarding the induction motor's dynamic simulation model can be found in [52] and [79].

Table 6.4: List of 500 hp induction motor parameters from [52] and [78]

Parameters	Value
Type of the motor	A or D
Voltage (V)	2300 V
Full-load Current (I_{fl})	93.6 A
Full-load Speed (N_s)	1773 RPM
Number of Poles	4
Stator Resistance (R_s)	0.262 Ω
Rotor Resistance (R_r)	0.187 Ω
Stator Reactance (X_{ls})	1.206 Ω
Rotor Reactance (X_{lr})	1.206 Ω
Magnetizing Reactance (X_M)	56.02 Ω
Moment of Inertia (J)	11.06 kg-m^2
Torque Generated by Motor (T_e)	2009 N-m

Stator current obtained from the simulation was processed using the NILM algorithm. NILM provided the spectral co-efficient of stator current's in-phase and quadrature-phase components. This spectral co-efficient of the current envelopes are used to estimate the parameters of the induction motor. In this simulation exercise, the motor started at full-load. Consequently, stator resistance was kept as a known parameter for the simulations. The proposed technique is applicable where stator resistance is known, or when the motor starts with almost no-load.

Equations 6-7 to 6-13 are used to estimate impedance values at the startup of the motor. The value of the power factor can be calculated using the stator current's in-phase and quadrature-phase component. The real and imaginary impedances are determined using the computed value of the power factor. At the startup, the real part of the impedance is the total stator and rotor resistance (R_s+R_r). The imaginary part of the impedance is the total stator and rotor leakage reactance (X_{ls}+X_{lr}). Stator resistance is known in this case, which helps in estimating rotor resistance. As this motor is either type A or D, the stator and rotor leakage reactances are equal.

The magnetizing reactance of the induction machine was estimated using equations 6-19 to 6-25. Induction machine simulation equations 3-1 to 3-6 assume linear magnetic material and

core resistance R_c is also neglected. All the electrical parameters are estimated from transient conditions are used as final estimations.

Using equations 6-41 to 6-43 friction co-efficient of load β was estimated. For the simulations, the motor was started with the full-load. Thus, β was calculated using the full-load conditions, including full-load torque, full-load current, and full-load slip values available from the nameplate data. The value of *J* is calculated using equations 6-45 to 6-50.

The estimations are listed in Table 6.5. Almost all the estimated parameters are close to the actual values, except the value of the moment of inertia *J*. It is to be expected, due to the assumption that the rate of change of velocity is constant the entire duration of acceleration. However, that assumption allows the estimation of *J* relatively close to the actual value. This difference in the value of *J* will affect the duration of the transient time; thus, the value of the moment of inertia *J* can be adjusted iteratively to match the transient time duration of the current envelope. The adjusted value of *J* is also shown in the same table with red fonts below initially estimated value. The adjusted value of *J* is significantly close to the actual value.

Table 6.5: Comparison between estimated parameters and actual values.

Parameters	Actual Value	Estimated Value	% Difference
Rotor Resistance (R_r)	0.187 Ω	0.1879 Ω	0.481283
Stator Reactance (X_{ls})	1.206 Ω	1.1933 Ω	-1.053
Rotor Reactance (X_{lr})	1.206 Ω	1.1933 Ω	-1.053
Magnetizing Reactance (X_M)	56.02 Ω	56.5372 Ω	0.9232
Moment of Inertia (*J*)	11.06 kg-m^2	11.9886 kg-m^2 11.35 kg-m^2	8.396 2.622
Friction co-efficient of load (β)	0.0145	0.0146	0.689

Figure 6.15 shows the comparison between the estimated current in a red dashed trace and the actual stator current with a solid blue trace for the 500 HP motor. The top image of this figure shows the difference in transient time duration due to the imperfect estimation of inertial value *J*. The bottom traces show the same comparison with the adjusted value of *J*. As shown in the bottom trace of Figure 6.15, both estimated and actual current trace matches very well. Figure 6.16 to Figure 6.18 shows a similar comparison for in-phase stator current component, quadrature-phase

stator current component, and rotor mechanical frequency, respectively. As seen in these figures, the adjusted estimation of *J* provides a better match between actual and estimated quantities.

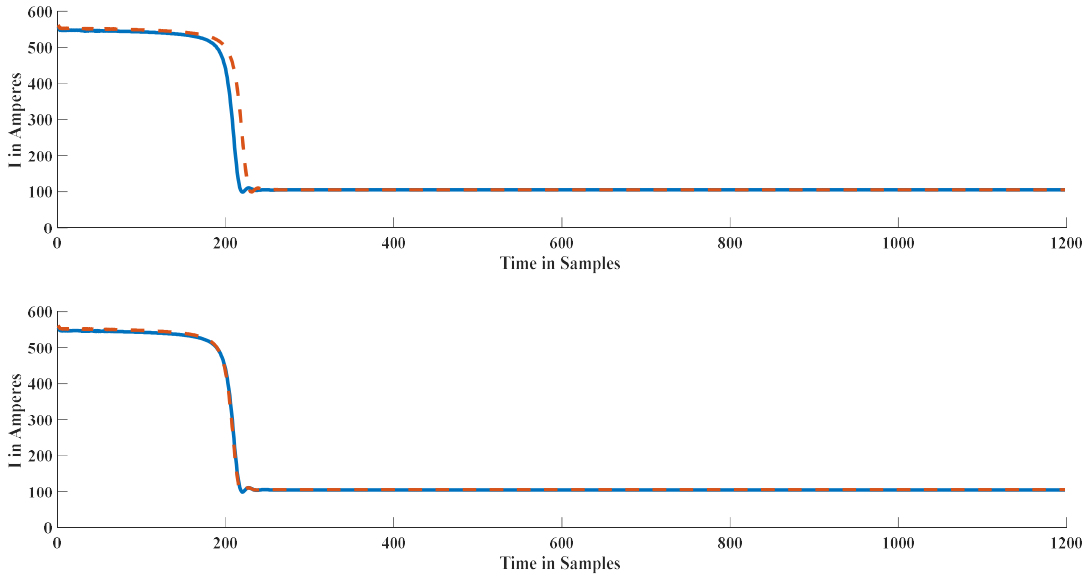

Figure 6.15: Comparison between 500 hp motor's actual stator current in a solid blue trace and estimated stator current with dashed red trace. The top picture shows the comparison between actual current and estimated current with initially estimated value of *J*. The bottom image shows the same comparison with the adjusted value of *J*.

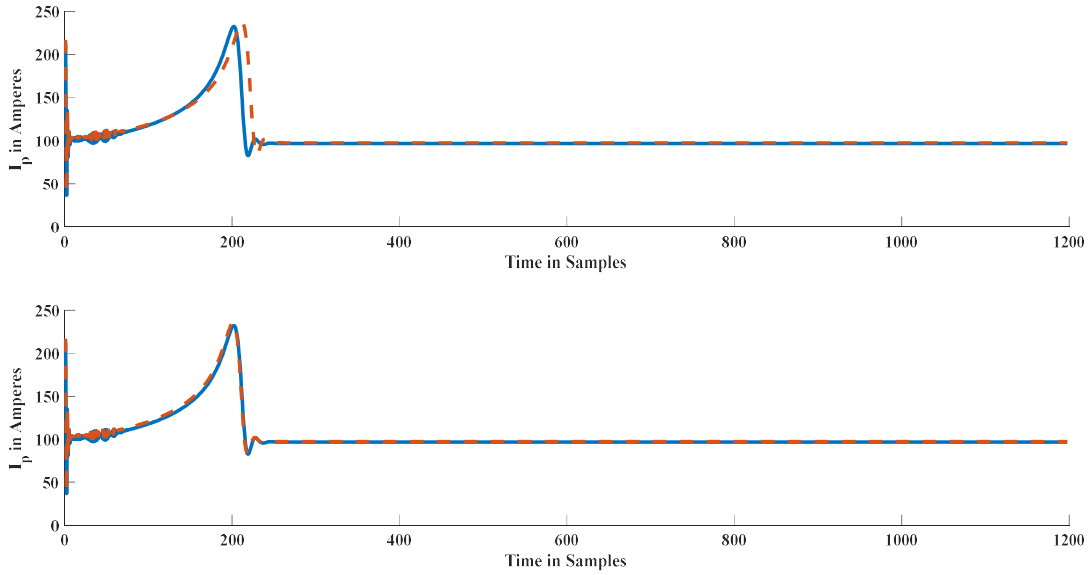

Figure 6.16: Comparison between 500 hp motor's actual in-phase current in a solid blue trace and estimated in-phase current in a dashed red trace. The top picture shows the comparison between actual in-phase current and estimated in-phase current with initially estimated value of *J*. Bottom picture shows the same comparison with the adjusted value of *J*.

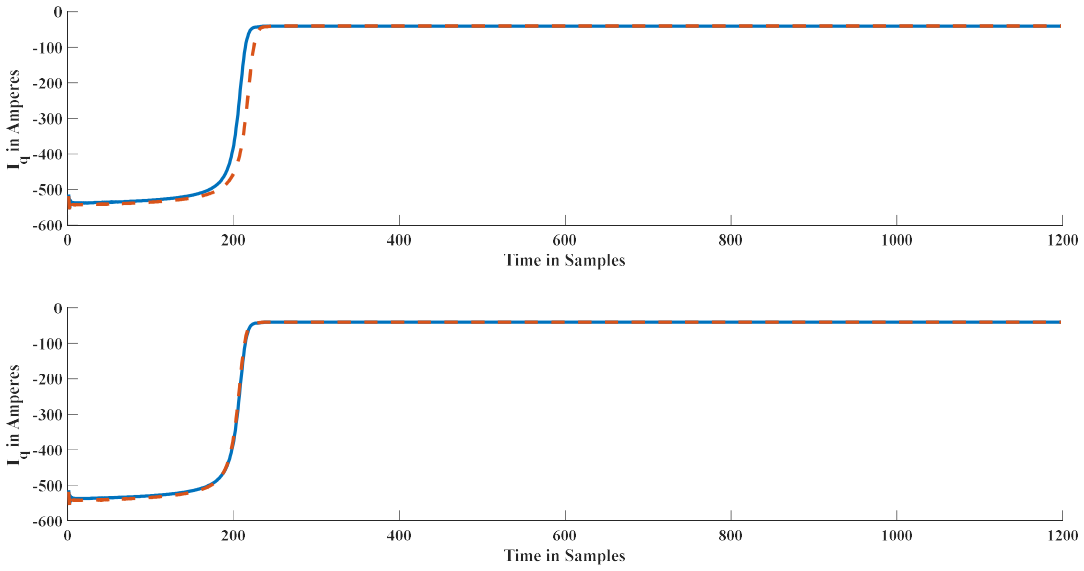

Figure 6.17: Comparison between 500 hp motor's actual quadrature-phase current in a solid blue trace and estimated quadrature-phase current in a dashed red trace. The top picture shows the comparison between actual quadrature-phase current and estimated quadrature-phase current with initially estimated value of *J*. Bottom picture shows the same comparison with the adjusted value of *J*.

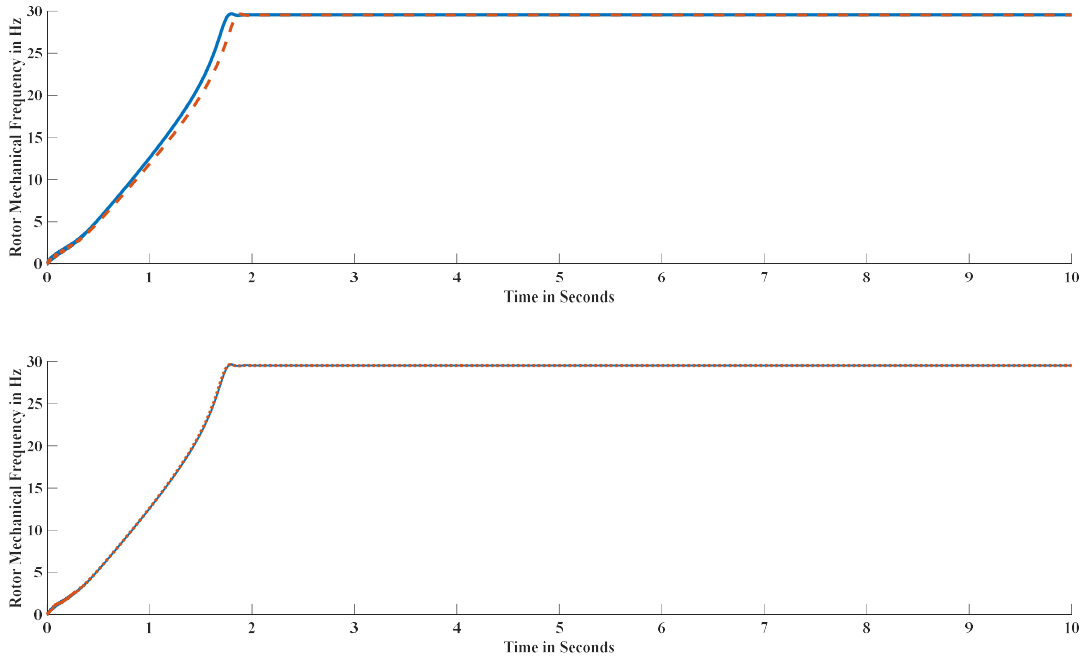

Figure 6.18: Comparison between 500 hp motor's actual rotor speed in Hz with a solid blue trace and estimated rotor speed in Hz with dashed red trace. The top picture shows the comparison between actual rotor speed in Hz and estimated rotor speed in Hz with the initial estimated value of *J*. Bottom picture shows the same comparison with the adjusted value of *J*.

D2: 100 HP, 480V, and 4-pole Induction Motor

Table 6.6 provides a list of 100 HP induction machine parameters used for the simulation. Fifth order dynamic simulation model for induction motor was used to simulate motor operation using parameters listed in Table 6.6. Full-load speed and full-load current were obtained using the simulation.

Table 6.6: List of 100 hp induction motor parameters.

Parameters	Rating
Type of the motor	A or D
Voltage (V)	480 V
Number of Poles	4
Stator Resistance (R_s)	0.024 Ω
Rotor Resistance (R_r)	0.017 Ω
Stator Reactance (X_{ls})	0.227 Ω
Rotor Reactance (X_{lr})	0.227 Ω
Magnetizing Reactance (X_M)	5.83 Ω
Moment of Inertia (J)	2.5 kg-m^2

The electrical and mechanical parameters of the motor were estimated following a similar process as described in 500 hp motor simulations. Table 6.7 shows the comparison between estimated parameters and actual value. The estimated parameters are reasonably close to the actual parameters. Figure 6.19 to Figure 6.23 shows the comparison between actual stator current, in-phase stator current component, quadrature-phase stator current component, rotor frequency, and torque with a solid blue trace and estimated signals with dashed red trace. As shown in these figures, after modifying the value of the moment of inertia *J*, traces are very close to each other as expected.

Table 6.7: Comparison between estimated parameters and actual values.

Parameters	Actual Value	Estimated Value	% Difference
Rotor Resistance (R_r)	0.017 Ω	0.0168 Ω	-1.176470588
Stator Reactance (X_{ls})	0.227 Ω	0.2227 Ω	-1.894273128
Rotor Reactance (X_{lr})	0.227 Ω	0.2227 Ω	-1.894273128
Magnetizing Reactance (X_M)	5.83 Ω	6.0482 Ω	3.74271012
Moment of Inertia (*J*)	2.5 kg-m^2	2.48 kg-m^2 2.6 kg-m^2	-0.8 4
Friction co-efficient of load (β)	0.0028	0.0028	0

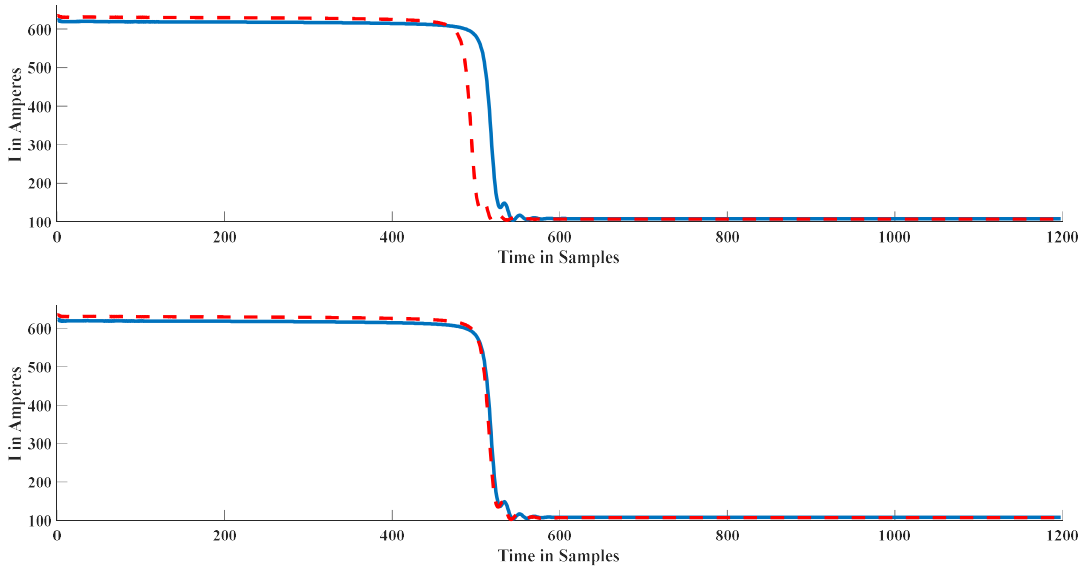

Figure 6.19: Comparison between 100 hp motor's actual stator current in a solid blue trace and estimated stator current in a dashed red trace. The top picture shows the comparison between actual current and estimated current with initially estimated value of *J*. The bottom image shows the same comparison with the adjusted value of *J*.

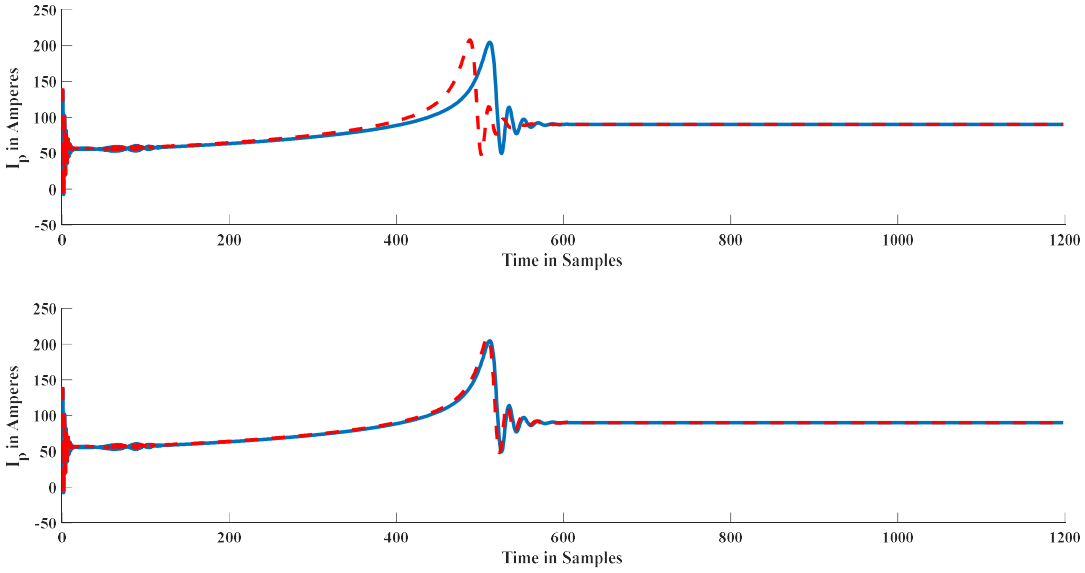

Figure 6.20: Comparison between 100 hp motor's actual in-phase current in a solid blue trace and estimated in-phase current in a dashed red trace. The top picture shows the comparison between actual in-phase current and estimated in-phase current with initially estimated value of *J*. Bottom picture shows the same comparison with the adjusted value of *J*.

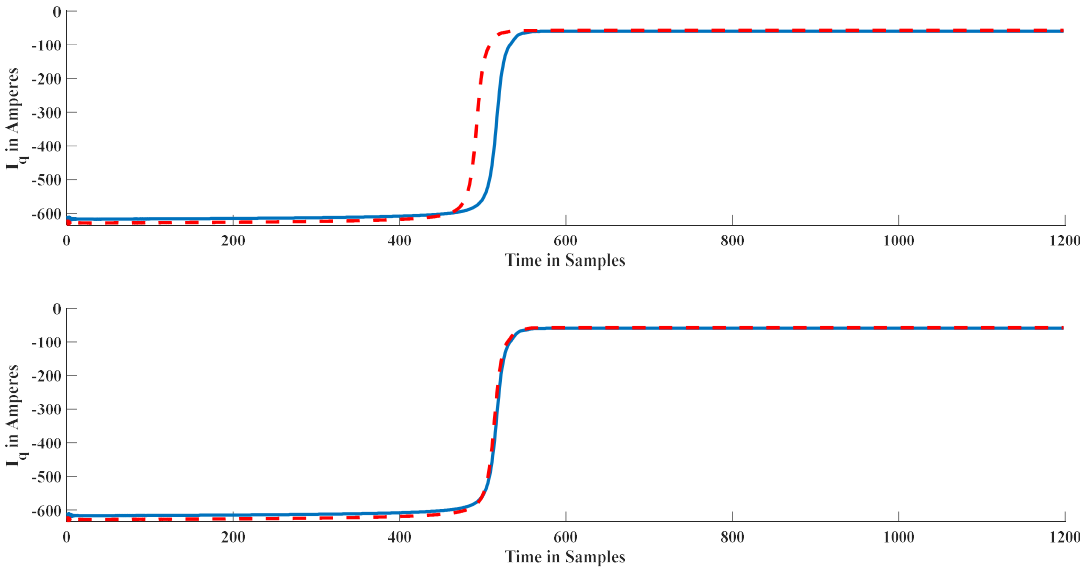

Figure 6.21: Comparison between 100 hp motor's actual quadrature-phase current in a solid blue trace and estimated quadrature-phase current in a dashed red trace. The top picture shows the comparison between actual quadrature-phase current and estimated quadrature-phase current with initially estimated value of *J*. Bottom picture shows the same comparison with the adjusted value of *J*.

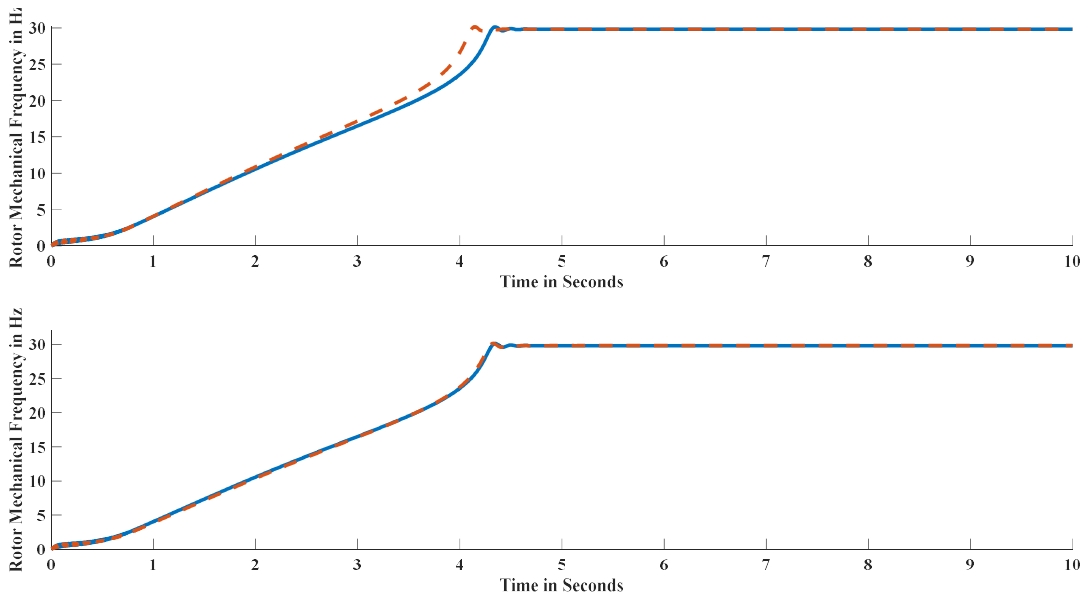

Figure 6.22: Comparison between 100 hp motor's actual rotor speed in Hz in a solid blue trace and estimated rotor speed in Hz in a dashed red trace. The top picture shows the comparison between actual rotor speed in Hz and estimated rotor speed in Hz with an initial estimated value of *J*. Bottom picture shows the same comparison with the adjusted value of *J*.

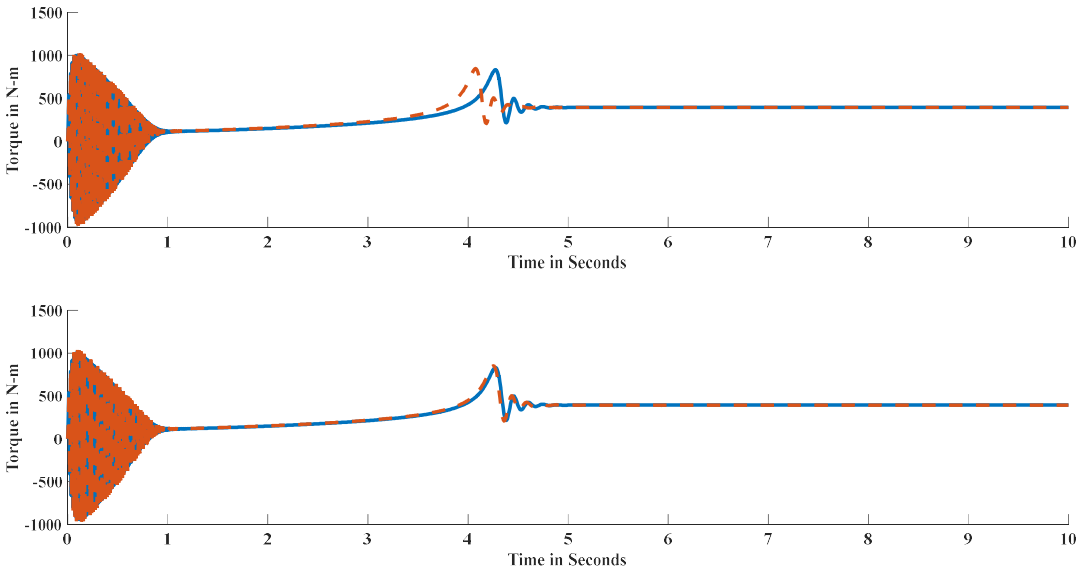

Figure 6.23: Comparison between 100 hp motor's actual rotor torque in N-m in a solid blue trace and estimated rotor torque in N-m in a dashed red trace. The top picture shows the comparison between actual rotor torque in N-m and estimated rotor torque in N-m current with initially estimated value of *J*. Bottom picture shows the same comparison with the adjusted value of *J*.

6.2.2 Laboratory Test and Results

The laboratory test was performed using a 0.5 hp motor connected directly to the utility supply. In this case stator resistance, R_s was kept unknown. Thus, the motor was started with almost no-load. The specifications for the motor are listed in Table 6.8. Figure 6.24 shows the picture of the nameplate data for the motor used in the laboratory test.

Table 6.8: List of motor parameters used for the laboratory test.

Parameter	Rating
NEMA Motor Design Type	B
Voltage	460 V
Output power	0.5 HP
Full-load current	1.1 A
Full-load speed	3450 RPM

Figure 6.24: Picture of nameplate data for the motor used in the laboratory test.

For the laboratory test, the motor was started at nearly no-load and the stator resistance of the induction motor was kept unknown. Similar to simulation test calculations, total stator and rotor impedance were calculated at the beginning of the transient using equations 6-7 to 6-13. The motor used for this test was the NEMA design type "B" motor. The value of stator to rotor leakage reactance ratio $\frac{X_{ls}}{X_{lr}} = 0.67$ was used to determine X_{ls} and X_{lr}, as suggested in [61]. The in-phase component of the current was used to estimate total resistance ($R_r + R_s$) at the transient.

At the steady-state, the measured quadrature-phase current component was higher than the in-phase component of the stator current, as the motor was started with almost no-load. Equation 6-26 and 6-27 were used to estimate the initial value of magnetizing reactance X_M.

The full-load torque can be computed using the rated power of the motor, rated frequency, and full-load slip, as shown in equation 6-51,

$$T_{fl} = \left(\frac{p}{2}\right)\frac{P\ (in\ watts)}{2\pi f_e(1 - S_{fl})} \quad \text{N.m} \qquad 6\text{-}51$$

The full-load torque can be estimated using estimated values of rotor reactance X_{lr}, magnetizing reactance X_M, full-load current $I_{fl,}$ and iterative values of rotor resistance $R_r \in [0, (R_r$

+ R_s)], as seen in equation 6-24. The slip of the motor was obtained using the Fast Fourier Transform (FFT) of the measured current signal.

$$T_{fl}^{e} = \frac{3\left(\frac{p}{2}\right)\left(\frac{X_M^2}{\omega_e}\right)\left(\frac{r_r}{s}\right)|I_{fl}|^2}{\left(\frac{r_r}{s}\right)^2 + (X_M + X_{lr})^2} \quad 6\text{-}52$$

Error minimization function was set up to reduce the error between full-load torque T_{fl} based on rated power and estimated full-load torque T_{fl}^{e}. Rotor resistance was obtained at the minimum value of error close to zero.

$$\text{err} = \min\sqrt{\left(T_{fl}^{e} - T_{fl}\right)^2} \quad 6\text{-}53$$

The refined value of magnetizing reactance X_M and rotor resistance R_r were obtained using the technique outlined in "Recalibration of X_M and R_r using Measured Current" section of this chapter. During the calibration process value of R_r did not change significantly. The recalibrated value of X_M was modified according to calibration, as shown in red fonts in Table 6.9.

Mechanical parameters are estimated using equations outlined in section 6.1.3. Please note that the total transient time duration for this motor was around a one-half second. Equations are modified accordingly to estimate the moment of inertia *J*. Initial estimate of J was 0.0052 kg-m^2 which was iteratively calibrated to 0.00467 to match the transient time duration of one-half second. The motor started with almost no-load; consequently, the value of load friction constant was nearly zero. Table 6.9 shows the list of estimated parameters for the laboratory motor.

Table 6.9: List of estimated parameters for the laboratory motor.

Parameters	Estimated Value
Stator Resistance (R_s)	19.5417 Ω
Stator Reactance (X_{ls})	8.8638 Ω
Rotor Reactance (X_{lr})	13.2956 Ω
Magnetizing Reactance (X_M)	310 Ω 336.5 Ω
Moment of Inertia (*J*)	0.0052 kg-m^2 0.00467 kg-m^2
Friction co-efficient of load (β)	3.4521*10^{-6}

The results of the experiment are shown in Figure 6.25 to Figure 6.27. In this experiment, estimated parameters of the laboratory motor are used with motor simulation equations to generate in-phase and quadrature-phase components of the stator current. As shown in these figures, the red dashed trace is of simulated stator current, the in-phase component, and the quadrature-phase component. The solid blue trace is of similar quantities measured using current and voltage sensors in the laboratory.

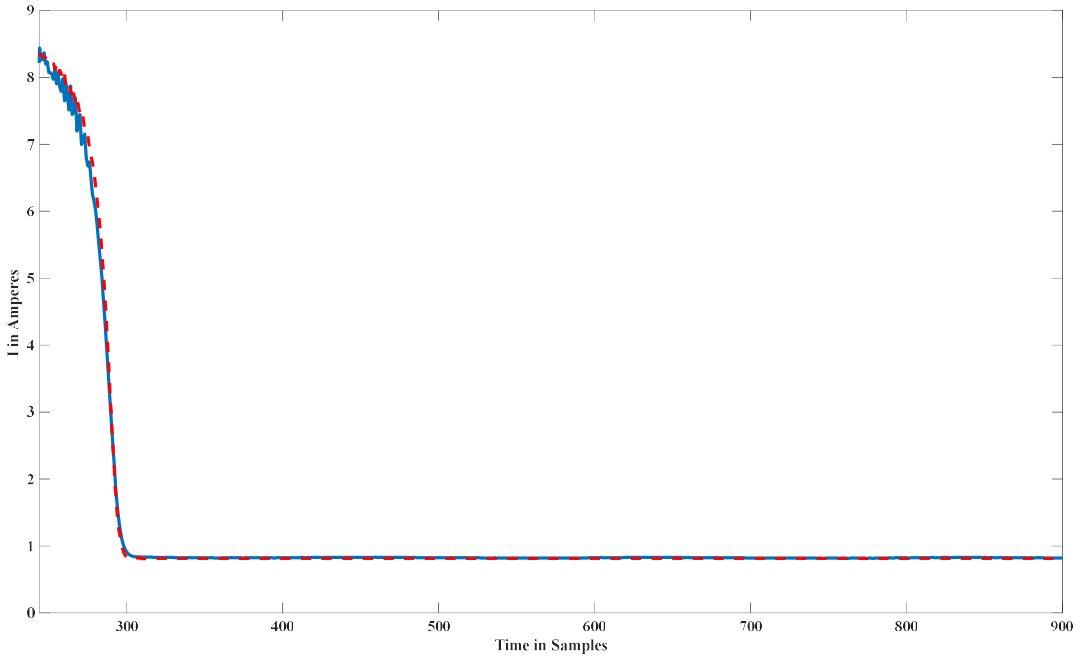

Figure 6.25: Comparison between measured and simulated stator current using estimated parameters for laboratory motor. The solid blue trace is an actual measurement of stator current, and the dashed red trace is simulated stator current.

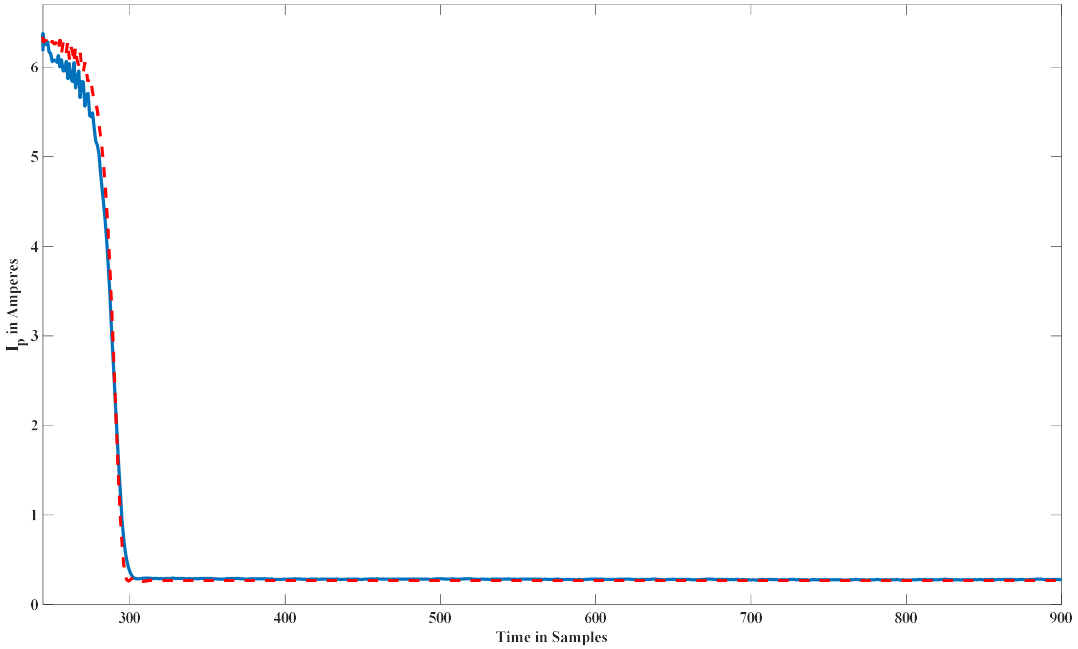

Figure 6.26: Comparison between an actual and simulated in-phase component of stator current using estimated parameters for laboratory motor. The solid blue trace is an actual measurement of the in-phase stator current, and the dashed red trace is simulated in-phase stator current.

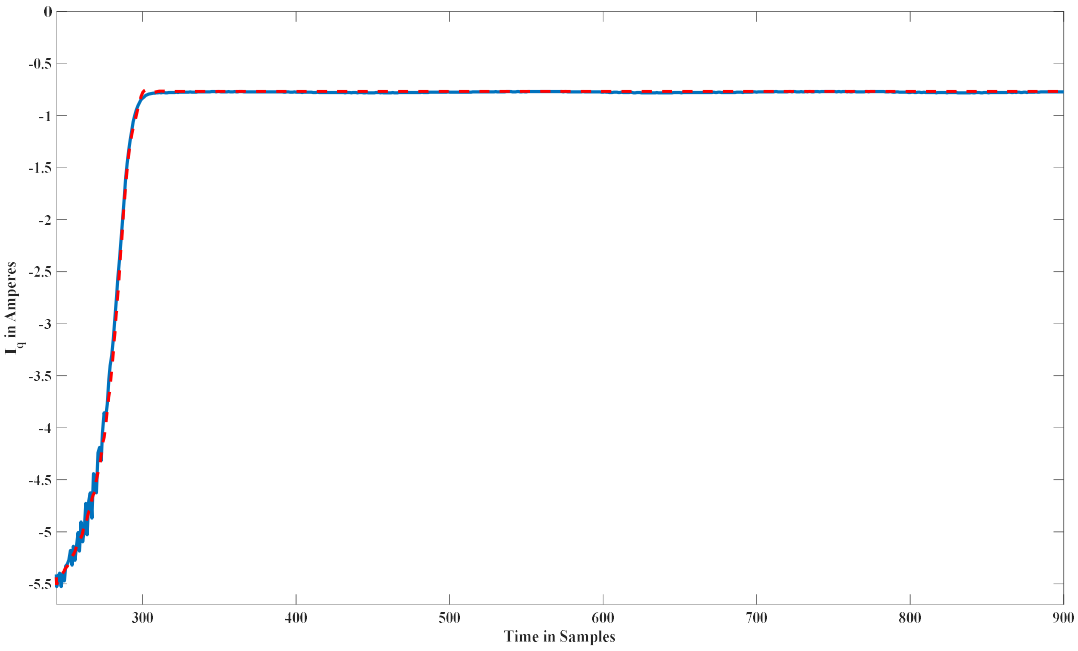

Figure 6.27: Comparison between an actual and simulated quadrature-phase component of stator current using estimated parameters for laboratory motor. The solid blue trace is the actual measurement of quadrature-phase stator current, and the dashed red trace is simulated quadrature-phase stator current

6.3 Summary

This chapter of the thesis proposed a parameter estimation technique for induction motor using bus-level current data. The summary level steps for the estimation of electrical parameters are shown in Figure 6.28. The method was tested using simulated data and laboratory data. As shown in Figure 6.15 to Figure 6.23, the simulated test results show that the technique works accurately. Similar to simulated data, the laboratory testing on a 0.5 hp motor also confirmed the proposed method could estimate parameters of the induction motor with sufficient accuracy. Figure 6.25 to Figure 6.27 shows the results of the laboratory test.

Table 5.2 and Table 5.3 shows the various manufacturer data required by widely used methods to estimate induction machine parameters. Compare to those requirements; the proposed technique requires only motor NEMA design type, measurements of current and voltage, stator resistance if available, and if stator resistance is not available, then it requires that motor starts with almost no-load. This method provides a better opportunity for power plant personnel to determine induction machine parameters without searching for various manufacturer data needed by other methods currently in use.

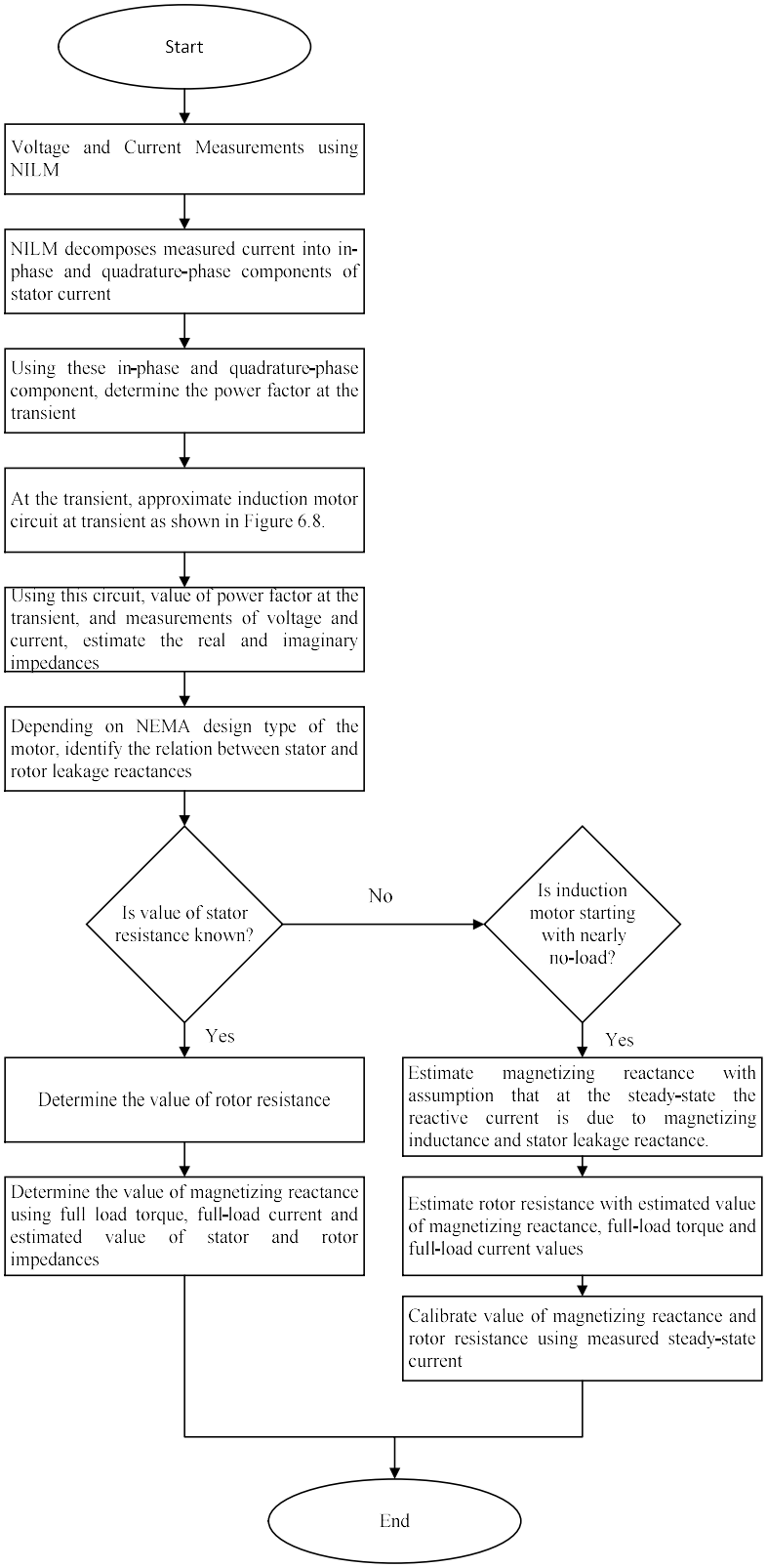

Figure 6.28: Summary level steps to estimate the electrical parameters of the induction machine using the proposed technique.

CHAPTER 7: SUMMARY AND FUTURE WORK

7.1 Summary

Power plant owners and operators are leveraging advancements in sensor technology and data science to deploy monitoring systems that can potentially improve reliability, increase flexibility, and reduce maintenance costs. In many cases, however, plants either do not have the budget for such technologies, or the return on investment is deemed to be too low. This thesis takes an alternative view and considers a potentially low-cost approach that can be implemented simply by monitoring the aggregate current flowing into a bank of downstream motors.

The approach described in this thesis relies on current and voltage sensors installed at either the main bus or a motor control center in a power plant. This non-intrusive technique can be used to provide some level of information about the health of motors and their driven equipment. Previous work has demonstrated the ability to use such measurements to track the operation of various loads; this thesis looks to move beyond the tracking application to develop specific use cases in power plants.

This thesis considered two specific applications of bus-level current for sensing applications in power plants. First, this dissertation shows two use cases on the use of bus-level electrical signals for induction motor health monitoring. Second, the thesis shows how bus-level measurements can be used to estimate induction-motor electrical and mechanical parameters. These parameter estimates can be provided to planners and system operators to support various regulatory requirements, including startup after the loss of off-site power at nuclear units and startup of black start units after the blackout.

7.2 Future Work

This type of technique has very high potential as a cost-effective sensory technology for monitoring and diagnostics of induction machines and connected mechanical load. It is particularly helpful for traditional power generations, for example, nuclear power plants and fossil power plants. As mentioned in chapter 1 of this dissertation, EPRI's PMBD has a repository of failure modes associated with induction motor used in power plants. The future work in the area of diagnostics of the induction machine using bus-level electrical measurement should include further expansion of the proposed technique to detect other failure modes in that database. In particular, detecting critical faults of the induction machines of the plant can have a significant impact on safety, reliability, and maintenance savings for the power plant industry.

This dissertation also proposed a technique to estimate induction machine parameters using bus-level electrical measurements. Parameter estimation for some of the induction machines is required to fulfill regulatory requirements as well as power system stability assessment within the power plant. The widely used parameter estimation technique for the induction machine in power plant requires a significant amount of manufacturer data. In comparison, the proposed technique requires a minimum amount of manufacturer data, and most of the required data is available on the nameplate of the induction machine.

There are some limitations to the proposed technique, and it needs further investigation. The proposed method only works if the value of stator resistance is known or the motor starts at almost no-load. The future work in the area of estimating parameters using bus-level electrical measurement can include:

1. There may be some induction machine loads in the power plant, which start with the full-load on the shaft; for example, a fan. Further investigation of the proposed technique is needed to determine parameters when the stator resistance is unknown, and the motor starts with varying or full-load. This investigation will help in

developing a comprehensive technique to determine induction machine parameters using bus-level electrical measurements.

2. The proposed technique has neglected the core resistance from the induction machine equivalent circuit. The effect of including core resistance for the parameter estimation technique should be investigated.
3. The effects of saturation and eddy currents on the stator and rotor parameters have not been considered in the proposed technique. The eddy currents and saturation of leakage path have an influence on parameter estimation during startup and steady-state. Future work may include exploring the effects of saturation on the proposed parameter estimation technique. The proposed method may need modifications to accommodate the effects of eddy currents and saturation.
4. Further testing of this technique using the power plant's induction motors' data may also help improve this technique for power plant applications.
5. Exploring the use of this technique to model the motor control center (MCC) as well as determine protection relay settings.

REFERENCES

[1] "Value-Based Maintenance." NEI.org. https://www.nei.org/CorporateSite/media/filefolder/resources/delivering-nuclear-promise/2017/eb-17-03a-value-based-maintenance.pdf (accessed August 29, 2019).

[2] J. Downey. "Layoffs Possible as Duke Energy expands buyout offers." https://www.bizjournals.com/charlotte/news/2018/11/27/layoffs-possible-as-duke-energy-expands-buyout.html (accessed August 29, 2019).

[3] "Continuous Online Monitoring (COLM) Guidebook: Volumes 1-8," EPRI, Palo Alto, CA: 2018. 3002014436.

[4] "Continuous Online Monitoring (COLM): Vertical Motor, Medium Voltage <15kV – Vertical – Solid Shaft – Tilt Pad – Oil Lubed," EPRI, Palo Alto, CA: 2018. 3002012765.

[5] "Continuous On-Line Monitoring (COLM): Horizontal Motors, Medium Voltage <15kV – Horizontal – Filters – Sleeve Bearing – Oil Lubed," EPRI, Palo Alto, CA: 2018. 3002012766.

[6] "Continuous Online Monitoring (COLM): Positive Displacement Pump," EPRI, Palo Alto, CA: 2018, 3002012773.

[7] "Continuous On-Line Monitoring (COLM): Horizontal Pumps, Horizontal – Single Stage – Double Suction," EPRI, Palo Alto, CA: 2018. 3002013864.

[8] "Continuous Online Monitoring (COLM): Horizontal Motor, Medium Voltage <15kV – Horizontal – TEFC – Sleeve Bearing – Oil Lubed," EPRI, Palo Alto, CA: 2018. 3002012771.

[9] "Continuous Online Monitoring (COLM): Horizontal Pumps, Horizontal – Single Stage – Single Suction," EPRI, Palo Alto, CA: 2018. 3002012769.

[10] "Continuous On-Line Monitoring (COLM): Vertical Pump, Vertical – Deep Draft – Radial Flow – Product Lube," EPRI, Palo Alto, CA: 2018. 3002012763.

[11] "Preventive Maintenance Basis Database (PMBD) 4.0." https://pmbd.epri.com/Landing.aspx (accessed August 29, 2019).

[12] *3002012770, Continuous Online Monitoring (COLM): Horizontal Motor, Medium Voltage <15kV – Horizontal – TEFC – Rolling Element – Grease Lubed*.

[13] "Electric Motor Predictive and Preventive Maintenance Guide," EPRI, Palo Alto, CA: 1992. NP-7502.

[14] "Predictive Maintenance Technologies: An Overview of Motor Current Signature Analysis and Electromagnetic Signature Analysis," EPRI, Palo Alto, CA: 2015. 3002003913.

[15] W. T. Thomson and M. Fenger, "Current signature analysis to detect induction motor faults," *IEEE Industry Applications Magazine,* vol. 7, no. 4, pp. 26-34, 2001, doi: 10.1109/2943.930988.

[16] V. F. Pires, T. G. Amaral, and J. F. Martins, "Stator winding fault diagnosis in induction motors using the dq current trajectory mass center," in *2009 35th Annual Conference of IEEE Industrial Electronics*, 3-5 Nov. 2009 2009, pp. 1322-1326, doi: 10.1109/IECON.2009.5414714.

[17] "Program on Technology Innovation: Smart Component Demonstration Project," EPRI, Palo Alto, CA: 2008. 1016702.

[18] S. Nandi, H. A. Toliyat, and X. Li, "Condition Monitoring and Fault Diagnosis of Electrical Motors—A Review," *IEEE Transactions on Energy Conversion,* vol. 20, no. 4, pp. 719-729, 2005, doi: 10.1109/TEC.2005.847955.

[19] M. E. H. Benbouzid, "A review of induction motors signature analysis as a medium for faults detection," in *IECON '98. Proceedings of the 24th Annual Conference of the IEEE Industrial Electronics Society (Cat. No.98CH36200)*, 31 Aug.-4 Sept. 1998 1998, vol. 4, pp. 1950-1955 vol.4, doi: 10.1109/IECON.1998.724016.

[20] M. E. H. Benbouzid and G. B. Kliman, "What stator current processing-based technique to use for induction motor rotor faults diagnosis?," *IEEE Transactions on Energy Conversion,* vol. 18, no. 2, pp. 238-244, 2003, doi: 10.1109/TEC.2003.811741.

[21] G. B. Kliman and J. Stein, "Methods of Motor Current Signature Analysis," *Electric Machines & Power Systems,* vol. 20, no. 5, pp. 463-474, 1992/09/01 1992, doi: 10.1080/07313569208909609.

[22] R. R. Schoen, T. G. Habetler, F. Kamran, and R. G. Bartheld, "Motor bearing damage detection using stator current monitoring," in *Proceedings of 1994 IEEE Industry Applications Society Annual Meeting*, 2-6 Oct. 1994 1994, vol. 1, pp. 110-116 vol.1, doi: 10.1109/IAS.1994.345491.

[23] R. R. Schoen and T. G. Habetler, "Effects of time-varying loads on rotor fault detection in induction machines," in *Conference Record of the 1993 IEEE Industry Applications Conference Twenty-Eighth IAS Annual Meeting*, 2-8 Oct. 1993 1993, pp. 324-330 vol.1, doi: 10.1109/IAS.1993.298943.

[24] "Demonstration of Smart Monitoring and Diagnostic Technologies for Electrical Equipment: Electromagnetic Signature Analysis and Motor Current Signature Analysis," EPRI, EPRI, Palo Alto, CA: 2017. 3002011674.

[25] "NRC INSPECTION MANUAL - INSPECTION PROCEDURE 88070." https://www.nrc.gov/docs/ML0617/ML061780363.pdf (accessed September 5, 2019).

[26] NRC. "NRC INSPECTION MANUAL - INSPECTION PROCEDURE 71111 ATTACHMENT 18." NRC. https://www.nrc.gov/docs/ML1630/ML16306A185.pdf (accessed September 5, 2019).

[27] T. r. w. p. b. t. s. o. t. F. E. R. C. i. c. w. s. f. t. N. A. E. R. C. a. i. R. Entities., "Report on the NERC-FERC-Regional Entity Joint Review of Restoration and Recovery Plans," NERC. [Online]. Available: https://www.ferc.gov/legal/staff-reports/2018/bsr-report.pdf

[28] J. R. Gracia, P. W. O'Connor, L. C. Markel, D. Rui Shan, T. Rizy, and A. Tarditi, "Hydropower Plants as Black Start Resources," in "HydroWIRES," ORNL, 2019.

Accessed: 8/29/2019. [Online]. Available: https://www.energy.gov/sites/prod/files/2019/05/f62/Hydro-Black-Start_May2019.pdf

[29] NERC. "Standard EOP-005-2 — System Restoration from Blackstart Resources " https://www.nerc.com/pa/Stand/Reliability%20Standards/EOP-005-2.pdf (accessed August 29, 2019).

[30] NERC. "EOP-005-3 – System Restoration from Blackstart Resources " NERC. https://www.nerc.com/pa/Stand/Reliability%20Standards/EOP-005-3.pdf (accessed August 29, 2019).

[31] PJM. "RTO-Wide Five-Year Selection Process, Request for Proposal for Black Start Service " https://www.pjm.com/-/media/markets-ops/ancillary/black-start-service/pjm-2018-rto-wide-black-start-rfp.ashx?la=en (accessed August 29, 2019).

[32] *Modelling and simulation of black start and restoration of electric power systems.*, Electra ELT_147_1, CIGRE, 1993.

[33] PJM. "Black Start Definitions & Procurement Process." PJM State & Member Training Dept. https://www.pjm.com/~/media/training/nerc-certifications/gen-exam-materials/gof/20160104-black-start-definitions-procurement-process.ashx (accessed August 29, 2019).

[34] S. B. Leeb, S. R. Shaw, and J. L. Kirtley, "Transient event detection in spectral envelope estimates for nonintrusive load monitoring," *IEEE Transactions on Power Delivery,* vol. 10, no. 3, pp. 1200-1210, 1995, doi: 10.1109/61.400897.

[35] S. R. Shaw and C. R. Laughman, "A Kalman-Filter Spectral Envelope Preprocessor," *IEEE Transactions on Instrumentation and Measurement,* vol. 56, no. 5, pp. 2010-2017, 2007, doi: 10.1109/TIM.2007.904475.

[36] R. W. C. IV, "Minimally Intrusive Strategies for Fault Detection and Energy Monitoring," PhD, Electrical Engineering and Computer Science, Massachusetts Institute of Technology, 2007.

[37] S. R. Sanders, J. M. Noworolski, X. Z. Liu, and G. C. Verghese, "Generalized averaging method for power conversion circuits," in *21st Annual IEEE Conference on Power Electronics Specialists*, 1990 1990, pp. 333-340, doi: 10.1109/PESC.1990.131207.

[38] A. W. A. Oppenheim, and I. Young, *Signals and Systems*. Englewood Cliffs, NJ: Addison-Wellesley, 1988.

[39] S. Shaw, "System Identification and Modeling for Non-Intrusive Load Diagnostics," Ph.D dissertation, Massachusetts Institute of Technology, Cambridge, MA, 2000.

[40] S. R. Shaw, C. B. Abler, R. F. Lepard, D. Luo, a. S. B. Leeb, and L. K. Norford, "Instrumentation for high performance nonintrusive electric load monitoring," *ASME Journal of Solar Energy Engineering,* vol. 120, pp. 224-229, August 1998.

[41] C. Laughman *et al.*, "Power signature analysis," *IEEE Power and Energy Magazine,* vol. 1, no. 2, pp. 56-63, 2003, doi: 10.1109/MPAE.2003.1192027.

[42] S. Drenker and A. Kader, "Nonintrusive monitoring of electric loads," *IEEE Computer Applications in Power,* vol. 12, no. 4, pp. 47-51, 1999, doi: 10.1109/67.795138.

[43] S. R. Shaw, S. B. Leeb, L. K. Norford, and R. W. Cox, "Nonintrusive Load Monitoring and Diagnostics in Power Systems," *IEEE Transactions on Instrumentation and Measurement,* vol. 57, no. 7, pp. 1445-1454, 2008, doi: 10.1109/TIM.2008.917179.

[44] K. D. Lee, "Electric load information system based on non-intrusive power monitoring," Ph.D. dissertation, Mechanical Engineering, Massachusetts Institute of Technology, May 2003.

[45] W. Wichakool, A. Avestruz, R. W. Cox, and S. B. Leeb, "Resolving Power Consumption of Variable Power Electronic Loads Using Nonintrusive Monitoring," in *2007 IEEE Power Electronics Specialists Conference*, 17-21 June 2007 2007, pp. 2765-2771, doi: 10.1109/PESC.2007.4342456.

[46] T. DeNucci *et al.*, "Diagnostic indicators for shipboard systems using non-intrusive load monitoring," in *IEEE Electric Ship Technologies Symposium, 2005.*, 27-27 July 2005 2005, pp. 413-420, doi: 10.1109/ESTS.2005.1524708.

[47] R. Cox, Lt. James P. Mosman USN, LCdr. Duncan McKay USN, Dr. Steven B. Leeb, and C. T. J. M. USN, "Diagnostic indicators for shipboard cycling systems using non-intrusive load monitoring," in *ASNE Day*, Arlington, VA, 2006.

[48] G. R. Mitchelle, R. W. Cox, J. Paris, and S. B. Leeb, "Shipboard Fluid System Diagnostic Indicators Using Non-Intrusive Load Monitoring," *Naval Engineers Journal,* vol. 119, pp. 109-119, 2007/10/01, doi: 10.1111/j.0028-1425.2007.00023.x.

[49] J. M. Anderson, R. W. Cox, P. K. Parikh, and C. R. Laughman, "Improving the efficiency of residential HVAC systems using computer-based power-electronic controls," in *2008 11th Workshop on Control and Modeling for Power Electronics*, 17-20 Aug. 2008 2008, pp. 1-6, doi: 10.1109/COMPEL.2008.4634692.

[50] P. R. Armstrong, C. R. Laughman, S. B. Leeb, and L. K. Norford, "Fault detection based on motor start transients and shaft harmonics measured at the RTU electrical service," in *International Refrigeration and Air Conditioning Conference at Purdue*, July 12-15, 2004.

[51] P. K. Parikh, R. W. Cox, R. L. Sawyer, A. Shrestha, and J. M. Anderson, "Diagnostics and prognostics for multiple induction machines using a single set of current transducers," in *2009 IEEE International Electric Machines and Drives Conference*, 3-6 May 2009 2009, pp. 1153-1160, doi: 10.1109/IEMDC.2009.5075349.

[52] P. C. Krause, O. Wasynczuk, and S. D. Sudhoff, *Analysis of Electric Machinery and Drives Systems*. New York: Wiley, 2002.

[53] P. Vas, *Parameter Estimation, Condition Monitoring and Diagnosis of Electrical Machines*. Oxford: Clarendon Press 1993.

[54] J. R. Stack, T. G. Habetler, and R. G. Harley, "Effects of machine speed on the development and detection of rolling element bearing faults," *IEEE Power Electronics Letters,* vol. 1, no. 1, pp. 19-21, 2003, doi: 10.1109/LPEL.2003.814607.

[55] R. Isermann, *Fault diagnosis systems*. Berlin: Springer-Verlag, 2006.

[56] A. Wolfram, D. Fussel, T. Brune, and R. Isermann, "Component based multi-model approach for fault detection and diagnosis of a centrifugal pump.," in *American Control Conference (ACC)*, Arlington, VA, 2001.

[57] K. C., V. Cocquempot, and R. Izadi-Zamanabdi, "Model based fault detection in a centrifugal pump application," presented at the IEEE Transactions on Control Systems Technology, 2006.

[58] L. Bachus and A. Custodio, *Know and Understand Centrifugal Pumps*. Elsevier Advanced Technology, 2003.

[59] M. Volk, *Pump characteristics and applications*. Boca Raton, Fl: CRC Press, 2005.

[60] G. Mitchell, R., "Shipboard Fluid System Diagnostics using Non-Intrusive Load Monitoring," Naval Engineer and Master of Science in Ocean Systems Management, Massachusett institute of technology, 2007. [Online]. Available: https://calhoun.nps.edu/handle/10945/2997

[61] "IEEE Standard Test Procedure for Polyphase Induction Motors and Generators," *IEEE Std 112-2004 (Revision of IEEE Std 112-1996),* pp. 1-83, 2004, doi: 10.1109/IEEESTD.2004.95394.

[62] G. J. Rogers and D. Shirmohammadi, "Induction Machine Modelling for Electromagnetic Transient Program," *IEEE Transactions on Energy Conversion,* vol. EC-2, no. 4, pp. 622-628, 1987, doi: 10.1109/TEC.1987.4765901.

[63] S. Ansuj, F. Shokooh, and R. Schinzinger, "Parameter estimation for induction machines based on sensitivity analysis," *IEEE Transactions on Industry Applications,* vol. 25, no. 6, pp. 1035-1040, 1989, doi: 10.1109/28.44239.

[64] D. Lindenmeyer, H. W. Dommel, A. Moshref, and P. Kundur, "An induction motor parameter estimation method," *International Journal of Electrical Power & Energy Systems,* vol. 23, no. 4, pp. 251-262, 2001/05/01/ 2001, doi: https://doi.org/10.1016/S0142-0615(00)00060-0.

[65] S. Deleanu, D. Carpenter, W. Yaremko, G. V. Lipinski, and N. Galan, "Comparison of Induction Machine Parameter Determination Methods and the Impact on Steady State Performances," in *5th International Conference on Modern Power Systems MPS 2013*, Cluj-Napoca, Romania, May 2013, vol. 1, pp. 156-163.

[66] G. J. Rogers and D. Benaragama, "An induction motor model with deep-bar effect and leakage inductance saturation," *Archiv für Elektrotechnik,* vol. 60, pp. 193-201, 1978, doi: 10.1007/BF01595160.

[67] B. Mirafzal, G. L. Skibinski, R. M. Tallam, D. W. Schlegel, and R. A. Lukaszewski, "Universal Induction Motor Model With Low-to-High Frequency-Response Characteristics," *IEEE Transactions on Industry Applications,* vol. 43, no. 5, pp. 1233-1246, 2007, doi: 10.1109/TIA.2007.904401.

[68] S. I. Moon and A. Keyhani, "Estimation of induction machine parameters from standstill time domain data," in *Conference Record of the 1993 IEEE Industry Applications Conference Twenty-Eighth IAS Annual Meeting*, 2-8 Oct. 1993 1993, pp. 336-342 vol.1, doi: 10.1109/IAS.1993.298945.

[69] H. A. Toliyat, E. Levi, and M. Raina, "A review of RFO induction motor parameter estimation techniques," *IEEE Transactions on Energy Conversion,* vol. 18, no. 2, pp. 271-283, 2003, doi: 10.1109/TEC.2003.811719.

[70] W. Kaiyu, J. Chiasson, M. Bodson, and L. M. Tolbert, "A nonlinear least-squares approach for identification of the induction motor parameters," *IEEE Transactions on Automatic Control,* vol. 50, no. 10, pp. 1622-1628, 2005, doi: 10.1109/TAC.2005.856661.

[71] C. Laughman, S. B. Leeb, L. K. Norford, S. R. Shaw, and P. R. Armstrong, "A two-step method for estimating the parameters of induction machine models," in *2009 IEEE Energy Conversion Congress and Exposition*, 20-24 Sept. 2009 2009, pp. 262-269, doi: 10.1109/ECCE.2009.5316204.

[72] J. Pedra, "Estimation of typical squirrel-cage induction motor parameters for dynamic performance simulation," *IEE Proceedings - Generation, Transmission and Distribution,* vol. 153, no. 2, pp. 137-146, 2006, doi: 10.1049/ip-gtd:20045209.

[73] M. H. Haque, "Determination of NEMA Design Induction Motor Parameters From Manufacturer Data," *IEEE Transactions on Energy Conversion,* vol. 23, no. 4, pp. 997-1004, 2008, doi: 10.1109/TEC.2008.2001451.

[74] S. R. Shaw and S. B. Leeb, "Identification of induction motor parameters from transient stator current measurements," *IEEE Transactions on Industrial Electronics,* vol. 46, no. 1, pp. 139-149, 1999, doi: 10.1109/41.744405.

[75] W. Rong-Ching, Yuan-Wei, and C. Tseng Cheng-Yi, "Estimating Parameters of the Induction Machine by the Polynomial Regression," *Applied Sciences, MDPI AG,* vol. 8, no. 7, 2018.

[76] P. D. Agarwal and P. L. Alger, "Saturation Factors for Leakage Reactance or Induction Motors," *Transactions of the American Institute of Electrical Engineers. Part III: Power Apparatus and Systems,* vol. 79, no. 3, pp. 1037-1042, 1960, doi: 10.1109/AIEEPAS.1960.4500907.

[77] *NEMA MG 1-2016 Motors and Generators*, N. E. M. A. (NEMA), 2016. [Online]. Available: https://www.nema.org/Standards/ComplimentaryDocuments/NEMA%20MG%201-2016%20CONTENTS%20and%20FOREWORD.pdf

[78] J. J. Cathey, R. K. Cavin, and A. K. Ayoub, "Transient Load Model of an Induction Motor," *IEEE Transactions on Power Apparatus and Systems,* vol. PAS-92, no. 4, pp. 1399-1406, 1973, doi: 10.1109/TPAS.1973.293548.

[79] P. C. Krause and C. H. Thomas, "Simulation of Symmetrical Induction Machinery," *IEEE Transactions on Power Apparatus and Systems,* vol. 84, no. 11, pp. 1038-1053, 1965, doi: 10.1109/TPAS.1965.4766135.

APPENDIX A: RE-SCALING OF PRE-PROCESSED DATA

Data returned in the first two columns of a prep output file is proportional to real and reactive power. To properly scale the data to reflect actual real and reactive power flow, one must understand the data flow.

- Current flowing through the CT is scaled down to a measurable level by a factor k. Thus, the secondary current flowing out of the CT is

$$i_{sec} = \frac{1}{k} i_{line}$$

- The secondary current flowing out of the CT is converted to a voltage by the measurement resistor

$$v_m = R_m i_{sec}$$

- The measured voltage is converted to a discrete value by an N-bit analog-to-digital converter. Typically, we use a 12-bit device that converts measured voltages into one of 2^{12} different values between 0 and 4095. The conversion factor here is what is known as a single bin or least-significant bit (LSB). One LSB is

$$LSB = \frac{2^N}{g}$$

where g is a value that corresponds to the maximum peak-to-peak voltage range of the A/D converter. The PCI-1710 cards that we currently use have a user-selectable measuring range. The possible measuring ranges and the corresponding g values are presented in Table A.1.

Table A.1: Measuring Range and *g* value for each PCI-1710 gain code.

Software Gain Code	Measuring Range (V)	g
0	-5 to +5	10
1	-2.5 to 2.5	5
2	-1.25 to 1.25	2.5
3	-.625 to .625	1.25
4	-10 to 10	20

- Prep passes the discrete voltage values to a discrete Fourier transform (DFT) algorithm that computes the amplitude of the in-phase and quadrature components of the fundamental of the current. If the samples obtained by the NILM are contained in the vector $i[n]$, then the corresponding 128-point DFT is

$$I[k] = \sum_{n=0}^{127} i[n] e^{-j\frac{2\pi kn}{128}}$$

At line frequency, the current contains a single sine wave, i.e.

$$i_{fund}[n] = I_o \cos(\Omega n + \phi) = Re\{e^{j\phi} e^{j\Omega n}\}$$

Before performing its Fourier analysis, prep performs a re-sampling process that ensures that fundamental of the current contains 128 points. Thus, the discrete frequency Ω of fundamental is $2\pi/128$. The first two columns of the final prep output contain the real and imaginary components of the second term of the DFT decomposition, i.e. the real and imaginary part of $I[1]$. Computation of $I[1]$ under the above-stated conditions shows that it is

$$I[1] = 64 I_o e^{j\phi} = 64 I_o (\cos\phi + j \sin\phi)$$

The first column of the prep output contains the real part of this result, and the second column contains the imaginary part. The DFT analysis is performed using a common fast Fourier transform (FFT) algorithm.

- To convert prep output to an *RMS* current one must undo all of the scaling performed in each of the above steps. The resulting equation is the following:

$$I_{real\ or\ imag} = \frac{x}{64}\frac{g}{2^{12}}\frac{1}{R_m}k\frac{1}{\sqrt{2}}$$

  The same equation is applied to both the second column and the first column.

- In a single phase system, the resulting real and imaginary components can be converted to real and reactive power via the relations

$$P = 120I_{real}$$

$$Q = 120I_{imag}$$

CAVEAT: Note that these calculations assume that the fundamental component of the voltage is 120V (RMS). In general, this is not true. The utility maintains the RMS value of the voltage around 120V. This means that the RMS value of the total waveform, including harmonics (which can be present in relatively large quantities) is 120V. Thus, the actual RMS value of the fundamental is lower than 120V. By definition, power cannot be transferred by a voltage and current at different frequencies. The approximation made here appears reasonable in low-voltage applications where power quality is not a major concern. In medium-voltage applications, this is not the case.

APPENDIX B: INDUCTION MACHINE SIMULATION CODE

Induction Machine Parameters

indpara.m

```
% This code loads the parameters for 500 hp, 2300V, 4-pole induction machine.
global P rs rr Xm X1s X1r we J Bl vds vqs vqr vdr Tl power
% These are the machine parameters for a 500 Hp, 1878V (L-N, peak) AC
% induction machine.
P = 4;        % Number of poles (*not* pole pairs)
rs = 0.262;   % Stator resistance
rr = 0.187;   % Rotor resistance
Xm = 56.02;   % Magnetizing Impedance, in Ohms on a 60 Hz base
X1s = 1.206;  % Stator Side Leakage Impedance, in Ohms on a 60 Hz base
X1r = 1.206;  % Rotor Side Leakage Impedance, in Ohms on a 60 Hz base
we = 377.;    % Base electrical frequency, rads per second (60 Hz)
J = 11.06;     % Rotor Inertia
Bl = 0.057;       % Load Damping Coefficient
vds = 0.0;    % D axis stator voltage
vqs = 1878.0;  % Q axis stator voltage
vqr = 0.0;    % D axis rotor voltage
vdr = 0.0;    % Q axis rotor voltage
```

State Variable Calculations for D-Q Model

ind.m

```
function [slopes] = ind(t,statev)
global P rs rr Xm X1s X1r we J Bl vds vqs vqr vdr Tl power
w = 377.;
```

```
Lm  = Xm/we;  % This is the magnetizing inductance

L1s = X1s/we; % Stator leakage

L1r = X1r/we; % Rotor leakage

Las = L1s + Lm;

Lar = L1r + Lm;

lamqs = statev(1);

lamds = statev(2);

lamqr = statev(3);

lamdr = statev(4);

wr    = statev(5)

th    = statev(6);

thr   = statev(7);

D = Lm*Lm - Las*Lar;

idr   = (Lm*lamds - Las*lamdr)/D;

iqr   = (Lm*lamqs - Las*lamqr)/D;

iqs   = (Lm*lamqr - Lar*lamqs)/D;

ids   = (Lm*lamdr - Lar*lamds)/D;

s1 = (vqs - w*lamds - rs*iqs);

s2 = (vds + w*lamqs - rs*ids);

s3 = (vqr - (w - wr)*lamdr - rr*iqr);

s4 = (vdr + (w - wr)*lamqr - rr*idr);

T  = (3/2)*(P/2)*(lamqr*idr - lamdr*iqr);

Tl = 0.0583*(2*wr/P)^2 ;

s5 = (P/2)*(T - Tl)/J;

s6 = 377;

s7 = wr ; %/(P/2);
```

```
slopes = [s1 s2 s3 s4 s5 s6 s7]';
```

The solution of Differential Equations

runind.m

```
time = [0:1/8000:15];

state0 = [0 0 0 0 0 0 0]';

[tout,yout] = ode45('ind',time, state0);

figure(5)

plot(tout,yout(:,5));

xlabel('Time, Seconds');

ylabel('Electrical Rotor Speed, Rads per Second')

title('Motor Spin-up');
```

Conversion from D-Q to Stator and Rotor Quantity

convind.m

```
function [m,m2,m3] = convind(t,y);

global P rs rr Xm X1s X1r we J Bl vds vqs vqr vdr Tl power

w = 377.;

Lm  = Xm/we;  % This is the magnetizing inductance

 L1s = X1s/we; % Stator leakage

 L1r = X1r/we; % Rotor leakage

 Las = L1s + Lm;

 Lar = L1r + Lm;

 lamqs = y(:,1);

 lamds = y(:,2);

 lamqr = y(:,3);

 lamdr = y(:,4);
```

```
wr    = y(:,5);

th    = y(:,6);

thr   = y(:,7);

D = Lm*Lm - Las*Lar;

idr   = (Lm*lamds - Las*lamdr)/D;

iqr   = (Lm*lamqs - Las*lamqr)/D;

iqs   = (Lm*lamqr - Lar*lamqs)/D;

ids   = (Lm*lamdr - Lar*lamds)/D;

 T     = (3/2)*(P/2)*(lamqr.*idr - lamdr.*iqr);

ias = cos(th).*ids - sin(th).*iqs;

ibs = cos(th - 2.*pi/3.).*ids - sin(th - 2.*pi/3.).*iqs;

ics = cos(th + 2.*pi/3.).*ids - sin(th + 2.*pi/3.).*iqs;

vas = cos(th).*vds - sin(th).*vqs;

vbs = cos(th - 2.*pi/3.).*vds - sin(th - 2.*pi/3.).*vqs;

vcs = cos(th + 2.*pi/3.).*vds - sin(th + 2.*pi/3.).*vqs;

iar = cos(th-thr).*idr - sin(th-thr).*iqr;

ibr = cos(th -thr - 2.*pi/3.).*idr - sin(th -thr - 2.*pi/3.).*iqr;

icr = cos(th -thr + 2.*pi/3.).*idr - sin(th -thr + 2.*pi/3.).*iqr;

i_rms = (sqrt(ids.^2 + iqs.^2))/sqrt(2);

m = [ids iqs idr iqr];

m2 = [T ias ibs ics vas vbs vcs];

 m3 = [iar ibr icr i_rms];
```

Plots

motor_sim.m

```
indparam;
runind
 [m,m2,m3] = convind(tout,yout);
 figure(1);
plot(tout,m2(:,2),tout,m2(:,5));
xlabel('time in seconds');
ylabel('Ibs, Vas');
 i_sim = m3(:,4);
v_sim = m2(:,5);
 figure(3);
plot(tout,m3(:,1))
xlabel('time in seconds');
ylabel('Iar')
maxi_ibr = max(m3(:,1));
 N =2*3600*yout(:,5)/(P*377) ;
 figure(4)
 plot(N,m2(:,1));
%plot(N,m2(:,1))
xlabel('Speed, RPM');
ylabel('tourque, N.m')
title('Torque-Speed');
maxi_Torque = max(m2(:,1));
 t = ((1:length(i_sim))/8000);
```

```
figure(8)
plot(t,i_sim,'r'); hold on;
```

Conversion of Simulated Data

sim2asc.m

```
function sim2asc(v_sim,i_sim,Rm_v,Rm_i,Rin_v,scale_i,filename)
motor_sim
Rm_v = 100;
Rm_i = 47;
Rin_v = 50000;
scale_i = 1/1000;
filename = 'motor_rms_current_sim_J= 11.06';
out = [v_sim, i_sim];
[a,b] = size(out);
 clear out;
 if (b ~= 2)
    error('Check dimensions - v_sim and i_sim should be column vectors');
end
 % Now, compute the voltages seen by the PCI-1710
 if (scale_i > 1)
    error ('Scale factor should be less than 1.  i.e. 1/1000');
end
v_in = v_sim*(1/Rin_v)*2.5*Rm_v;
i_in = i_sim*scale_i*Rm_i;
v_out = v_in*(4096/10)+2048;
v_out = round(v_out);
```

```
i_out = i_in*(4096/10)+2048;

i_out = round(i_out);

out = [v_out i_out];

% Now, write the output file.

 str = sprintf('save -ASCII %s out',filename);

eval(str);
```

APPENDIX C: MATLAB CODES FOR FIELD DATA

Calculation of In-rush Period

inrush.m

```
clear all;
clc;
files = dir('aggregate*0400*');
name2=[];
delta2=[];
for i=1:length(files)
x_crusher5=load(files(i).name);
name=files(i).name
filename='Crusher5_StartupCurrent_Change';
fid1 = fopen(filename,'a');
t=[0:1:length(x_crusher5)-1]*(1/7200);
global ...
   FILTER_LENGTH ...
   FILTER_CUTOFF ...
   GETEVENTS_SKIP ...
   GETEVENTS_THRESHOLD ...
    I1=-x_crusher5(:,1);
   I1=I1*(10/4096)*(1/64)*(1000/15)*(1/6)*(100/5)*(1/sqrt(2));
   I2=-x_crusher5(:,2);
   I2=I2*(10/4096)*(1/64)*(1000/15)*(1/6)*(100/5)*(1/sqrt(2));
   I = sqrt((I1).^2 + (I2).^2);
 % Now, get the event locations with the change-of-mean detector
```

```
nilmconst;
b = fir1(FILTER_LENGTH,FILTER_CUTOFF);
thresh = GETEVENTS_THRESHOLD/10;
[ev,z] = event(I,b,thresh);
ev=ev';
skip=GETEVENTS_SKIP;
if (length(ev)<2)
    fprintf(fid1,'%s \n zero \n',name);
end
if (length(ev)>1)
    if(length(I)-ev(end) <= skip)
        ev = ev(1:end-1);
        if(ev(1)<=20)
            ev = ev(2:end);
        end
    end
   y=I(ev(:));
    z=(ev(2)-ev(1))/120;
    ev=ev/7200
    ev_s=ev*60
    fid = fopen('I_rescaled_crusher5.txt', 'w');
    fprintf(fid, '%s\n', I);
    fclose(fid);
    y=length(files);
    name2=strvcat(name2,name);
    delta2=[delta2;y ev(1) ev(2) ev_s(1) ev_s(2) z];
```

```
    end
end
out=[name2 num2str(delta2)];
fid = fopen('Crusher5_Start_Current.txt', 'w');
   for I = 1:length(out(:,1))
      fprintf(fid, '%s\n', out(I,:));
   end
start_current.name=name2;
start_current.delta=delta2;
save Start_Current5_Structure -struct start_current
   fclose(fid)
   open('Crusher5_Start_Current.txt')
```

FFT Code for Field-Tested Data

fft.m

```
clear all;
clc;
files=load('fft_files_0604_062008_structure.mat');
files_5=files.c5;
files_6=files.c6;
files_a=files.agg;
out1=[];
out2=[];
for i=1:length(files_5(:,1))
  D_crusher5 = files_5(i,:)   % NEED TO CHANGE DATE AND TIME ACCORDINGLY
  D_crusher6 = files_6(i,:)   % NEED TO CHANGE DATE AND TIME ACCORDINGLY
```

```
 D_aggregate = files_a(i,:)   % NEED TO CHANGE DATE AND TIME ACCORDINGLY
 x_crusher5 = load(D_crusher5);
 x_crusher6 = load(D_crusher6);
 x_aggregate = load(D_aggregate);
 file_title_crusher5 = D_crusher5(1:findstr(D_crusher5,'.') - 1);
 file_title_crusher6 = D_crusher6(1:findstr(D_crusher6,'.') - 1);
 file_title_aggregate = D_aggregate(1:findstr(D_aggregate,'.') - 1);
 out1=strvcat(out1,file_title_crusher5);
  I1_crusher5 = -x_crusher5(:,1);
  I1_crusher6 = -x_crusher6(:,1);
  I1_aggregate = x_aggregate(:,1);
   I2_crusher5 = -x_crusher5(:,2);
   I2_crusher6 = -x_crusher6(:,2);
   I2_aggregate = x_aggregate(:,2);
% rescale reactive current
rescaled_current_I1_crusher5 =
(I1_crusher5)*(10/4096)*(1/64)*(1000/15)*(1/6)*(100/5)*(1/sqrt(2));
rescaled_current_I1_crusher6 =
(I1_crusher6)*(10/4096)*(1/64)*(1000/15)*(1/6)*(100/5)*(1/sqrt(2));
rescaled_current_I1_aggregate  =
(I1_aggregate)*(10/4096)*(1/64)*(1000/15)*(1/55.5455)*(2000/5)*(1/sqrt(2));
 % rescale active current
 rescaled_current_I2_crusher5 =
(I2_crusher5)*(10/4096)*(1/64)*(1000/15)*(1/6)*(100/5)*(1/sqrt(2));
rescaled_current_I2_crusher6 =
(I2_crusher6)*(10/4096)*(1/64)*(1000/15)*(1/6)*(100/5)*(1/sqrt(2));
```

```
rescaled_current_I2_aggregate =
(I2_aggregate)*(10/4096)*(1/64)*(1000/15)*(1/55.5455)*(2000/5)*(1/sqrt(2)); %*(4.2*sqrt(3));
% Current Amplitude
 I_rms_crusher5 = sqrt((rescaled_current_I1_crusher5).^2 + (rescaled_current_I2_crusher5).^2);
 I_rms_crusher6 = sqrt((rescaled_current_I1_crusher6).^2 + (rescaled_current_I2_crusher6).^2);
 I_rms_aggregate = sqrt((rescaled_current_I1_aggregate).^2 +
(rescaled_current_I2_aggregate).^2);
 %%%%%      CHANGE NEEDED FOR VARIABLES 'SM' AND 'EM'    %%%%%%
 % HERE 'SM= STARTING MINUTE' AND 'EM=ENDING MINUTE' BETWEEN WHICH
YOU NEED FFT.  %%%%
SM = 20;    % STARTING MINUTE AT WHICH YOU WANT TO TAKE FFT
EM = 25;    % ENDING MINUTE AT WHICH YOU WANT TO TAKE FFT
fft_section_crusher5 = I_rms_crusher5(7200*SM:7200*EM);
fft_section_crusher6 = I_rms_crusher6(7200*SM:7200*EM);
fft_section_aggregate = I_rms_aggregate(7200*SM:7200*EM);
meaan_I_crusher5 = mean(fft_section_crusher5)
meaan_I_crusher6 = mean(fft_section_crusher6)
meaan_I_aggregate = mean(fft_section_aggregate)
x_detrend_crusher5 = detrend(fft_section_crusher5);
x_detrend_crusher6 = detrend(fft_section_crusher6);
x_detrend_aggregate = detrend(fft_section_aggregate);
N = 2^16;                   % Number of points in fft
f_sample = 120;               % NILM sampling frequency is 8000 Hz
Y_crusher5 = fft(x_detrend_crusher5.*kaiser(length(x_detrend_crusher5)),N);
Y_crusher6 = fft(x_detrend_crusher6.*kaiser(length(x_detrend_crusher6)),N);
Y_aggregate = fft(x_detrend_aggregate.*kaiser(length(x_detrend_aggregate)),N);
```

```
f=[0:1:N/2-1]*(f_sample/N);
max5_12=[];
max5_24=[];
max6_12=[];
max6_24=[];
max5_36=[];
max6_36=[];
ind5_12=0;
ind5_24=0;
ind6_12=0;
ind6_24=0;
ind5_36=0;
ind6_36=0;
ind=0;
for i=1:length(f)
if (f(i)>=11)
   if (f(i)<=12)
      ind=f(i)*N/f_sample;
   m5_12=abs(Y_crusher5(ind));
   m6_12=abs(Y_crusher6(ind));
   max5_12=[max5_12;m5_12];
   max6_12=[max6_12;m6_12];
   end
end
if (f(i)>=23)
   if(f(i)<=24)
```

```
        ind=f(i)*N/f_sample;
    m5_24=abs(Y_crusher5(ind));
    m6_24=abs(Y_crusher6(ind));
    max5_24=[max5_24;m5_24];
    max6_24=[max6_24;m6_24];
    end
end
if (f(i)>=35)
    if(f(i)<=36)
        ind=f(i)*N/f_sample;
    m5_36=abs(Y_crusher5(ind));
    m6_36=abs(Y_crusher6(ind));
    max5_36=[max5_36;m5_36];
    max6_36=[max6_36;m6_36];
    end
end
end
max5_12=max(max5_12)
max6_12=max(max6_12)
max5_24=max(max5_24)
max6_24=max(max6_24)
max5_36=max(max5_36)
max6_36=max(max6_36)
 for j=1:length(f)
     if (f(j)>=11)
        if (f(j)<=12)
```

```
        ind=f(j)*N/f_sample;
        m5_12=abs(Y_crusher5(ind));
        m6_12=abs(Y_crusher6(ind));
        if m5_12==max5_12
           ind5_12=ind
        end
        if m6_12==max6_12
           ind6_12=ind
        end
     end
  end
  if (f(j)>=23)
     if (f(j)<=24)
        ind=f(j)*N/f_sample;
        m5_24=abs(Y_crusher5(ind))
        m6_24=abs(Y_crusher6(ind))
        if m5_24==max5_24
           ind5_24=ind
        end
        if m6_24==max6_24
           ind6_24=ind
        end
     end
  end
  if (f(j)>=35)
     if (f(j)<=36)
```

```
        ind=f(j)*N/f_sample;
        m5_36=abs(Y_crusher5(ind))
        m6_36=abs(Y_crusher6(ind))
        if m5_36==max5_36
           ind5_36=ind
        end
        if m6_36==max6_36
           ind6_36=ind
        end
      end
   end
end
   ind5_12=ind5_12*f_sample/N
   ind6_12=ind6_12*f_sample/N
   ind5_24=ind5_24*f_sample/N
   ind6_24=ind6_24*f_sample/N
   ind5_36=ind5_36*f_sample/N
   ind6_36=ind6_36*f_sample/N
   diff_12=ind5_12-ind6_12
   diff_24=ind5_24-ind6_24
   diff_36=ind5_36-ind6_36
   y=length(files_5(:,1));
out2=[out2; y meaan_I_crusher5 meaan_I_crusher6 meaan_I_aggregate ind5_12 max5_12
ind6_12 max6_12 diff_12 ind5_24 max5_24 ind6_24 max6_24 diff_24 ind5_36 max5_36 ind6_36
max6_36 diff_36];
    s = [out1  num2str(out2)];
```

```
    fid = fopen('Crusher_FFT_0604_062008_Data.txt', 'w');  % PLEASE PLACE A FILE NAME
    for I = 1:length(s(:,1))
        fprintf(fid, '%s\n', s(I,:));
    end
        fclose(fid);
 figure(1);
 plot(f,abs(Y_crusher5(1:length(Y_crusher5)/2)));
title(file_title_crusher5); xlabel('Frequency: Hz'); ylabel('Magnitude');
saveas(gcf,['FFT_',file_title_crusher5],'fig');
 figure(2);
 plot(f,abs(Y_crusher6(1:length(Y_crusher6)/2)));
title(file_title_crusher6); xlabel('Frequency: Hz'); ylabel('Magnitude');
saveas(gcf,['FFT_',file_title_crusher6],'fig');
figure(3);
plot(f,abs(Y_aggregate(1:length(Y_aggregate)/2)));
title(file_title_aggregate); xlabel('Frequency: Hz'); ylabel('Magnitude');
saveas(gcf,['FFT_',file_title_aggregate],'fig');
end
```

APPENDIX D: MATLAB CODE FOR PARAMETER ESTIMATION

Code for Simulation Test:

```
clear all;
motor_sim;


t5=2:220/5;
ip1=mean(i_p(t5));
iq1=mean(i_q(t5));
irms1=ip1+j*iq1;
Z_lr=vqs/(sqrt(2)*irms1);
r1 = real(Z_lr);
x1 = imag(Z_lr)

wb=377;

X1 = (x1/2);
X2 = (x1/2) ;
Rs=0.262;
Rr=r1-Rs;

power = 500.0*746.0;
f0 = 60.0;
s0 = 0.015;
Te = (P/2)*power/(2*pi*f0*(1-s0));
t6=300:700;  % at steady state
ip2=mean(i_p(t6));
iq2=mean(i_q(t6));
i_ss = ip2+j*iq2;    %%%steady state current
irms2=abs(i_ss);

a=Te;
b=(3*irms2^2)*(P/2)*(1/(2*pi*f0))*(Rr/s0);
c=2*Te*X2;
d=(Te*(Rr^2/s0^2))+(Te*X2^2);

syms t positive    %%% real or positive or imag
xm = double(solve((a-b)*t^2 + t*c +d));  %%%%% Initial guess of Xm
beta=Te/(2*pi*f0*(1-s0))^2;
t_s=1.833333;
wra = (2*pi*f0*(1-s0))/t_s;
Tl_a = beta*wra^2
 t3=2:55;

ia=sqrt(i_p(120)^2+i_q(120)^2);
sa=(377-wra)/377;

Te_a=(3*(P/2)*(xm^2/377)*(Rr/sa)*(ia^2))/(((Rr/sa)^2)+(xm+X2)^2);
```

```
J=(P/2)*((Te_a-Tl_a)/wra)
```

Code for Laboratory Test:

```
clear all;
x = load('C1current_output.dat');
 % CT factors
n = 2000;
R = 100;
sf = (20/2^16)
 I_scale = (n/R)*sf*(1/24);
 I_p = x(:,2)*I_scale*(1/sqrt(2));
I_q = x(:,1)*I_scale*(1/sqrt(2));
 figure(18);
plot(I_p), hold on;
ylabel('I_p');
figure(16);
plot(I_q), hold on;
ylabel('I_q');
irms = sqrt(I_p.^2+I_q.^2);
figure(15)
plot(irms), hold on;
V_scale = (1/24)*(20/2^16)*(200e3)*(1/50)*(1/2.5);
y = load('C1voltage_output.dat');
V = y(:,1)*V_scale*(1/(sqrt(2)*sqrt(3)));
figure(50);
plot(V);
I_p_ss = mean(I_p(1000:end));
I_q_ss = mean(I_q(1000:end));
I_ss = I_p_ss+j*I_q_ss;
t1=245:250;
I_p_lr = mean(I_p(t1));
I_q_lr = mean(I_q(t1));
I_lr = sqrt(I_p_lr^2+I_q_lr^2)*exp(j*atan(I_q_lr/I_p_lr));
Z_lr = 277/I_lr;
Xr = (3/5)*imag(Z_lr);
Xs = (2/3)*Xr;
R_t=real(Z_lr)
Rr=R_t/4.396;
Rs=R_t-Rr
Z_run = 277/(I_p_ss+j*I_q_ss);
xm = imag(Z_run)-Xs;
% P=2;
% power = 0.5*746.0;
% f0 = 60.0;
% s0 = 0.0417;  %%%%%
% Te = (P/2)*power/(2*pi*f0*(1-s0));  %%%%%%steady state torque at full load
% ia =1.1; %%% full load amperes
% Te_a=(3*(P/2)*(xm^2/377)*(Rr/s0)*(ia^2))/(((Rr/s0)^2)+(xm+Xr)^2)
% Te-Te_a
```

```
f_run = 59.7;
s_run = (60-59.7)/60;
Z_run = 277/(I_p_ss+j*I_q_ss);
X_m = [300:0.1:350];
R_r = [1:.01:10];
X_r = Xr;
R_s = Rs;
X_s=Xs;
A = zeros(length(X_m)*length(R_r)*length(X_r),5);
m=1;
for n=1:1:length(X_m)
  for k=1:1:length(R_r)
   for  l=1:1:length(X_r)
        R_r_run = R_r(k)/s_run;
        Z = j*X_s + R_s + j*X_m(n)*(R_r_run+j*X_r(l))/(j*(X_m(n)+X_r(l))+R_r_run);
        I_est = 277/Z;
        err = sqrt((real(I_est)-I_p_ss)^2 + (imag(I_est)-I_q_ss)^2);
         A(m,1) = X_m(n);
        A(m,2) = R_r(k);
        A(m,4) = err;
        m = m+1;

   end
   end
end
[y,index]=min(A(:,4));
R_r = A(index,2);
X_m = A(index,1);
X_r = Xr;
err = A(index,4);
Z_est = j*X_s + R_s + j*X_m*(R_r/s_run+j*X_r)/(j*(X_m+X_r)+R_r/s_run);
I_est = 277/Z_est;
I_r_run = I_est*(j*X_m)/(j*(X_m+X_r)+R_r/s_run)
T_est = 3*abs(I_r_run)^2*(R_r/s_run)/(2*pi*60*(1-s_run))
beta = T_est/(2*pi*f_run)^2
%%%%%%%%Inertia
t_s=0.5/3;
s1 = (60-59.7)/60;
f0=60;
P=2;
wra = (2*pi*f0*(1-s1))*t_s*2;
Tl_a = beta*wra^2
 %%%%for torque at transient
ia=sqrt(I_p(261)^2+I_q(261)^2);
sa=(377-wra)/377;
Te_a=(3*(P/2)*(X_m^2/377)*(Rr/sa)*(ia^2))/(((Rr/sa)^2)+(X_m+Xr)^2);
J=(1/6)*(P/2)*((Te_a-Tl_a)/wra);
```